Progress in Polymer Science 36 (2011) 1697–1753

Contents lists available at ScienceDirect

Progress in Polymer Science

journal homepage: www.elsevier.com/locate/ppolysci

A review of nonlinear oscillatory shear tests: Analysis and application of large amplitude oscillatory shear (LAOS)

Kyu Hyun[a,*], Manfred Wilhelm[b], Christopher O. Klein[b], Kwang Soo Cho[c], Jung Gun Nam[d], Kyung Hyun Ahn[d], Seung Jong Lee[d], Randy H. Ewoldt[e], Gareth H. McKinley[f]

[a] School of Chemical and Biomolecular Engineering, Pusan National University, Jangjeon-Dong 30, Busan 609-735, Republic of Korea
[b] Institute for Chemical Technology and Polymer Chemistry, Karlsruhe Institute of Technology (KIT), Engesserstraße 18, 76128 Karlsruhe, Germany
[c] Department of Polymer Science and Engineering, Kyungpook National University, Sangyeok-Dong 1370, Daegu 702-701, Republic of Korea
[d] School of Chemical and Biological Engineering, Seoul National University, Seoul 151-744, Republic of Korea
[e] Institute for Mathematics and its Applications & Department of Chemical Engineering and Materials Science, University of Minnesota, Minneapolis, MN 55455, USA
[f] Department of Mechanical Engineering, Massachusetts Institute of Technology (MIT), Cambridge, MA 02139, USA

ARTICLE INFO

Article history:
Received 10 May 2010
Received in revised form 11 February 2011
Accepted 16 February 2011
Available online 11 March 2011

Keywords:
LAOS (Large amplitude oscillatory shear)
Nonlinear response
FT-Rheology
Stress decomposition (SD)

ABSTRACT

Dynamic oscillatory shear tests are common in rheology and have been used to investigate a wide range of soft matter and complex fluids including polymer melts and solutions, block copolymers, biological macromolecules, polyelectrolytes, surfactants, suspensions, emulsions and beyond. More specifically, small amplitude oscillatory shear (SAOS) tests have become the canonical method for probing the linear viscoelastic properties of these complex fluids because of the firm theoretical background [1–4] and the ease of implementing suitable test protocols. However, in most processing operations the deformations can be large and rapid: it is therefore the nonlinear material properties that control the system response. A full sample characterization thus requires well-defined nonlinear test protocols. Consequently there has been a recent renewal of interest in exploiting large amplitude oscillatory shear (LAOS) tests to investigate and quantify the nonlinear viscoelastic behavior of complex fluids. In terms of the experimental input, both LAOS and SAOS require the user to select appropriate ranges of strain amplitude (γ_0) and frequency (ω). However, there is a distinct difference in the analysis of experimental output, i.e. the material response. At sufficiently large strain amplitude, the material response will become nonlinear in LAOS tests and the familiar material functions used to quantify the linear behavior in SAOS tests are no longer sufficient. For example, the definitions of the linear viscoelastic moduli $G'(\omega)$ and $G''(\omega)$ are based inherently on the assumption that the stress response is purely sinusoidal (linear). However, a nonlinear stress response is not a perfect sinusoid and therefore the viscoelastic moduli are not uniquely defined; other methods are needed for quantifying the nonlinear material response under LAOS deformation. In the present review article, we first summarize the typical nonlinear responses observed with complex fluids under LAOS deformations. We then introduce and critically compare several methods that quantify the nonlinear oscillatory stress response. We illustrate the utility and sensitivity of these protocols by investigating the nonlinear response of various complex fluids over a wide range of frequency and amplitude of deformation, and show that LAOS characterization is a rigorous test for rheological models and advanced quality control.

* Corresponding author.
E-mail address: kyuhyun@pusan.ac.kr (K. Hyun).

0079-6700/$ – see front matter © 2011 Elsevier Ltd. All rights reserved.
doi:10.1016/j.progpolymsci.2011.02.002

Contents

1. Introduction 1698
   1.1. Dynamic oscillatory shear test 1698
   1.2. Historical survey of LAOS 1700
   1.3. Scope of the present article 1702
2. Experimental methods and setup 1702
3. Fundamental LAOS behavior 1703
   3.1. Basic mathematical descriptions of LAOS 1703
   3.2. $G'(\gamma_0)$ and $G''(\gamma_0)$ 1705
      3.2.1. Type I (strain thinning) 1707
      3.2.2. Type II (strain hardening) 1707
      3.2.3. Type III (weak strain overshoot) 1707
      3.2.4. Type IV (strong strain overshoot) 1708
   3.3. Nonlinear shear stress waveforms 1709
   3.4. Nonlinear normal stress difference 1711
4. Quantitative methods for analyzing nonlinear stress waveforms 1717
   4.1. Fourier transform (FT) 1717
      4.1.1. New nonlinear quantitative coefficient, Q from FT-Rheology 1720
      4.1.2. Transition between linear and nonlinear viscoelasticity 1722
      4.1.3. Even harmonics of the normal stress differences 1723
      4.1.4. Even harmonics within the shear stress 1723
   4.2. Characteristic functions 1724
   4.3. Stress decomposition 1726
   4.4. Chebyshev polynomial representation 1727
   4.5. Viscoelastic moduli in the nonlinear regime 1730
   4.6. Summary of quantitative methods 1731
5. Applications 1733
   5.1. Entangled polymer systems 1733
      5.1.1. Frequency-dependence of $Q_0(\omega)$ in the asymptotic regime 1733
      5.1.2. Strain-dependence of $Q(\gamma_0)$ under LAOS 1733
   5.2. Dispersion systems 1735
      5.2.1. Suspensions 1735
      5.2.2. Emulsions 1737
      5.2.3. Polymer blends 1737
      5.2.4. Filled rubber compounds 1738
   5.3. Block copolymers and gels 1739
      5.3.1. Block copolymer melts 1739
      5.3.2. Block copolymer solutions 1740
      5.3.3. Biopolymer gel 1741
6. Microstructural probes under LAOS flow 1743
   6.1. Rheo-dielectric setup 1744
   6.2. *In situ* Rheo-SAXS setup 1746
7. Concluding remarks 1746
   Acknowledgments 1747
   Appendix A. Stress direction and deformation direction 1747
   Appendix B. Odd harmonics of shear stress in oscillatory shear 1748
   Appendix C. Giesekus and UCM model 1749
   Appendix D. Q_0 at low frequency 1749
   References 1750

1. Introduction

1.1. Dynamic oscillatory shear test

Dynamic oscillatory shear tests are performed by subjecting a material to a sinusoidal deformation and measuring the resulting mechanical response as a function of time. Oscillatory shear tests can be divided into two regimes. One regime evokes a linear viscoelastic response (small amplitude oscillatory shear, SAOS) and the other regime is defined by a measurable nonlinear material response (large amplitude oscillatory shear, LAOS). As the applied amplitude (of strain or stress) is increased from small to large at a fixed frequency, a transition between the linear and nonlinear regimes can appear. Fig. 1 schematically illustrates an oscillatory strain-sweep test in which the frequency is fixed and the applied strain amplitude is varied. In Fig. 1 the viscoelastic response is quantified by two material measures, namely the elastic storage modulus $G'(\omega)$ and the viscous loss modulus $G''(\omega)$. In the linear regime the strain amplitude is sufficiently small that both viscoelastic moduli are independent of strain amplitude and the oscillatory stress response is sinusoidal. The strain amplitudes used in linear oscillatory shear tests are

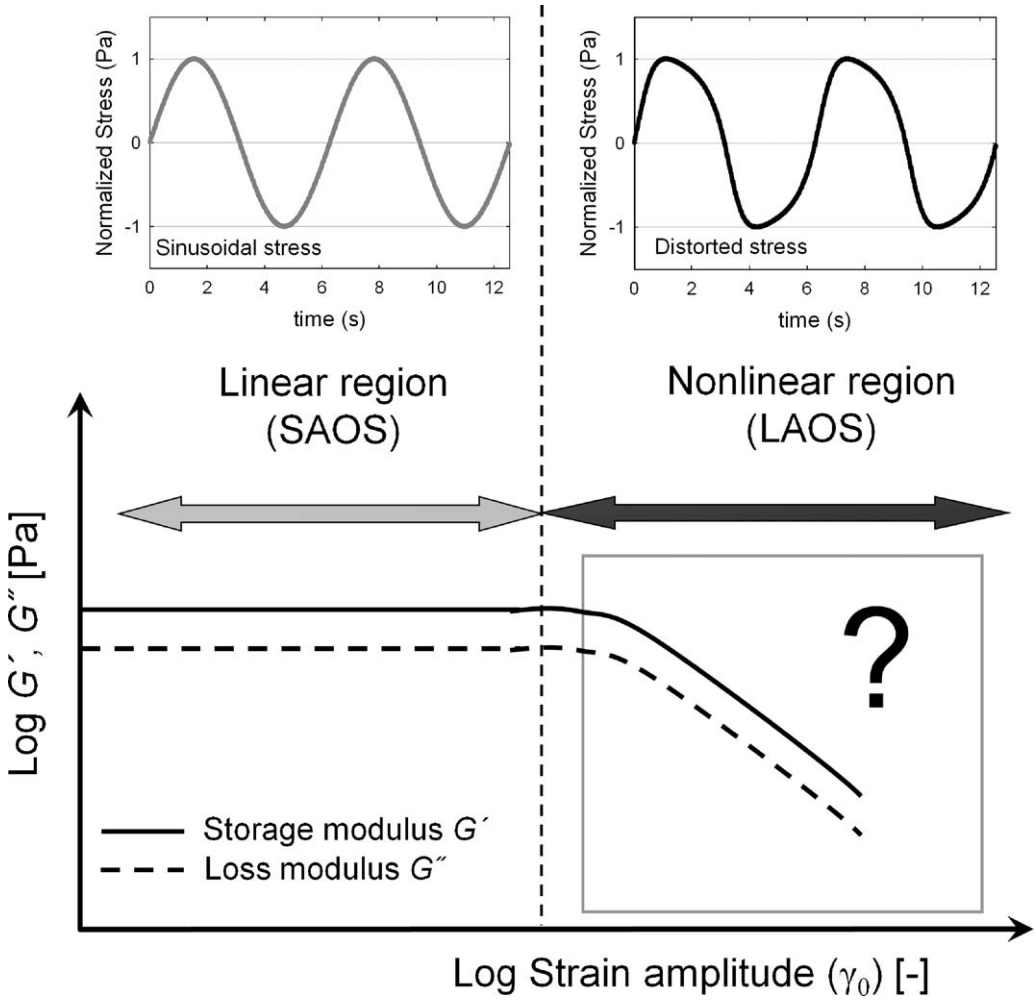

Fig. 1. Schematic illustration of the strain sweep test at a fixed frequency. This sweep test can be used for determining the linear and nonlinear viscoelastic region. In the linear region, the storage (G') and loss (G'') moduli are independent of the applied strain amplitude at a fixed frequency and the resulting stress is a sinusoidal wave. However, in the nonlinear region, the storage and loss moduli become a function of the strain amplitude ($G'(\gamma_0)$ and $G''(\gamma_0)$) at a fixed frequency and the resulting stress waveforms are distorted from sinusoidal waves. In the linear region, the oscillatory shear test is called SAOS (small amplitude oscillatory shear), and the application of LAOS (large amplitude oscillatory shear) results in a nonlinear material response.

generally very small, often on the order of $\gamma_0 \approx 10^{-2}$ to 10^{-1} for homopolymer melts and polymer solutions. For some dispersed systems (emulsions and suspensions) [5] or blockcopolymer solutions [6] the linear regime is limited to even smaller strain amplitude, $\gamma_0 < 10^{-2}$. With increasing strain amplitude the nonlinear regime can appear beyond SAOS. In the nonlinear regime, the storage or loss moduli are a function of the strain amplitude ($G'(\gamma_0)$ and $G''(\gamma_0)$) and the resulting periodic stress waveform becomes distorted and deviates from a sinusoidal wave (see Fig. 1). This nonlinear regime becomes apparent at larger strain amplitude, therefore the nonlinear dynamic test is typically referred to as large amplitude oscillatory shear (LAOS).

A SAOS test assumes that the material response is in the linear regime within the accuracy of the rheometer and therefore the material functions, e.g. G' and G'' fully describe the material response. Since linear viscoelasticity is based on a rigorous theoretical foundation [1–4], SAOS tests provide very useful and convenient rheological characterization of complex fluids or soft materials.

Although linear viscoelasticity is useful for understanding the relationship between the microstructure and the rheological properties of complex fluids, it is important to bear in mind that the linear viscoelasticity theory is only valid when the total deformation is quite small [4]. However, in most processing operations the deformation is both large and rapid (therefore in the nonlinear region) and consequently linear viscoelastic characterization is not sufficient to fully understand practical polymer processing undergoing nonlinear situations. Moreover, since linear viscoelastic experiments use small strain amplitude (SAOS test), this measurement has a limited resolution to distinguish complex fluids with similar micro- and nanostructure or molecular structures (e.g. linear or branched polymer topology). Complex fluids with similar linear viscoelastic properties may show different nonlinear viscoelastic properties. This means that even if rheological

measurements are only being used for material characterization or quality control, the linear viscoelastic properties may often be insufficient. It can be anticipated that nonlinear viscoelastic characterization will provide much more insight for distinguishing such structural differences. Additionally, the coherence between molecular theories, continuum-level constitutive equations and experiments will be improved if nonlinear parameters are matched. Thus, for several reasons, it is necessary to study the nonlinear viscoelastic responses of complex fluids in depth. Among other nonlinear rheometric tests, the steady shear viscosity is often measured as a function of shear rate. The steady-state viscosity can frequently provide the key information regarding how fast the material can be processed or shaped into a product, and this information is very helpful in polymer processing operations such as injection molding. However, when processing at high rates of deformation for short time the material does not reach steady state. Steady simple shear rate experiments also have inherent limitations: little information is provided about microstructure, information about elastic relaxation time scales is lost since the measurement is made at steady state, and several materials cannot be measured including crosslinked materials like rubber or structurally-sensitive hydrogen-bonded materials. In contrast, LAOS tests are useful for a broad class of complex fluids and soft matter because strain amplitude and frequency can be varied independently allowing a broad spectrum of conditions to be attained [7]. Furthermore, LAOS does not involve any sudden imposed jumps in speed or position, and consequently it is a relatively easy flow to generate and control [8].

1.2. Historical survey of LAOS

The basic concept of large amplitude oscillatory shear (LAOS) was introduced a number of years ago. From the 1960s to 1970s, early publications [9–19] investigated nonlinear phenomena for various viscoelastic materials under oscillatory shear and proposed the methods of Fourier transform analysis and stress waveform analysis. Technical problems severely hindered further progress at that time, specifically hardware and software limitations such as torque transducer resolution and computational power. Payne [9] observed strain-amplitude dependence of the dynamic moduli for a natural rubber filled with carbon black particles; the nonlinear behavior he reported is often referred to generically as "dynamic stress softening." This effect is called the "Payne effect" or the "Fletcher-Gent" effect [10]. Harris [11] reported the nonlinear stress behavior of suspensions of undeformable particles (a clay-water system) at low and high frequency. Philippoff [12] investigated the influence of the shear strain amplitude on the nonlinear behavior of polymer solutions up to strain amplitude $\gamma_0 \approx 7$. He was able to detect the growth of third harmonic contributions, and studied the onset of nonlinearity in several polymer solutions. MacDonald et al. [13] studied the dependence of the complex viscosity of four viscoelastic fluids (three polymer solutions and one polymer melt) for large amplitude oscillatory motion using a Weissenberg Rheogoniometer. Onogi et al. [14] investigated the viscoelastic behavior of carbon-black filled solutions of polystyrene in diethyl phthalate using a coaxial cylinder viscometer. They observed nonlinear oscillatory response signals which included odd harmonics up to the order of 5. Dodge and Krieger [15] investigated polystyrene latex and also observed the first five harmonics of shear stress at various frequencies. They concluded that oscillatory shear measurements show promise for the investigation of nonlinear fluids. Matsumoto et al. [16] calculated the fundamental stress components at the excitation frequency, G_1' and G_1'', and the corresponding third harmonic components, G_3' and G_3'', for particle suspensions in polystyrene solution (see Eq. (9), Section 3.1 for variable definitions). They found that the ratios of G_3'/G_1' and G_3''/G_1'', respectively, were of the order of 10% at an applied shear strain amplitude $\gamma_0 = 0.26$. Komatsu et al. [17] investigated the nonlinear viscoelastic behavior of two kinds of semisolid emulsions; one was an oil-in-water type and the other was water-in-oil type (commercial cosmetic creams). They compared the stress shape as a function of time including the analysis of higher Fourier components as proposed by Onogi et al. [14]. Philippoff [13], Onogi et al. [14], Dodge and Krieger [15], Matsumoto et al. [16], and Komatsu et al. [17] used Fourier transform analysis of stress data. Tee and Dealy [18] investigated the nonlinear viscoelastic properties of three polymer melts (HDPE, LDPE, and PS). In order to characterize molten thermoplastics in a simplified way, they used closed loop plots (Lissajous curves) of the measured stress vs. strain or stress vs. strain-rate. They concluded that the stress vs. strain-rate loops were more distinctive than the stress–strain loops for these materials. They suggested at the time that only the first Fourier component can be determined with precision because of experimental difficulties. Furthermore, they emphasized that the higher Fourier components have no direct relationship with traditional material functions that are commonly measured. Walters and Jones [19] concluded in 1970 that, at that time, harmonic analysis was not a useful tool in viscoelasticity studies. Precise and accurate experimental equipment was yet to be developed, such as high fidelity monochromatic sinusoidal excitation, drastically improved torque transducers, "high performance" ADC cards, and cheap and powerful computers to perform advanced signal processing techniques such as data oversampling. Before such developments, the stress and strain data were typically detected by a differential transformer and recorded by a two-pen recorder [16]. Tee and Dealy [18] obtained the stress vs. strain and stress vs. strain-rate loops by means of a storage oscilloscope, equipped with a Polaroid camera. Experiments were limited by the dynamic range of the torque transducer in the rheometers commonly used at this time, nonetheless, various analysis methods were already suggested at this early stage, especially stress shape analysis and Fourier transform analysis. Pearson and Rocherfort [20] and Helfand and Pearson [21] calculated nonlinear parameters under LAOS utilizing the Doi-Edwards model for polymer dynamics. They investigated the limits of linear viscoelastic behavior of concentrated polystyrene solutions.

During the 1990s, book chapters by Dealy and Wissbrun [4] and Giacomin and Dealy [8] described LAOS test

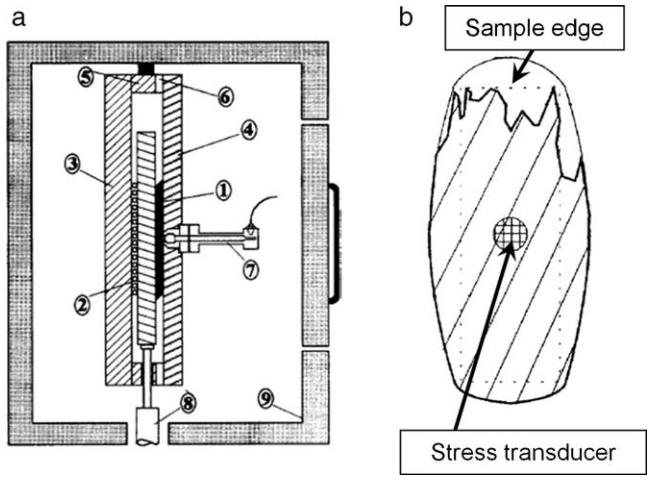

Fig. 2. (a) Cross-section showing the essential elements of a sliding plate rheometer incorporating an elastic type shear stress transducer: (1) sample (2) moving plate (7) shear stress transducer. (b) The schematic sample shape under LAOS is shown with flow heterogeneity at the sample edge, because the stress transducer is located at the center of the sample, errors induced by edge effects are avoided. Reproduced by permission of Dealy and Jeyaseelan [28], copyright (1998) of the Society of Rheology.

protocols and provided rich sources of information on the LAOS experiments and analysis at the time. Dealy and Giacomin [4,7,8,22–27] investigated the LAOS behavior of various polymer melts with a unique sliding plate rheometer (SPR, see Fig. 2). Their results under LAOS flow were investigated via waveform analysis (closed-loop plots), Fourier transform analysis of the stress response, and constitutive equation modeling. In most sliding-plate rheometers, the shear stress is inferred from a total force measurement and thus may include error due to flow heterogeneities at the sample edges. To avoid this problem, they invented a shear-stress transducer that could be flush-mounted in the stationary plate [28] (see Fig. 2). Hence, the shear stress could be measured locally in a region of uniform deformation, away from the free surface boundaries, and they were able to conduct LAOS tests of highly viscous polymer melts to strain amplitudes $\gamma_0 > 10$. With such large imposed deformations, very large nonlinearities could be generated that could be easily detected with the state-of-the-art software and hardware at that time. This unique custom setup was used for investigating high density polyethylene (HDPE) [22], polyurethane [23], low density polyethylene (LDPE) and HDPE [24], and linear low density polyethylene (LLDPE) [25]. They also studied wall slip of HDPE [23] and determined model parameters for various nonlinear constitutive equations under LAOS, including the Liu, Mewis-Denn, Mewis-De Cleyn, and PTT model [26,27], the Wagner integral equation [24], and the revised Berkeley kinetic network model [7]. These pioneering studies directly connecting LAOS experiments and simulations were primarily focused on polymer melts because the sliding plate rheometer (SPR) is optimized for measuring such highly viscous systems. The SPR also has some disadvantages, as it cannot measure low viscosity systems, e.g. polymer solutions or dispersed systems, it has a limited signal-to-noise range, and it was never widely commercially available. Sliding-plate devices continue to be custom-built and used to study complex fluid rheology [29].

Wilhelm et al. [30–33] developed the methodology for high sensitivity Fourier transform (FT) rheology by transferring techniques from NMR spectroscopy to oscillatory rheometery on commercial rheometers. Their work is distinguished by the development and use of extremely sensitive detection methods, especially the use of "oversampling" with high performance Analog-to-Digital Converter (ADC) cards, electrical and mechanical shielding, and a special FT algorithm [30,34]. These contributions lead to an improvement of about 2–3 decades in the signal/noise ratio compared to former work, with a final signal to noise ratio $S/N \approx 10^5$. Some of these contributions are discussed in detail in Section 4.1, "FT-Rheology." With these developments, it was possible to obtain high resolution torque signals from commercial rheometers and to obtain Fourier transform spectra for complex fluids with very low viscosities. The simple and easy setup using a commercial rheometer was clearly beneficial for broader adoption of the technique.

FT-Rheology was used for various complex fluids, such as polymer melts [35–43], polymer solutions [44,45], polymer blends [46–48], block copolymers [6,49,50] and dispersed systems [5,33,46,51]. Leblanc et al. [52–61] systematically investigated various industrial elastomers and rubber materials with FT-Rheology, including EPDM rubber(ethylene propylene diene M-class rubber) [52–54], poly(vinyl chloride) (PVC)/green coconut fiber (GCF) composites [55], carbon black filled rubber compounds [53,56–59], natural rubber [60], polybutadiene rubber (BR) and styrene-butadiene rubber (SBR) [54,57], and thermoplastic vulcanizates (TPVs). TPVs are blends of a crystalline thermoplastic polymer (e.g. polypropylene) and a vulcanizable rubber composition. For these multiphase and heterogeneous polymer materials Leblanc [61] shows that LAOS experiments can be used to elucidate the structure of industrially important polymer blends. Such rubbery samples usually display a very high torque value and can exhibit elastic instability under LAOS flow due to the polymer network structures. In order to over-

come these drawbacks, they used the Rubber Process Analyzer RPA 2000 with a closed cavity geometry, in combination with "high performance" ADC cards [62]. The normalized intensity of the third harmonic obtained from FT-Rheology was used to investigate systematically the effect of filler and long chain branching in these elastomer materials.

As already noted, the storage modulus (G') and the loss modulus (G'') at large strain lose their precise physical meaning when stress is no longer perfectly sinusoidal. However, useful calculations can still be made. Section 4.5 addresses the various options for calculating nonlinear viscoelastic moduli and the interpretation associated with each choice. At present the commonly output moduli from commercial rheometers are the first-harmonic moduli G'_1 and G''_1, see Eq. (9), Section 3.1. Ahn et al. [63–65] classified complex fluids according to the strain-amplitude dependence of the first-harmonic viscoelastic moduli $G'(\gamma_0)$ and $G''(\gamma_0)$ for experiments and simulations. (In this article the generic notation G' and G'' will refer to the first-harmonic Fourier moduli G'_1 and G''_1 unless otherwise stated.) Ahn et al. observed that the LAOS behavior of complex fluids could be classified into four primary categories, but acknowledged that other types which look like a variation or combination of these four types may also exist as indicated by a literature survey [63]. It was also reported that network theory simulations suggest the existence of four generic types of LAOS responses [64,65]. The investigation of $G'(\gamma_0)$ and $G''(\gamma_0)$ at a fixed frequency under LAOS is the simplest method to classify complex fluids without obtaining raw stress data, and is directly available on any commercial rheometer.

For LAOS tests, however, the stress output is not purely sinusoidal and the behavior can no longer be fully described in terms of a storage modulus (G') and loss modulus (G''), due to the presence of higher harmonic contributions (see Section 3 for more detail). The viscoelastic nonlinearity can be quantified in a simple way by using the Fourier transform method [33]. Recently, other methods to quantify nonlinearity under LAOS have also been proposed. Cho et al. [66] suggested a nonlinear "stress decomposition" (SD) method. The SD method decomposes the generic nonlinear stress response into a superposition of "elastic" and "viscous" contributions. The SD method provides a very useful step toward a physical interpretation of nonlinear stress response. Klein et al. [5,67] use sets of simplified characteristic functions, specifically sine, rectangular, triangular, and saw tooth waves to describe the prototypical nonlinear responses. These selected waveforms may be thought of as a set of "basis functions" used to represent a superposition of different physical phenomena; however they are neither orthogonal (in a mathematical way) nor unique selections. Ewoldt et al. [68,69] quantified the nonlinear viscoelastic material functions on the basis of the SD method by using a set of orthogonal Chebyshev polynomials of the first kind. They also suggested meaningful viscoelastic moduli in the nonlinear regime, e.g. minimum-strain and large-strain elastic modulus and minimum-rate and large-rate dynamic viscosity. With these concepts, they could efficiently and uniquely define strain stiffening/softening and shear thickening/thinning. One of the goals of this article is to review and compare these different quantitative methods.

1.3. Scope of the present article

Oscillatory shear tests investigate and quantify viscoelastic properties of complex fluids or soft matter. If the strain amplitude is kept small the results can be discussed within the framework of linear viscoelasticity, therefore SAOS (small amplitude oscillatory shear) tests have been extensively studied both theoretically and experimentally. However, if the strain amplitude is increased, interesting nonlinear effects occur. There have already been extensive articles on specific nonlinear oscillatory shear tests [4,8,33]. Since the latest published review article [33], there has been much progress on quantitative methods for analyzing and interpreting LAOS tests, and applications of these methods. However, until now there has been no systematic review of the recent developments in the field of nonlinear oscillatory shear tests. In this article we review and compare several quantitative methods which have been proposed for analyzing nonlinear stress responses to deformation-controlled oscillatory shear. These methods are given context through the LAOS characterization of several classes of materials.

Section 2 introduces the experimental methods used to obtain raw stress data under LAOS loading. Section 3 introduces several generic nonlinear behaviors observed in various complex fluids under LAOS including the leading order quantitative description using $G'(\gamma_0)$ and $G''(\gamma_0)$, and the oscillatory waveforms shapes of nonlinear shear stress and the nonlinear normal stress difference. Section 4 summarizes and compares several quantitative methods proposed by researchers for analyzing non-sinusoidal stress waveforms. In Section 5 we introduce several experimental findings under LAOS for various complex fluids, e.g. polymer melts, solutions, block copolymers, dispersions and others. In Section 6 we review experimental configurations which combine rheometry and morphology characterization to investigate the influence of LAOS flow on the structural change of complex fluids. Finally, Section 7 offers concluding remarks and an outlook on the future use and development of LAOS techniques.

2. Experimental methods and setup

Commercially available strain-controlled rheometers are typically used for performing LAOS tests. It is most desirable to obtain raw oscillatory waveforms for proper analysis (as reviewed in Section 4), which may require modifications to the factory-purchased instrument setup. The most common experimental modification is based on a commercial strain-controlled rheometer with separated motor and transducer technology, e.g. the RMS 800, ARES, or ARES-G2 instruments from TA Instruments, in which raw signals of torque, normal force, and motor displacement are available as analog voltage outputs. In order to convert these analog signals into digital signals, shielded BNC-type cables are connected between the instrument output and an analog-to-digital converter (ADC) card. The two important points of selecting the ADC card are the

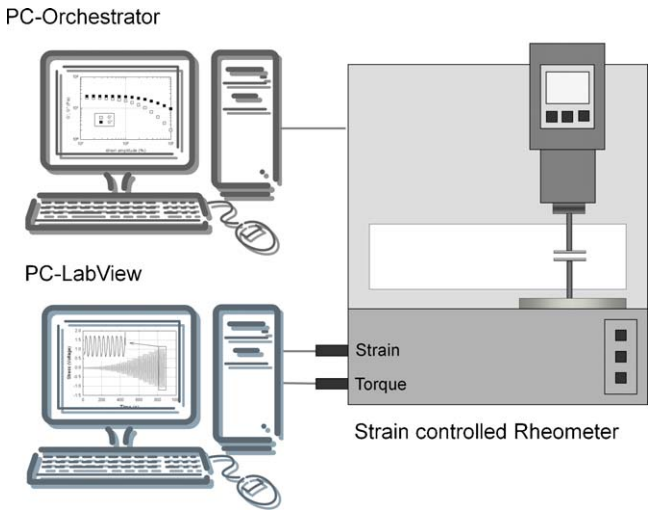

Fig. 3. Experimental setup for common LAOS experiments. The displacement (strain), torque and normal forces are digitized via a stand-alone PC. The rheometer is controlled via a second PC with the standard instrument software.

digital input resolution (dynamic range) and the maximum sampling rate. Typically a 16-bit (input resolution) analog-to-digital converter (ADC) card with sampling rates up to 100–333 kHz for one channel or 50–150 kHz for two channels is used. Measurement and on-the-fly boxcar averaging (oversampling) of the raw signals can increase the effective dynamic range of the transducer and allow for lower torques to be detected (see below). The ADC card (e.g. National Instruments, Austin, TX, USA) can be installed on a stand-alone PC equipped with home-written LabView software (National Instruments). In this way the factory-provided rheometer control software is fully independent. This modified rheometer setup, which provides high-resolution raw oscillatory waveform data, is displayed in Fig. 3.

For rheological measurements – and in general for any spectroscopic technique – there is a clear need for the most sensitive detection possible. This can be realized by developing more sensitive detection devices, shielding spurious signals, or processing and acquiring data with refined methods. Dusschoten and Wilhelm [34] proposed that torque transducer sensitivity could be increased by using appropriate data processing techniques. The basic idea is to acquire the oscillatory shear data at the highest possible acquisition rate as allowed by a high performance ADC card, i.e. – the raw data is oversampled. The sampling rate may exceed 50 kHz with this method even for 1 Hz mechanical excitation. In a second step the raw time data is truncated on the fly by means of a so-called boxcar average at a fixed time interval, e.g. several hundreds or thousands of raw data points [70] are averaged into a single time data point. The application of the boxcar average to the raw time data results in a new "down-sampled" time domain data set with a strongly reduced number of data points and drastically reduced random noise for each new data point. Here, the oversampling can be considered as an adjustable low pass filter in the frequency domain. In Fig. 4, the torque response as a function of time is shown for a data set together with the applied oversampling number. Oversampling number (*No.*) means that "*No.*" data points are averaged and collapsed into a single oversampled new data point. As expected, the random noise decreases as the oversampling number (*No.*) increases (Fig. 4), provided that the oversampling number is not so large as to lose information from the raw signal (not shown).

3. Fundamental LAOS behavior

In this section we discuss the most basic methods used for interpreting LAOS tests. We begin with a review of mathematical descriptions of the LAOS stress responses. The common outputs from commercial rheometers are torque (or forces) and displacements. Intrinsic rheological parameters are then calculated using geometric parameters and appropriate analysis, e.g. stresses, strains, compliances, and viscoelastic moduli. For strain-controlled LAOS tests, the stress response is analyzed in terms of strain-dependent viscoelastic moduli, which we discuss in some detail in Sections 3.1 and 3.2. This is followed by visual analysis of nonlinear oscillatory stress waveforms (specifically the shear stress in Section 3.3 and the first normal stress difference in Section 3.4). Advanced analysis techniques are left to be reviewed in detail in Section 4.

3.1. Basic mathematical descriptions of LAOS

Applying an oscillatory shear flow, the strain and strain-rate inputs can be described as follows

$$\gamma(t) = \gamma_0 \sin \omega t, \quad \dot{\gamma}(t) = \omega\gamma_0 \cos \omega t \tag{1}$$

The stress response to this input deformation can be analytically represented in various ways. In the dynamic steady state, the shear stress of viscoelastic materials can be considered as an instantaneous function of the input strain and strain-rate. Thus we can expand the shear stress in the

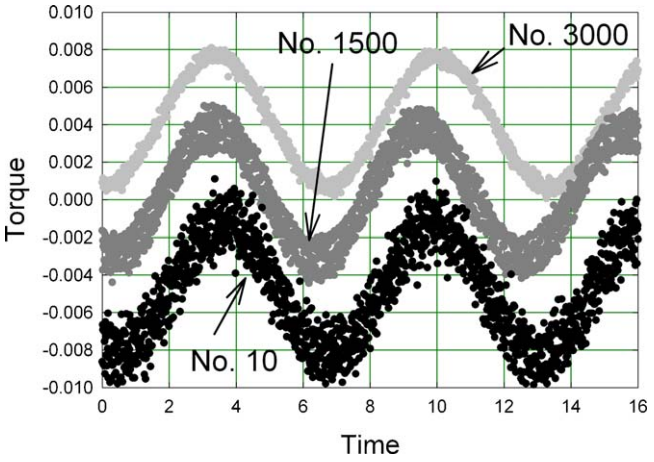

Fig. 4. The torque as a function of time for Xanthan gum 4% aqueous solution at fixed strain amplitude, $\gamma_0 = 0.03$ with strain controlled rheometer RMS 800 that can detect a torque within the range 2–2000 mN m. The torque is shifted vertically for ease of comparison. Increasing the oversampling number reduces the noise while the absolute torque amplitude remains the same.

nonlinear regime by a polynomial or Taylor expansion with respect to the strain and strain-rate:

$$\sigma(t) = \sum_{i=0}\sum_{j=0} C_{ij}\gamma^i(t)\dot{\gamma}^j(t) \tag{2}$$

where C_{ij} are mathematical constants for the expansion of nonlinear stress as a function of strain and strain rate. The values of C_{ij} are related to material functions in the linear and nonlinear regime. A similar expansion is used to describe nonlinear optics [71]. The stress response of viscoelastic materials is typically independent of the shear direction, and it is assumed that the sign of the shear stress changes as the sign of shearing changes, and therefore the shear stress must be an odd function with respect to the direction of shearing deformations. Therefore, we can obtain criteria for the symmetry of the shear stress as follows (see Appendix A):

$$\sigma[-\gamma(t), -\dot{\gamma}(t)] = -\sigma[\gamma(t), \dot{\gamma}(t)] \tag{3}$$

Considering the symmetry criteria of Eq. (3), we can rewrite Eq. (2) as follows:

$$\sigma(t) = \sum_{i=1}\sum_{j=1}[C_{2i-1,2(j-1)}\gamma^{2i-1}(t)\dot{\gamma}^{2(j-1)}(t) + C_{2(i-1),2j-1}\gamma^{2(i-1)}(t)\dot{\gamma}^{2j-1}(t)] \tag{4}$$

Inserting Eq. (1) into Eq. (4) results in the following expression for the shear stress,

$$\sigma(t) = \sum_{i=1}\sum_{j=1}\gamma_0^{2i+2j-3}\omega^{2j-1}\left[\frac{C_{2i-1,2(j-1)}}{\omega}\sum_{m=1,odd}^{2i+2j-3} a_m \sin m\omega t + C_{2(i-1),2j-1}\sum_{n=1,odd}^{2i+2j-3} b_n \cos n\omega t\right] \tag{5}$$

Therefore, we may write the shear stress as a function of the *odd* higher-order terms in the nonlinear regime as follows (see Appendix B for more detail):

$$\sigma(t) = \sum_{p,odd}\sum_{q,odd}^{p}\gamma_0^q[a_{pq}\sin q\omega t + b_{pq}\cos q\omega t] \tag{6}$$

Expanding this expression explicity gives

$$\begin{aligned}
&\sigma(t) = \gamma_0[a_{11}\sin\omega t + b_{11}\cos\omega t] + \gamma_0^3[a_{31}\sin\omega t \\
&+b_{31}\cos\omega t + a_{33}\sin 3\omega t + b_{33}\cos 3\omega t] + O(\gamma_0^5) + \cdots \\
&a_{11} = C_{10}|_{\gamma_0\to 0} = G'(\omega), \qquad b_{11} = C_{01}|_{\gamma_0\to 0} = G''(\omega), \\
&a_{31} = \frac{1}{2}(C_{10} + C_{12}\omega^2), \qquad b_{31} = \frac{1}{4}(-C_{21}\omega + 3C_{03}\omega^3), \\
&a_{33} = \frac{1}{4}(-C_{30} + C_{12}\omega^2), \qquad b_{33} = \frac{1}{4}(-C_{21}\omega + C_{03}\omega^3), \\
&a_{51} = \frac{1}{2}C_{32}\omega^2, \qquad b_{51} = \frac{1}{4}(3C_{23}\omega^3 - 2C_{41}\omega), \\
&a_{53} = \frac{1}{4}(C_{14}\omega^4 - C_{50}), \qquad b_{53} = \frac{1}{16}(-3C_{41}\omega - C_{23}\omega^3 + 5C_{05}\omega^5), \\
&\vdots \qquad\qquad \vdots
\end{aligned} \tag{7}$$

where $a_{11} = G'(\omega)$ and $b_{11} = G''(\omega)$ in the linear regime. With the given assumptions, it is seen that the shear stress waveform contains only *odd* higher harmonic contributions for LAOS deformations. Eq. (6) is the same result as obtained by Pearson and Rochefort [20]. The higher order terms in Eq. (6) result from the assumption that shear stress must be an odd function of shear deformations (Eq. (3)). By contrast, the normal stress differences do not change sign if the shearing direction changes, but remain independent of shear direction. This means that the normal stress differences must be exclusively *even* functions of shear deformations (i.e. $N_{1,2}[-\gamma(t), -\dot{\gamma}(t)] = N_{1,2}[\gamma(t), \dot{\gamma}(t)]$, where $N_{1,2}$ denotes either the first or second normal stress difference). Thus, the normal stress differences measured under LAOS deformations have only even higher terms [1,43,72] of the excitation frequency.

The mathematical assumptions above can be violated for several reasons, first, as a result of inhomogeneous flow in the measuring geometries, e.g. wall slip [73,74], elastic instability [75,76], secondary flows in the parallel

plates [77], or shear banding [78], and second, by imperfect (anharmonic) mechanical excitation, back-lash in the torsional actuator imposing the deformation and so on. It might further be possible to generate even terms of shear stress via microstructural anisotropy. Such non-idealized situations may therefore cause the presence of even harmonic terms in the shear stress or odd harmonic terms in the normal stress differences, however these features are generally of lower intensity. Even harmonic contributions of shear stress will be reviewed in more detail in Section 4.1.4.

Following from Eq. (6), a different notation is also possible for the nonlinear stress, written in terms of amplitude and phase [8,33]. The total nonlinear viscoelastic stress can be expanded as a linear viscoelastic stress characterized by a stress amplitude and phase shift plus the odd higher harmonic contributions (higher stress amplitude and phase shift). Consequently, the stress can be represented as:

$$\sigma(t) = \sum_{n=1,odd} \sigma_n \sin(n\omega t + \delta_n) \tag{8}$$

where the harmonic magnitude $\sigma_n(\omega, \gamma_0)$ and the phase angle $\delta_n(\omega, \gamma_0)$ depend on both the strain amplitude γ_0 and the excitation frequency ω. This Eq. (8) clarifies the starting point of "Fourier transform" rheology (FT-Rheology: see also Section 4.1). Note that Eq. (6) and Eq. (8) describe the same nonlinear phenomena using different mathematical descriptions. Giacomin and Dealy [8] referred to Eq. (6) as a power series and Eq. (8) as a Fourier series. One can re-write each Fourier component from Eq. (8) as components which are in-phase and out-of-phase with the strain input, and factoring out strain amplitude (γ_0) define a set of nonlinear viscoelastic moduli [8]:

$$\sigma(t) = \gamma_0 \sum_{n,odd} [G'_n(\omega, \gamma_0) \sin(n\omega t) + G''_n(\omega, \gamma_0) \cos(n\omega t)] \tag{9}$$

Eq. (6) can be rewritten as

$$\sigma(t) = \sum_{n,odd} \sum_{m,odd}^{n} \gamma_0^n [G'_{nm}(\omega) \sin(m\omega t) + G''_{nm}(\omega) \cos(m\omega t)] \tag{10}$$

which nicely separates the strain dependence from the frequency dependence, therefore being distinct from Eq. (9). Giacomin and Dealy [8] reported that the terms of this power series are not simply related to those of the Fourier series. However, either mathematical description can be used to argue for a leading order nonlinear coefficient (see Section 4.1.2). The complex mathematics is one of the reasons why there are many ways to interpret the complex nonlinear response under dynamic oscillatory shear.

3.2. $G'(\gamma_0)$ and $G''(\gamma_0)$

As mentioned in the introduction, LAOS tests are typically applied as a strain amplitude sweep at fixed frequency (see Fig. 1). The storage modulus G' and the loss modulus G'' are strictly defined only in the linear viscoelastic regime, and therefore their values at large strain amplitude may have ambiguous physical meaning. However, if care is taken, the measurements of $G'(\gamma_0)$ and $G''(\gamma_0)$ at a fixed frequency can provide meaningful information. Section 4.5 addresses the various options for calculating nonlinear viscoelastic moduli and the interpretation associated with each choice. We re-emphasize here that in this review the generic notation G' and G'' will refer to the first-harmonic moduli G'_1 and G''_1 (Eq. (9)) which is the most common option for calculating viscoelastic moduli from a non-sinusoidal response and is the typical output of commercial rheometer software.

Before quantifying the non-sinusoidal waveforms of LAOS stress responses, we first discuss the interpretation of the amplitude-dependent leading order description of a nonlinear response, i.e. $G'(\gamma_0)$ and $G''(\gamma_0)$. Typical LAOS studies include the results of $G'(\gamma_0)$ and $G''(\gamma_0)$ since this information can be obtained from commercial rheometers even when raw oscillatory data is unavailable. The higher harmonic contributions describing the extent of distortion away from a linear sinusoidal stress response are normally not large if compared with the amplitude of the first harmonic (typically <20%). Therefore, the moduli obtained from the first harmonic via Fourier transform analysis are relevant for a leading order description of the viscoelastic properties. Hyun et al. [63] observed that the leading order LAOS behavior ($G'(\gamma_0)$ and $G''(\gamma_0)$) of complex fluids could be classified by at least four types of strain-amplitude dependence: type I, strain thinning (G' and G'' decreasing); type II, strain hardening (G' and G'' increasing); type III, weak strain overshoot (G' decreasing, G'' increasing followed by decreasing); type IV, strong strain overshoot (G' and G'' increasing followed by decreasing). The four types of LAOS behavior are schematically shown in Fig. 5 and Hyun et al. [63] documented each class of LAOS behavior from different complex fluids with different microstructure.

Equating the representation of Fourier series (Eq. (9)) and power series (Eq. (10)), the 1st harmonic contribution can be calculated as:

$$\begin{aligned} 1\text{st term} &= [G'_{11}\gamma_0 + G'_{31}\gamma_0^3 + O(\gamma_0^5) + \cdots] \sin \omega t \\ &+ [G''_{11}\gamma_0 + G''_{31}\gamma_0^3 + O(\gamma_0^5) + \cdots] \cos \omega t = G'_1(\omega, \gamma_0) \sin \omega t \\ &+ G''_1(\omega, \gamma_0) \cos \omega t \end{aligned} \tag{11}$$

which shows that $G'_1(\omega, \gamma_0)$ and $G''_1(\omega, \gamma_0)$ consist of odd polynomials of the strain amplitude (γ_0) with nonlinear coefficients of frequency (ω). Therefore, we can observe the LAOS behavior of the 1st term as a function of strain amplitude. The nonlinear coefficients from the power series (e.g. $G'_{11}(\omega), G'_{31}(\omega), \ldots$ and $G''_{11}(\omega), G''_{31}(\omega), \ldots$) in Eq. (11) determine the leading-order amplitude dependence of $G'_1(\gamma_0)$ and $G''_1(\gamma_0)$. The relaxation processes which represent the viscoelasticity of the materials are connected with the nonlinear coefficients that are only a function of frequency for the elastic part ($G'_{11}(\omega), G'_{31}(\omega), \ldots$) and for the viscous part ($G''_{11}(\omega), G''_{31}(\omega), \ldots$).

For example, Heymann et al. [79] investigated the nonlinear behavior of medium- and highly-concentrated suspensions of spherical and quasimonodisperse particles by analyzing $G'_1(\gamma_0)$ and $G''_1(\gamma_0)$ at a fixed frequency. They

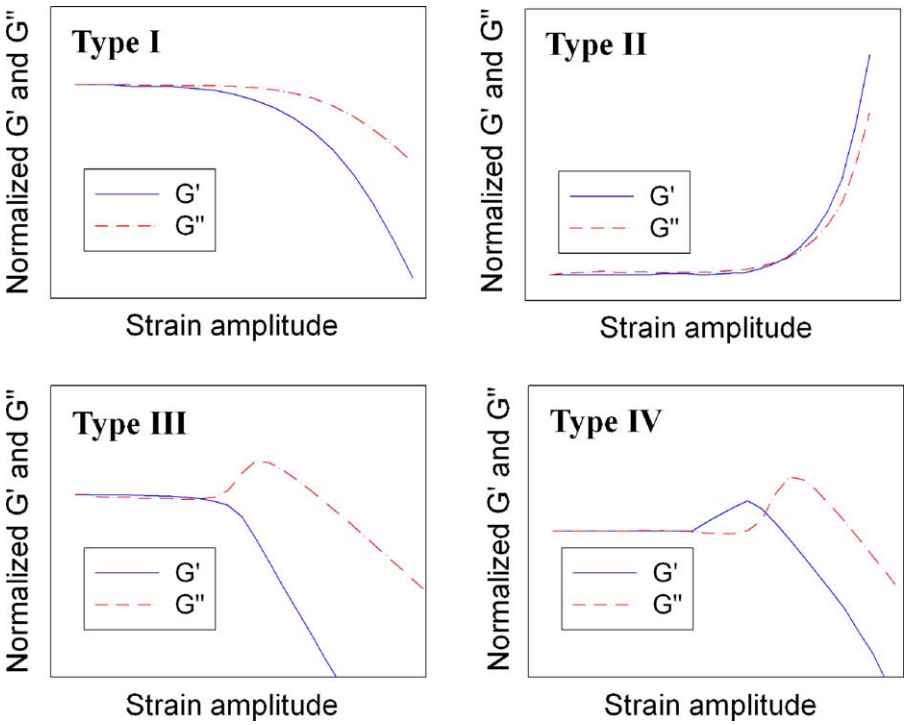

Fig. 5. The four archetypes of LAOS behavior as outlined by Hyun et al. [63]; (a) strain thinning (b) strain hardening (c) weak strain overshoot (d) strong strain overshoot. Reproduced by permission of Hyun et al. [63], copyright (2002) of Elsevier.

also investigated the effect of changing the imposed oscillatory frequency. From this result, they concluded that concentrated suspension have a Hookean response at low strain amplitude, and with increasing strain amplitude go through a nonlinear transition region to a Newtonian flow range at high strain amplitude. They also pointed out that $G_1'(\gamma_0)$ and $G_1''(\gamma_0)$ are acceptable measures of the viscoelastic response because the deviation of the response signal from a pure harmonic wave does not exceed 15%, in terms of the proportion of higher harmonics. Wyss et al. [80] introduced a technique called strain-rate frequency superposition (SRFS) for probing the nonlinear structural relaxation of metastable soft materials. For materials exhibiting a relaxation time which depends solely on the applied strain-rate amplitude, one may conduct a series of LAOS tests which maintain a constant strain-rate amplitude and therefore isolate the structural relaxation dependence. This new experimental technique (SRFS) is different from a typical strain amplitude sweep test. Wyss et al. reported values of $G_1''(\omega, \gamma_0)$ and $G_1''(\omega, \gamma_0)$ from a commercial rheometer under LAOS flow. Both Heymann et al. [79] and Wyss et al. [80] effectively employ first order nonlinear harmonic information, i.e. $G_1''(\omega, \gamma_0)$ and $G_1''(\omega, \gamma_0)$ in order to investigate the nonlinear rheology of complex fluids.

Sim et al. [65] investigated possible mechanisms of complex LAOS behavior using a network model composed of segments and junctions. A segment is considered a part of a macromolecular chain or a microstructure joining two successive junctions, and the junctions are the points where the intra- or intermolecular interactions are localized. A junction may be regarded as a crosslinking point, but basically it is a phantom element defined in the network model for convenience. Segments are lost and created during the flow, and the network consists of junctions with a distribution of ages. Although there are many families of network models, they share the common feature that the distribution of network junctions is determined by their creation $f(t)$ and loss rates $g(t)$. The main difference between models is the functional form of the creation and loss rates of network junctions. For the case of a single mode, the evolution of the state of stress in the network model can be written in terms of the creation and loss functions as follows [65,81],

$$\frac{d\sigma_{11}}{dt} = 2\beta\sigma_{12} - g(t)\sigma_{11} + f(t) - g(t) \tag{12}$$

$$\frac{d\sigma_{12}}{dt} = \beta\sigma_{22} - g(t)\sigma_{12} + \beta \tag{13}$$

$$\frac{d\sigma_{22}}{dt} = -g(t)\sigma_{22} + f(t) - g(t) \tag{14}$$

$$\frac{d\sigma_{33}}{dt} = -g(t)\sigma_{33} + f(t) - g(t) \tag{15}$$

where σ is the stress scaled by the plateau modulus G_N^0, t is the time scaled by the relaxation time λ_0, and $\beta = \lambda_0\dot{\gamma}$ is the dimensionless shear rate. Sim et al. [65] used empirical functional relationships such that $f(t)$ and $g(t)$ are represented as exponential functions of the shear stress $\sigma_{12}(t)$ as follows

$$f(t) = \exp(a|\sigma_{12}(t)|) \tag{16}$$

$$g(t) = \exp(b|\sigma_{12}(t)|) \tag{17}$$

where the constants a and b are model parameters defining the creation and loss rates, respectively. This approximation is overly simplistic and will not be adequate for a quantitative analysis of real material systems. However, it qualitatively predicts the various classes of experimentally observed LAOS behaviors of complex fluids determined from $G'(\gamma_0)$ and $G''(\gamma_0)$, and rationalizes the responses in terms of the model parameters, i.e. the creation and loss rate of network junctions.

Based upon both experimental and simulation results [63,65], a broad descriptive overview of the four typical LAOS types can be given as follows.

3.2.1. Type I (strain thinning)

This type of behavior is the most commonly observed in polymer solutions and melts. The origin of strain thinning is similar to that leading to shear thinning in steady shear flow. Shear thinning in the viscosity may be the most dominant rheological property of systems such as polymer melts, suspensions, and solutions, and originates from chain orientation or alignment of microstructures along the flow direction, thus reducing the local viscous drag on material elements. As the shear rate is further increased, the flow alignment becomes more complete, and the shear viscosity decreases further [82]. A recent example of polymer melt flow-alignment in LAOS was reported by Höfl et al. [83]. They investigated anionically synthesized 1,4-cis-polyisoprene (PI), a monodisperse polymer melt that showed shear thinning behavior. With a sensitive *in situ* rheo-dielectric setup, they observed a decrease in the dielectric strength at large strain amplitude, and interpreted this as slight orientation of the end-to-end vector (polymer chain alignment) in the shear direction.

Within the network model, type I behavior results when the creation rate parameter is negative ($a < 0$) and the loss rate parameter is positive ($b > 0$). With this parameter combination, the LAOS behavior shows strain thinning regardless of the excitation frequency. When the strain amplitude is large, the network segments align with the flow field, or the network junctions are easily lost and dangling chain segments have little chance to rejoin the network structure. The model parameters specify that the creation rate decreases while the loss rate increases with increasing strain amplitude.

3.2.2. Type II (strain hardening)

Strain hardening directly contrasts strain thinning. In this case strong interactions exist between some segments of the complex fluid and therefore flow alignment is resisted undergoing shearing deformation. It is believed that strain hardening or strain stiffening is associated with the formation of complex microstructures and nonlinear elastic network elements. PVA (polyvinyl alcohol)/Borax solutions show strain hardening and it is reported that deformation leads to formation of a chemical complex between hydroxyl groups and borate anions, which plays a role analogous to temporary crosslink among the PVA chains [84]. Many biological gels, e.g. F-actin, fibrin, collagen, also show strain hardening behavior [85]. Strain hardening is associated inherently with strain-stiffening network components, or shear-induced network formation. From the viewpoint of the basic network model, the creation rate of new network junctions should be much larger than the loss rate for a shear-induced network. As a result, LAOS type II behavior is found when the creation rate parameter is positive ($a > 0$) and greater than $2b$ ($a > 2b$), see Eq. (16) and (17). At large strain amplitude, the governing equations of the network model become numerically stiff due to the large positive exponents. Experimentally, it is also difficult to obtain rheological properties at very large strain amplitude due to the sudden increase in the torque. This effect can also lead to elastic instability at large strain amplitude ($\gamma_0 > 5$).

3.2.3. Type III (weak strain overshoot)

The distinctive feature of type III behavior is a pronounced local maximum in the loss modulus. This response is a remarkably robust feature of soft glassy materials, e.g. concentrated emulsions [86,87], suspensions [5,88,89], pastes [90], soft hydrogel spheres dispersed in water [80], and electrorheological (ER) fluids [91]. It is also observed in polymer solution systems, e.g. blockcopolymer solutions [6,49], associative polymer solutions [92–94], or Xanthan gum solutions [63,95]. For the network model (Eqs. (12)–(17)), type III is found when both the creation and loss rate parameters are positive ($a > 0$, $b > 0$) but the creation rate parameter is smaller than the loss rate parameter ($a < b$). This range of parameters results in both the creation and loss terms increasing with the strain amplitude, with the destruction rate growing faster than that of creation. The positive creation rate exponent (a) is sufficient to provide increased connectivity of the network (or other microstructure arising from interactions) leading to increased dissipation, while the loss term becomes dominant at larger strain amplitude leading to the ultimate overall decrease of both G' and G''. Thus, the overshoot (i.e. local maximum of G'') may be regarded as arising from the balance between the formation and the destruction of the network junctions. Specifically, the maximum of G'' depends more on the creation rate parameter a than the loss rate parameter b of the network model.

The structural cause of the strain overshoot behavior in G'' is not universal. Depending on the class of soft material, the explanation for the local maximum of G'' is different. Tirtaatmadja et al. [92,93] suggested that the overshoot behavior of G'' could be attributed to the increase of the effective volume of temporal network structures. From the viewpoint of associative polymer solutions, Raghavan and Khan [96] explained the strain overshoot in terms of the change of flock size during the oscillatory shear deformation. They suggested that the flock size increases when weak strain overshoot behavior appears. Parthasarathy et al. [97] reported that the overshoot in G'' occurs because of viscous dissipation due to slight rearrangement of unstable clusters under shear, and that the decrease at large strain is associated with larger scale structural rearrangements. Through structural analysis using numerical simulation for ER fluids, Sim et al. [91] explained that the increase of G'' is partly related to the destruction of microstructures developed during the imposed oscillation, and the overshoot behavior is due to the reformation process of the clusters. These differing explanations for

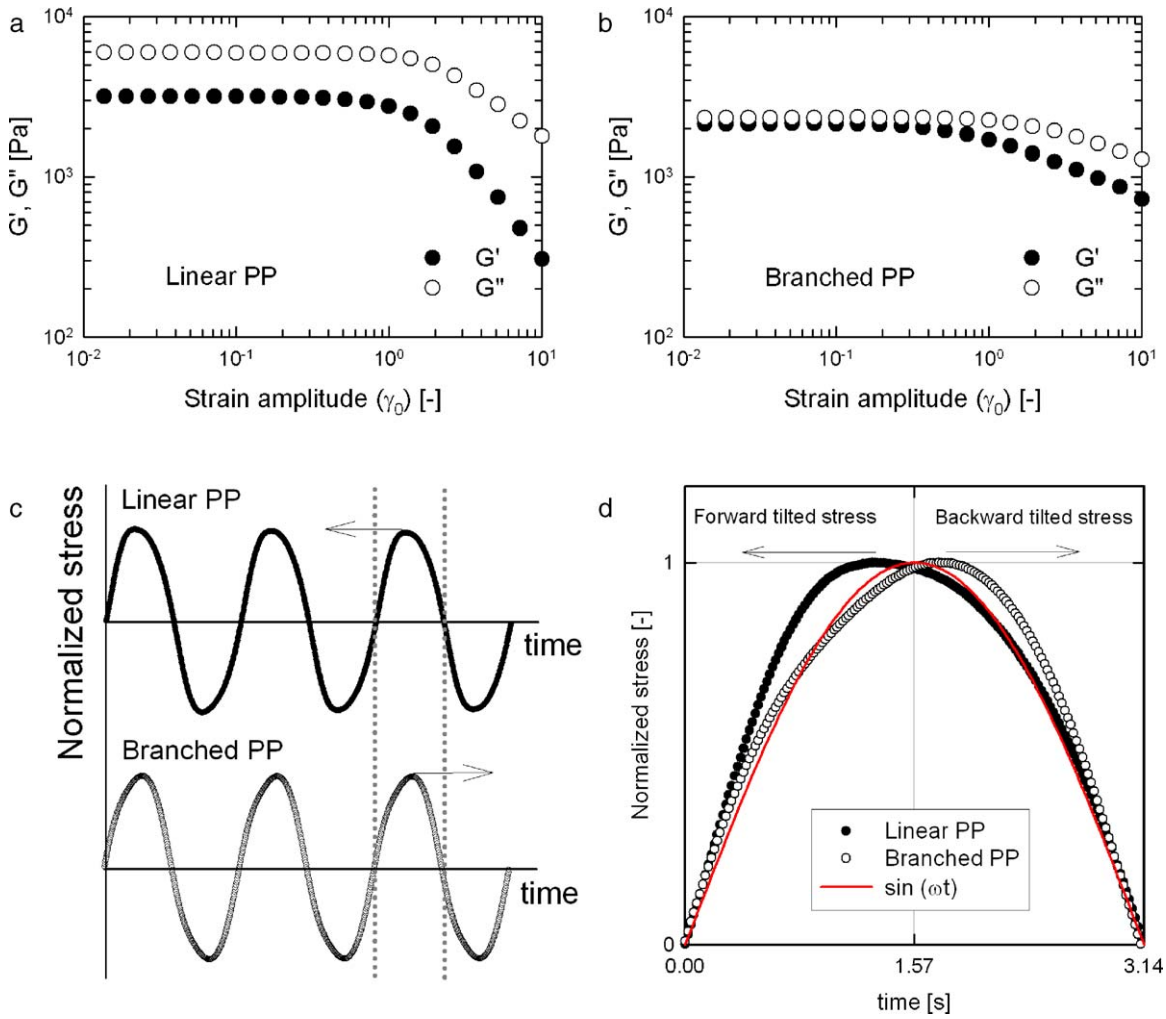

Fig. 6. The viscoelastic moduli $G'(\gamma_0)$ and $G''(\gamma_0)$ at $\omega = 1$ rad/s and $T = 180\,^{\circ}C$ for two different Polypropylene (PP) samples are shown, (a) linear PP and (b) branched PP. Both linear PP and branched PP display LAOS type I behavior (strain thinning). However the stress waveform shapes of the linear PP and branched PP samples are different. (c) The oscillatory stress for linear and branched PP at strain amplitude, $\gamma_0 = 7.19$. Both stress shapes are distorted from a single sinusoidal shape. (d) Magnified view of the stress data: linear PP responds with a "forward tilted stress" shape whereas the branched PP displays a "backward tilted stress" shape [95]. This difference in the shape of the waveform corresponds to different polymer topology, i.e. linear vs. branched chain structure [38].

the cause of loss modulus overshoot arise because the specific flow-induced microstructure depends on the particular material under investigation. This indicates that the leading-order descriptions of nonlinear viscoelasticity (i.e. the first-harmonic viscoelastic moduli) are not sufficient to explain the flow-induced microstructure. It is therefore necessary to investigate the higher harmonic contributions to the nonlinear stress response (quantitative methods for analyzing these differences are discussed in Section 4). In Fig. 6 below, we will present some examples of complex fluids that display the same leading-order LAOS type behavior but involve different distortions (higher harmonics) of the shear stress waveform under LAOS.

3.2.4. Type IV (strong strain overshoot)

For some material systems, e.g. associative polymer solutions, both G' and G'' may exhibit an overshoot at intermediate strain amplitude [93]. For associative polymer solutions this LAOS type IV behavior seems to be related to the strength of the intermolecular interaction energy which is weaker than the case of type II (strain hardening), but stronger than the case of type III in which only G'' shows overshoot. Such interactions may exist between hydrophobic groups or large micellar cluster microstructures. This type IV behavior is observed when both the creation and loss rate parameter are positive ($a > 0$, $b > 0$) and the creation rate, a, is limited to values of $b < a < 2b$. As the nonlinear creation rate parameter a increases, the maximum in G' and G'' becomes more pronounced. This type IV response is observed less often than type III.

These four generic types of leading order LAOS behavior have also been suggested by network theory [64,65]. We note that other classes of behavior have also been observed which look like a variation or combination of these four types, e.g. a local minimum of G' and G'' followed by strain hardening of both moduli [98–100], or a

local minimum of G' and G'' followed by a local maximum of G' and G'' [6,79,101]. Ahn et al. [63–65] concluded that the LAOS behavior of each class of fluid is closely related to its microstructure. Factors that influence the nonlinear response include molecular interactions and polymer topology. LAOS tests can help classify complex fluids and also provide information on the nonlinear evolution of fluid microstructure which may be unavailable with conventional rheological measurements.

3.3. Nonlinear shear stress waveforms

The viscoelastic moduli $G'(\gamma_0)$ and $G''(\gamma_0)$ provide only a leading order characterization of a material (i.e. the first harmonic contribution). Higher-order contributions, and nonlinear stress waveforms, can be used to further distinguish and investigate viscoelastic materials. Oscillatory stress waveforms are often (and in our opinion, should always be) available from commercial rheometers. In this section we demonstrate that even qualitative visual comparison of stress waveforms can be used to help distinguish materials (Figs. 6 and 7). We also present a survey of various waveform shapes which can be observed in LAOS tests (Figs. 8–13). The nonlinear waveforms represented visually in this section can also be thoroughly quantified with the methods discussed in Section 4.

Fig. 6 shows an example of how the raw oscillatory stress waveforms can distinguish two commercial polypropylene (PP) melts, one with a linear polymer chain topology and the other consisting of branched polymer chains [38]. Both linear and branched PP display strain thinning behavior when represented simply in terms of strain-amplitude-dependent moduli $G'(\gamma_0)$ and $G''(\gamma_0)$, i.e. LAOS type I (Fig. 6a and b). However, the nonlinear stress waveforms of the molten linear PP and branched PP samples are different (Fig. 6c and d). The linear PP melt displays a "forward tilted stress" shape whereas the branched PP melt displays a "backward tilted stress" shape [38,95]. The "forward tilted stress" shape was observed in the case of polymer melts and solutions with a linear chain structure whereas the "backward tilted stress" shape was observed for suspensions and polymer melts with branched chains [95]. Future studies of numerical simulations for branched structures (e.g. using the pom-pom constitutive model) are needed to fully understand this behavior.

Consideration of nonlinear stress waveforms can also be used to understand the difference between 4 wt% aqueous solution of Xanthan gum (XG) and the hard gel formed by a poly(ethylene oxide)–poly(propylene oxide)–poly(ethylene oxide) (PEO–PPO–PEO) 20 wt% solution. These materials show the same generic LAOS type III behavior of weak strain overshoot (Fig. 7a and b), however the stress waveforms take distinctively different shapes (Fig. 7c and d). The molecular structure of Xanthan is based on a linear 1,4-β-D-glucose backbone with charged trisaccharide side chains on every second residue [63]. In aqueous solution at 25 °C, the backbone of Xanthan is disordered but highly extended, as a result of electrostatic repulsion from the similarly charged groups on the side chains. Because of this highly extended structure, the molecules may align even at low concentration and associate (partly due to hydrogen bonding and charges) to form a weakly structured gel-like material [102]. In contrast, the microdomain of a hard gel for PEO–PPO–PEO is a close-packed (cubic) array of micelles. The "rectangular" stress waveform shapes for the PEO–PPO–PEO solution (Fig. 7d) can be related to the microstructure reversibly "sticking and slipping" where the "stick" comes from the short range interaction potential between hard spheres and "slip" occurs when layers slide over one another and destroy the stacking sequence [6]. Even though the two complex fluids display the same LAOS type III behavior, i.e. the same leading-order nonlinear features, LAOS deformation results in different flow-induced microstructure evolution that can be distinguished by the higher-order nonlinearities and different shapes of the nonlinear stress waveforms.

From these two simple examples, it is clear that analyzing the shape of the nonlinear stress response provides more structural insight than simply considering the leading order characterization $G'(\gamma_0)$ and $G''(\gamma_0)$. This is because the moduli $G'(\gamma_0)$ and $G''(\gamma_0)$ reflect only the 1st harmonic contribution from Eq. (9) and (10). Of course, a wide array of waveform shapes can be observed with LAOS. What follows is a selection of some canonical shapes observed in nonlinear shear stress waveforms.

From the mathematical descriptions of LAOS, e.g. Eq. (8), it is clear that higher harmonic contributions induce non-sinusoidal stress waveform shapes. The 3rd harmonic is the predominant determining factor controlling the stress shape, since subsequent higher order terms typically decay rapidly. Here we illustrate various distortions of the shear stress signal which result from varying the 3rd harmonic phase angle, neglecting all higher harmonic contributions (see also Fig. 26 and Section 4.4 for a related discussion on interpreting the phase angle of the 3rd harmonic, which is enabled by the Chebyshev polynomial representation of decomposed stress).

From Eq. (8), both the intensity and the phase angle of the 3rd harmonic contribution can be quantified. Neidhöfer et al. [103] analyzed the stress signal by a shift in time, substituting time t by $t = t' - \delta_1/\omega$, so that higher harmonics of stress were referenced to the first-harmonic stress response, rather than the input strain. Within this framework Eq. (8) is reformulated as follows,

$$\begin{aligned} \sigma(t') &= \sigma_1 \sin(\omega t') + \sigma_3 \sin(3\omega t' + \delta_3') \\ &\quad + \sigma_5 \sin(5\omega t' + \delta_5') + \cdots, \\ \gamma &= \gamma_0 \sin(\omega t) = \gamma_0 \sin(\omega t' - \delta_1) \end{aligned} \tag{18}$$

where $\delta_n' = \delta_n - n\delta_1$ is the nth relative phase angle and δ_1 is the 1st phase angle ($0° \le \delta_1 \le 90°$) which determines the stress response as elastic ($\delta_1 = 0°$), viscoelastic, or viscous ($\delta_1 = 90°$). For purposes of self-consistent notation, we use a "sine" notation in Eq. (18) rather than the "cosine" notation from Neidhöfer et al. [103], however the principle is same. For illustrative purposes let us assume that the 3rd harmonic contribution is exactly 10% of the 1st harmonic contribution ($\sigma_3/\sigma_1 = I_3/I_1$) and the other harmonics higher than the third are negligible, then Eq. (18)

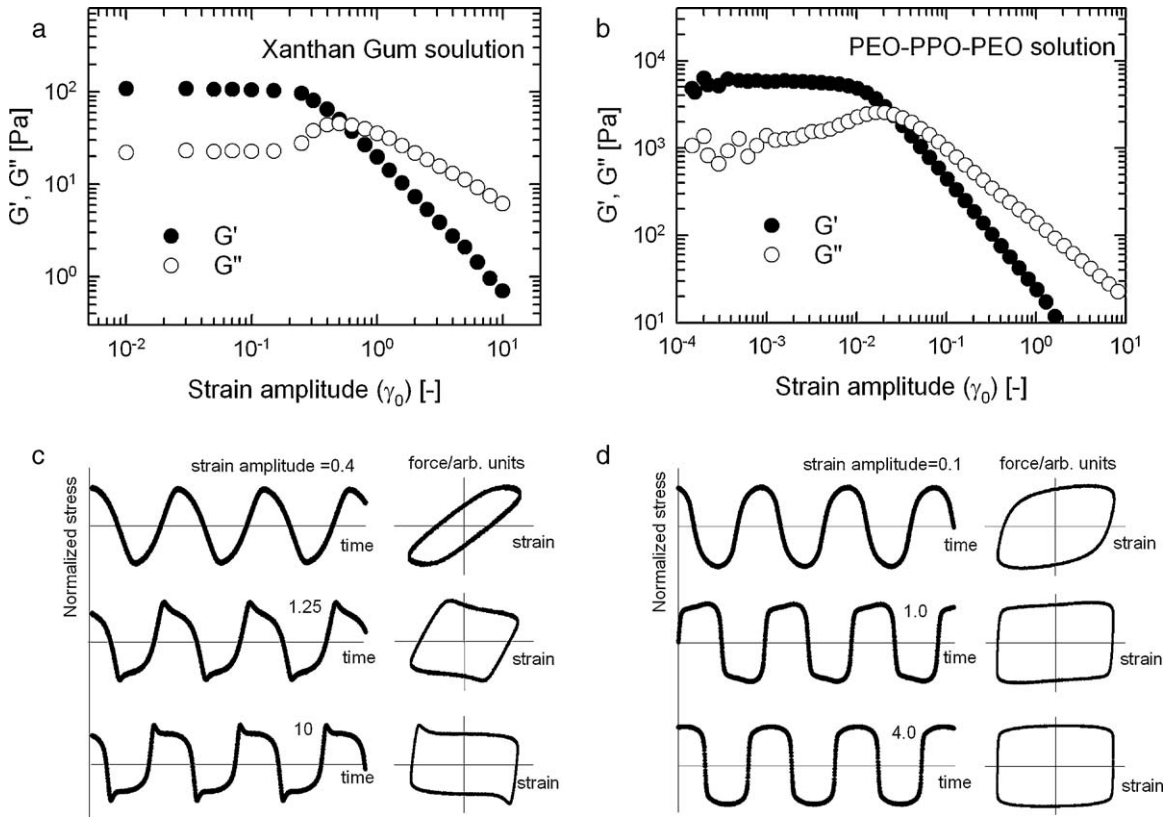

Fig. 7. The viscoelastic moduli $G'(\gamma_0)$ and $G''(\gamma_0)$ for (a) Xanthan gum 4 wt% aqueous solution at $\omega = 1$ rad/s and $T = 25\,^{\circ}$C and (b) hard gel of PEO–PPO–PEO triblock 20 wt% aqueous solution at $\omega = 1$ rad/s and $T = 26\,^{\circ}$C are shown. Both aqueous solutions display LAOS type III (weak strain overshoot) behavior. However, the shapes of the nonlinear stress waveforms are markedly different. The stress data and Lissajous patterns are shown in (c) Xanthan gum 4% aqueous solution (saw tooth shape) and (d) hard gel of PEO–PPO–PEO triblock 20% aqueous solution (rectangular shape). The different shape of these stress waveforms originates from different microstructures. Reproduced by permission of Hyun et al. [95], copyright (2003) of the Korean Society of Rheology and the Australian Society of Rheology.

becomes

$$\frac{\sigma(t')}{\sigma_1} = \sin(\omega t') + 0.1\,\sin(3\omega t' + \delta_3')$$
$$\gamma = \gamma_0\,\sin(\omega t) = \gamma_0\,\sin(\omega t' - \delta_1) \tag{19}$$

By changing the relative third-harmonic phase angle δ_3' in Eq. (19) from 0° to 360°, we can investigate the effect of the 3rd harmonic contribution on the stress signal. The distorted shear stresses are plotted as a function of time at four different phase angles ($\delta_3' = 0°, 90°, 180°, 270°$) in Fig. 8. Various canonical shapes in the shear stress are observed, including rectangular, "backward" tilted, triangular, and "forward" tilted shapes. Leblanc [59,60] suggested a quantifying method for the "backward" and "forward" tilted shapes of shear stress by comparing quarter cycle integrations of shear stress data as a function of time. The first quarter stress signal integration Q1 (e.g. integration from 0 s to 1.57 s in Fig. 6d) is compared to the second quarter stress integration Q2 (e.g. integration from 1.57 s to 3.14 s in Fig. 6d). The ratio $Q1/Q2 = 1$ for the case of no tilting, and allows clear distinction between "forward" tilted ($Q1/Q2 > 1$) and "backward" tilted ($Q1/Q2 < 1$) waveforms. This method is used to distinguish unfilled polymer and filled polymer, e.g. carbon black rubber compounds [60]. This method will be introduced in more detail in Section 5.

A graphical representation that is more amenable to rapid qualitative evaluation is the use of a closed loop plot (Lissajous curve) of stress vs. strain or stress vs. rate of strain [4]. For the full reconstruction of a Lissajous curve, we also calculated strain using three different 1st harmonic phase angle, $\delta_1 = 0°$ (elastic), 45° (viscoelastic), and 90° (viscous) in Eq. (19). The Lissajous curves are plotted in Fig. 9. This is a simple example to visualize how the 3rd harmonic phase angle contributes to the shapes of the stress waveforms in either the time domain (stress vs. time) or the deformation domain (Lissajous curves of stress vs. strain). Even though these equations (Eqs. (18) and (19)) have no direct information regarding microstructure in a complex fluid, this plot visually demonstrates how higher harmonic contributions, especially the 3rd harmonic, can affect the measured output for a nonlinear viscoelastic material. The variety of theoretical stress waveforms shown in Figs. 8 and 9 can also be observed in both experimental measurements and simulations of various complex fluids. The challenge for the rheologist is to connect such measurements to changes in the material microstructure.

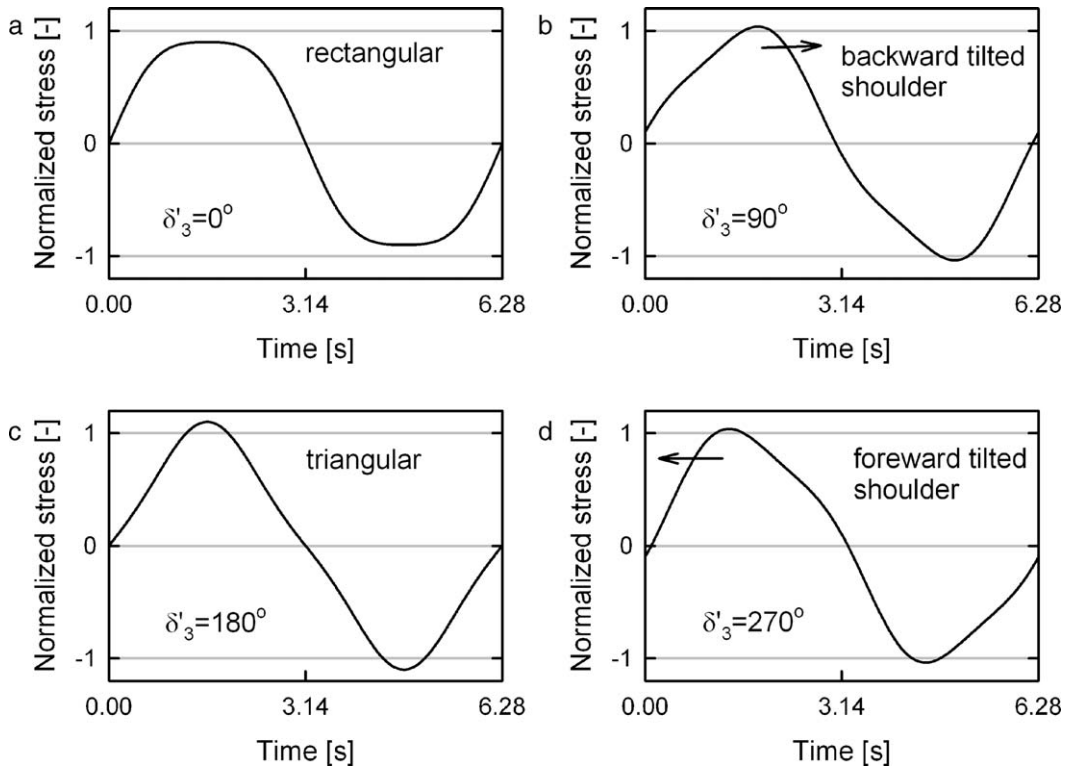

Fig. 8. The normalized stress data at different values of the phase angle for the third harmonic from Eq. (19) at a fixed frequency $\omega = 1$ rad/s: (a) $\delta'_3 = 0°$, (b) $\delta'_3 = 90°$, (c) $\delta'_3 = 180°$, (d) $\delta'_3 = 270°$. There are various shapes of the stress curve, including rectangular, triangular, backward tilted, and forward tilted waveforms. Reproduced by permission of Hyun et al. [95], copyright (2003) of the Korean Society of Rheology and the Australian Society of Rheology.

Experimental examples of LAOS shear stress responses are now described, and shown in Figs. 10–13. Many classes of complex fluids exhibit nonlinear and distorted stress waveforms under LAOS, for example: polymer melts [38,62], polymer blends [104], polymer solutions [72,95,105], block copolymer solutions [6,49,106], block copolymer melts [107], suspensions [5,12,14,51,108], ER materials [91,109], MR (magnetorheological) fluids [110], biological materials [111], wormlike micelle solutions [69] and food products [100,112], just to mention some prominent examples. In Fig. 10, several distorted, non-sinusoidal shear stress waveforms are shown as a function of time for different complex fluids under LAOS including polymer and block copolymer solutions and polymer melts. The Lissajous curves (stress vs. strain) of various complex fluids subjected to LAOS with a range of strain amplitudes are also displayed in Fig. 11. The experimentally measured LAOS response of a micellar solution is shown in Fig. 12, in which the Lissajous curves are positioned in a Pipkin space defined by the two parameters which define an oscillatory test: the imposed strain amplitude γ_0 (y-axis) and the frequency ω (x-axis) [69]. For the case of linear viscoelastic behavior the parametric loops of stress vs. strain are ellipses, with a minor axis that narrows with increasing frequency, i.e. less energy is dissipated in the high-frequency elastic region. Fig. 13 shows the experimentally measured LAOS response of a suspension system, in which the Lissajous curves are also positioned in a Pipkin space according to the imposed strain amplitude (y-axis) and frequency (x-axis). In contrast to the micelle solution (Fig. 12), the Lissajous curves for the suspension system (Fig. 13) do not flatten, and the suspension is dissipative even at the highest frequencies shown. The evolution in the shape of the distorted stress waveforms can be related with systematic changes in the internal microstructure of the material or the polymer topologies (linear or branched chain). While visual investigations such as those presented in Figs. 8–13 are helpful to give an overview of nonlinear viscoelastic response, quantitative methods are also necessary for analyzing these nonlinear shear stress waveforms. Several different quantitative methods will be reviewed in Section 4.

3.4. Nonlinear normal stress difference

In addition to a shear stress, viscoelastic normal stresses can also develop in response to shearing deformations of large strain amplitude [1]. In this subsection we consider the fundamental features of normal stress waveforms resulting from oscillatory shear. In oscillatory shear flow analysis with quasilinear constitutive models such as the Oldroyd-B equation it can be shown that the normal stress difference oscillates at twice the imposed frequency (2ω) around a nonzero mean value that varies quadratically with strain amplitude γ_0 [1,2,4,113]. This result would be expected from symmetry considerations because the normal stress difference is a nonlinear material response that is induced by the imposed shear but is independent of the shear direction, $N_i[\gamma(t), \dot{\gamma}(t)] = N_i[-\gamma(t), -\dot{\gamma}(t)]$, where N_i

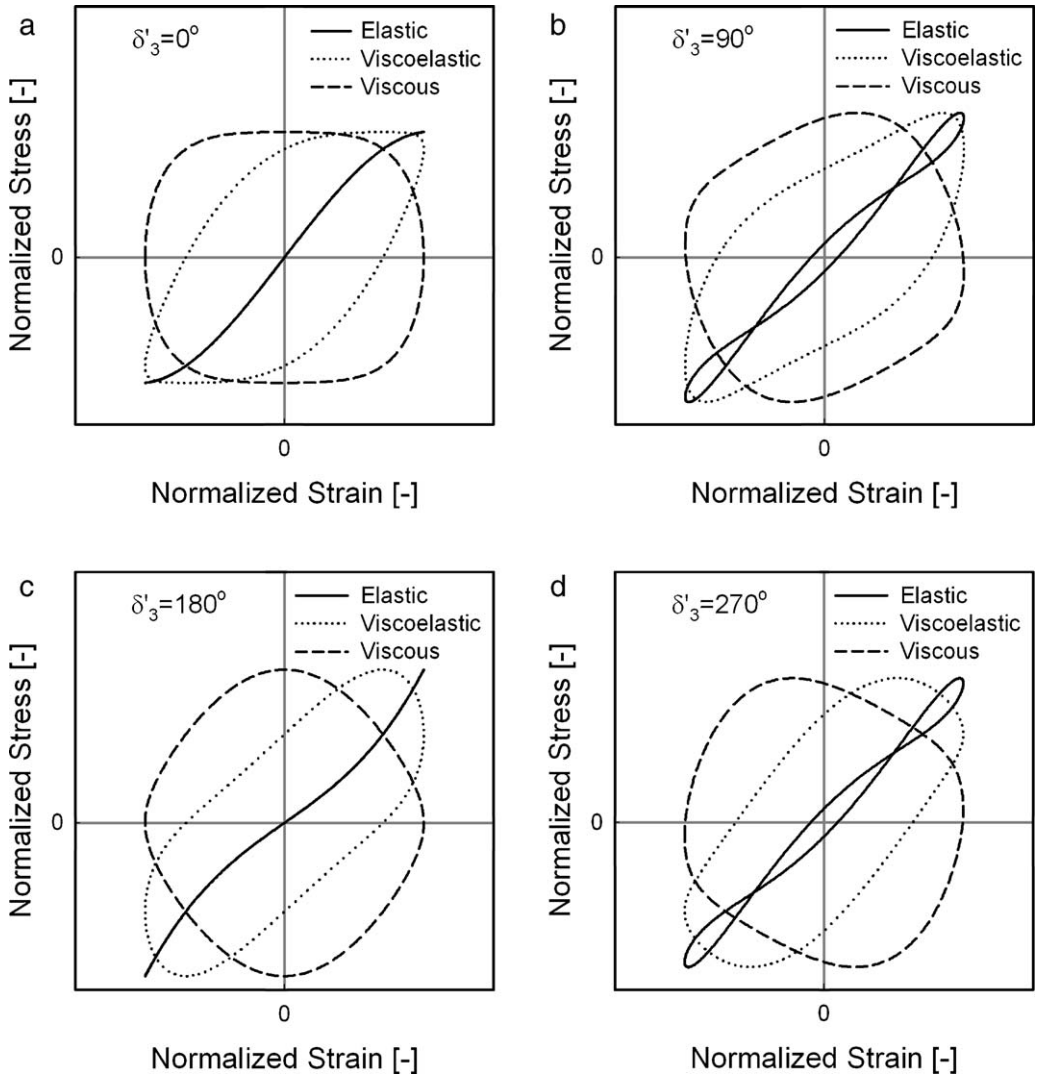

Fig. 9. The normalized Lissajous curve (stress (y axis) vs. strain (x axis)) at different third relative phase angle: (a) $\delta'_3 = 0^\circ$, (b) $\delta'_3 = 90^\circ$, (c) $\delta'_3 = 180^\circ$, (d) $\delta'_3 = 270^\circ$ from Eq. (19) at a fixed frequency $\omega = 1$ rad/s with $\sigma_3/\sigma_1 = I_3/I_1 = 0.1$ in Eq. (19). For calculation of strain, three different 1st phase angles are used, $\delta_1 = 0^\circ$ (Elastic), 45° (Viscoelastic), and 90° (Viscous) in Eq. (19). (See also Section 4.4 and Fig. 26 which describes alternative third-harmonic phase angle interpretations via Chebyshev polynomials.)

is either the first ($i = 1$) or second ($i = 2$) normal stress difference. The normal stress differences under oscillatory shearing conditions can be written as the sum of a constant term and an oscillating term with phase angle ($\delta_{i,2}$). The oscillatory term can itself be decomposed into two components, by analogy with the representation of the storage and loss moduli (G', G''),

$$\begin{aligned} N_i &= N_{i,0} + N_{i,2}\,\sin(2\omega t + \delta_{i,2}) = N_{i,0} + N'_{i,2} + N''_{i,2} \\ N'_{i,2} &= N_{i,2}\,\cos\,\delta_{i,2}\,\sin(2\omega t) \\ N''_{i,2} &= N_{i,2}\,\sin\,\delta_{i,2}\,\cos(2\omega t), \quad i = 1 \;\text{ or }\; 2 \end{aligned} \tag{20}$$

The second normal stress difference ($i = 2$) in steady shear flow is typically smaller than the first ($i = 1$) by roughly an order of magnitude [1] and is difficult to measure. Therefore, we only focus on the first normal stress difference in this review. In the SAOS regime, the first normal stress difference can be calculated from the shear properties (G', G'') by the phenomenological models as follows [1,72,114,115]:

$$\begin{aligned} \frac{N_{1,0}}{\gamma_0^2} &= G'(\omega) \\ \frac{N'_{1,2}}{\gamma_0^2} &= \frac{N_{i,2}}{\gamma_0^2}\,\cos\delta_{i,2} = \left[G''(\omega) - \frac{1}{2}G''(2\omega)\right] \\ \frac{N''_{i,2}}{\gamma_0^2} &= \frac{N_{i,2}}{\gamma_0^2}\,\sin\delta_{i,2} = \left[-G'(\omega) + \frac{1}{2}G'(2\omega)\right] \end{aligned} \tag{21}$$

However, the physical meaning of the first normal stress difference can be complicated and obscured due to the frequency-doubled terms of shear moduli (G', G''). The first normal stress difference can be much larger in magnitude

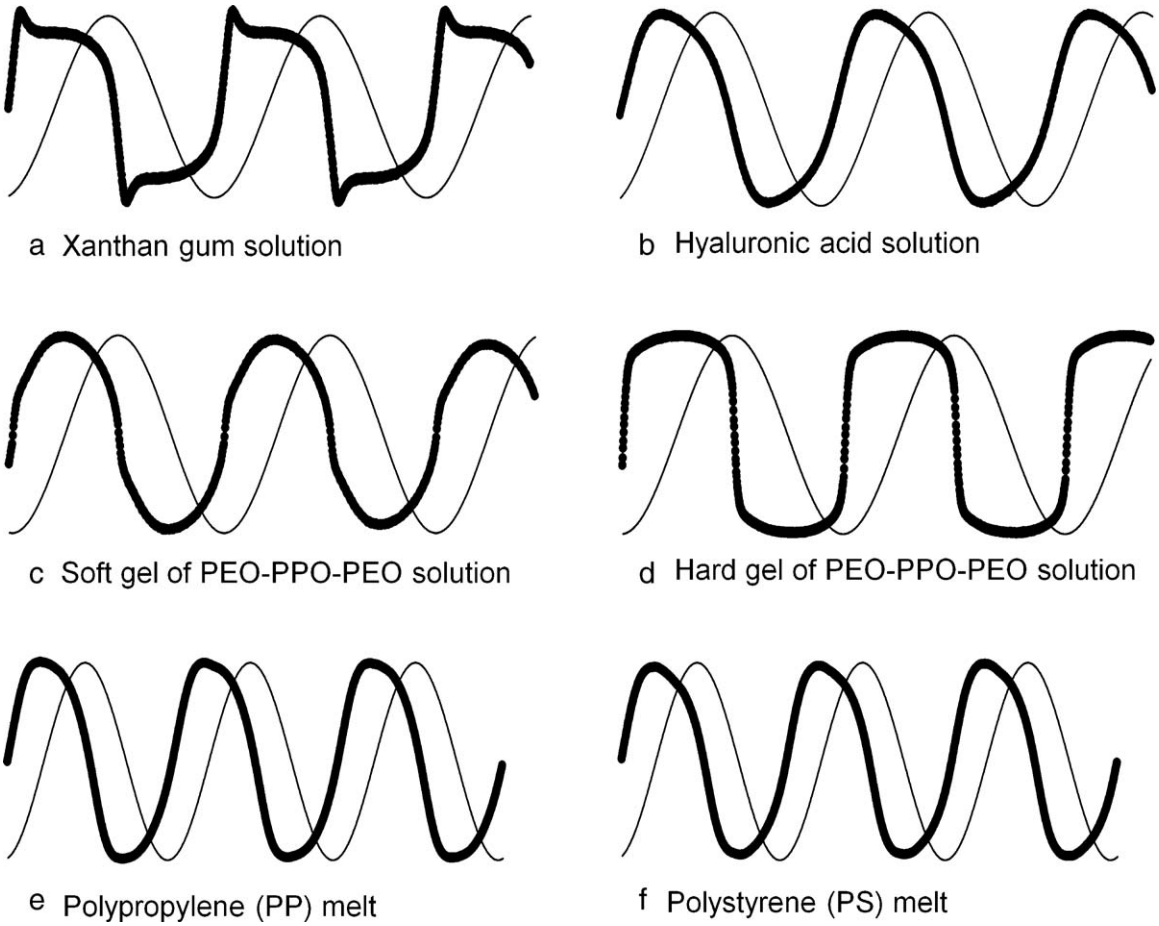

Fig. 10. Stress curves (●) and applied strain curves (—) as a function of time for various complex fluids at large strain amplitude and frequency 1 rad/s. (a) Xanthan gum 4 wt% aqueous solution at strain amplitude $\gamma_0 = 10$. (b) Hyaluronic acid 1% aqueous solution at strain amplitude $\gamma_0 = 7.2$. (c) soft gel of PEO–PPO–PEO triblock 20 wt% aqueous solution at strain amplitude $\gamma_0 = 10$. (d) Hard gel of PEO–PPO–PEO triblock 20% aqueous solution at strain amplitude $\gamma_0 = 4$. (e) Polypropylene (PP) melt at strain amplitude $\gamma_0 = 10$. (f) Polystyrene (PS) melt at strain amplitude $\gamma_0 = 10$.

than the shear stress at large strain amplitude [72,77]; conversely, it is not easy to measure at small and intermediate strain amplitudes because the normal forces are quadratic with respect to γ_0. Precise measurement of normal stresses in oscillatory shear flow recently became feasible and has enabled investigation of nonlinear normal stress responses to LAOS.

In the LAOS regime, the normal stress differences oscillate with additional higher harmonics. These are similar in principle to higher harmonics of the shear stress but instead contain only *even* harmonic contributions, because the normal stress difference has no dependence on the imposed shear direction as mentioned before. This symmetry is in contrast to the shear stress behavior ($\sigma[-\gamma(t), -\dot{\gamma}(t)] = -\sigma[\gamma(t), \dot{\gamma}(t)]$, i.e. Eq. (3)). The nonlinear normal stress differences also can be described using Fourier series, similar to the treatment of shear stress (compare to Eq. (8)):

$$N_i(t) = \sum_{k=0}^{\infty} N_{i,2k} \sin(2k\omega t + \delta_{i,2k}) = N_{i,0} + \sum_{k=1}^{\infty} N_{i,2k} \sin(2k\omega t + \delta_{i,2k}), \quad i = 1 \text{ or } 2 \qquad (22)$$

The nonlinear normal stress differences can also be defined as the sum of a constant term and an oscillating term like Eq. (20). The contribution at zero frequency ($N_{i,0}$, zero harmonic) indicates the non-zero mean value, i.e. the bias value. Some care must be taken with the nomenclature and the term '*nonlinear*.' Normal stress differences are inherently a nonlinear phenomenon even in the limit of small deformations, e.g. the first normal stress difference $N_1(\dot{\gamma})$ in steady shear flow reaches proportionality with $\dot{\gamma}^2$ in the limit of small shear rate. In this limit $N_1(\dot{\gamma})/\dot{\gamma}^2 = 2\eta_0^2 J_s$, with J_s the linear recoverable compliance after steady shear flow and η_0 the zero shear viscosity at linear region. In SAOS (small amplitude oscillatory shear), the appropriately scaled $N_1(t)/\gamma_0^2$ is not a function of strain amplitude. As strain amplitude increases, the higher harmonics appear in the Normal stress differences. Our interest is this deviation from small deformation behavior, therefore we will use the term '*nonlinear*' normal stress difference to refer specifically to the higher harmonic contributions at 4ω, 6ω, . . ., in response to LAOS deformation.

Due to experimental difficulties, nonlinear normal stress differences in LAOS have been studied far less than the nonlinear shear stress. As a result, the investigation of

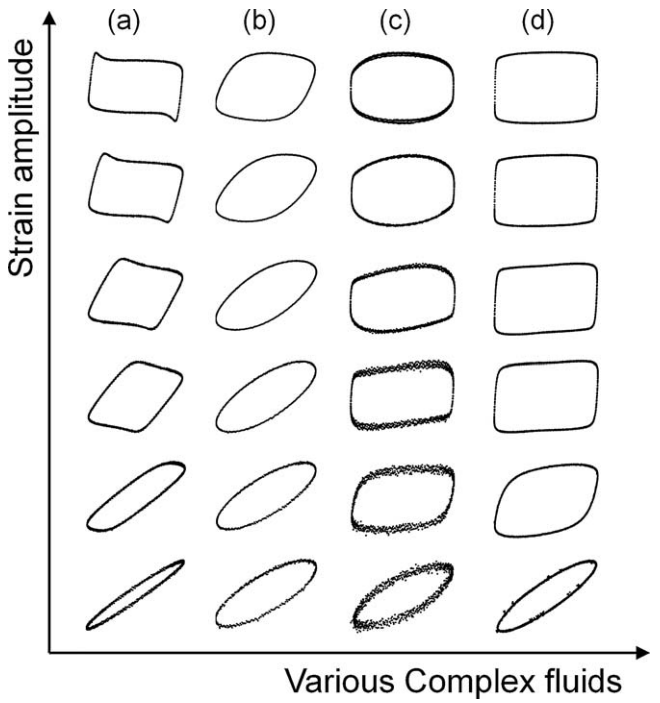

Fig. 11. The Lissajous curves (stress (y axis) vs. strain (x axis)) (●) of various complex fluids, arranged from small strain amplitude to large strain amplitude at a fixed frequency, 1 rad/s: (a) Xanthan gum 4% aqueous solution, (b) hyaluronic acid 1% aqueous solution, (c) soft gel of PEO–PPO–PEO triblock 20% aqueous solution, (d) hard gel of PEO–PPO–PEO triblock 20% aqueous solution.

a nonlinear (non-sinusoidal) first normal stress difference has a shorter history. Vrentas et al. [116] measured the first normal stress difference in LAOS at various frequencies for a polystyrene solution and simply compared with results obtained in steady shear experiments to check the validity of the K-BKZ constitutive equation. Oakley and Giacomin [117] analyzed the higher harmonics of the first normal stress difference, which were previously not obtainable, in

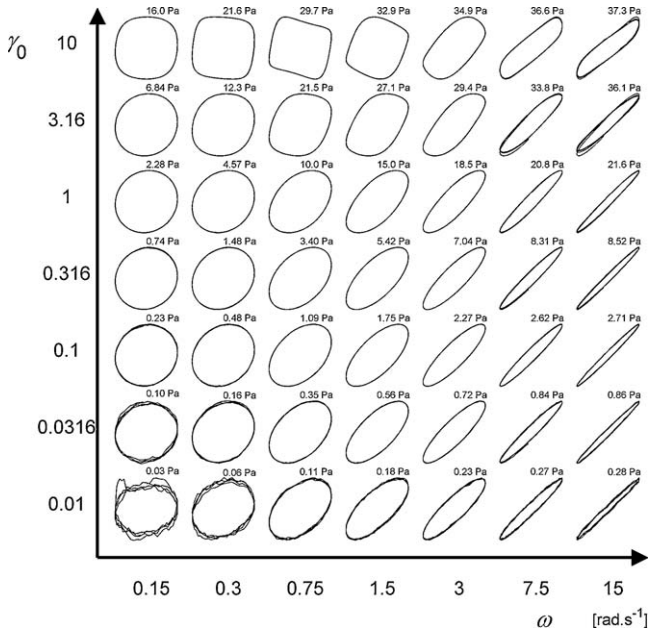

Fig. 12. Raw LAOS data for a micellar solution, generated from experimental oscillatory tests, shown as normalized elastic Lissajous curves of stress $\sigma(t)$ vs. strain $\gamma(t)$. Each trajectory is positioned in a Pipkin space according to the imposed values of strain amplitude γ_0 and frequency ω. Solid lines are total stress $\sigma(t)/\sigma_{max}$ vs. $\gamma(t)/\gamma_0$. The maximum stress σ_{max} is indicated above each curve. Reproduced by permission of Ewoldt et al. [69], copyright (2009) of The Society of Rheology.

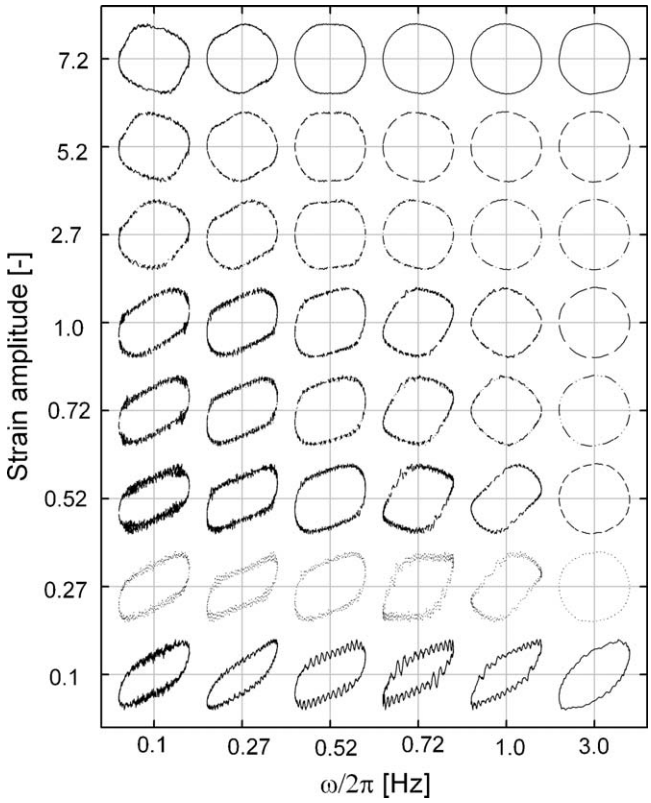

Fig. 13. Raw LAOS data for a highly concentrated suspension system (50 wt% PMMA particle (100 nm radius) in paraffin oil), generated from experimental oscillatory tests, shown as normalized elastic Lissajous curves of stress $\sigma(t)$ vs. strain $\gamma(t)$. Each trajectory is positioned in a Pipkin space according to the imposed values of strain amplitude γ_0 and frequency ω.

melt flow using a home built sliding plate rheometer (SPR). Atalık and Keunings [77] reported that a few odd harmonics could be introduced in the first normal stress difference by fluid inertia in LAOS. Even harmonic responses of the normal stress differences under LAOS were critically discussed using the predictions of a single mode Giesekus model and compared to experimental results [72]. Analysis of the normal stress difference in LAOS can lead to rheological insight for certain complex fluids or soft matter. For example, the structure of highly elastic materials such as gels and foams can be explained by pronounced oscillatory first normal stress differences [118,119]. Additionally, the response of the first normal stress difference for polymer solutions in LAOS has been compared with transient network theory [120], and the non-sinusoidal form of the response in the first normal stress difference has been shown to sensitively reflect the orientation and relaxation of fibers in polymer melt flow [121].

In Fig. 14 we show the first normal stress difference and shear stress waveforms experimentally measured for a Boger fluid undergoing LAOS with increasing strain amplitude at a fixed frequency 1 rad/s. The first normal stress oscillates with twice the imposed frequency (2ω) about a non-zero mean value, whereas the shear stress oscillates with the imposed frequency (ω) about zero mean. A Boger fluid is typically composed of a low concentration of high molecular-weight flexible polymer dissolved in a very viscous Newtonian liquid, such as a low molecular-weight polymer or oligomer. The Boger fluid investigated here is composed of 0.5 wt% of Polyisobutylene (PIB) with a high molecular weight of 6×10^5 g/mol dissolved in polybutylene (PB) with a low molecular weight of 920 g/mol. The viscosity is nearly independent of shear rate, therefore elastic effects can be separated from viscous effects in viscoelastic flows [122]. Fig. 15 compares the LAOS responses of an elastic Boger fluid with constant viscosity and a polymer solution with strong shear-thinning viscosity. Different constitutive equations are used for the Boger fluid and the shear-thinning polymer solution to compare the two materials. The upper convected Maxwell (UCM) model (see Appendix C) predicts a quadratic variation of the first normal stress difference and a constant viscosity, and is thus mathematically suitable for displaying the material response of a Boger fluid in LAOS. The Giesekus model with a single nonlinear coefficient α is an extension of the UCM model (see Appendix C), and is appropriate for modeling the shear-thinning polymer solutions [123].

For the Boger fluid (Fig. 15b), no distortion of the shear stress and the normal stress difference is observed even at large strain amplitude, because the viscosity of the Boger fluid (BF) is nearly independent of shear. The first normal stress difference and the shear stress for the UCM model (Fig. 15a) also show no distortion behavior at large strain amplitude due to the absence of nonlinear terms in the constitutive equation. Because of the quasi-linear nature of the UCM model, the oscillatory first normal stress difference

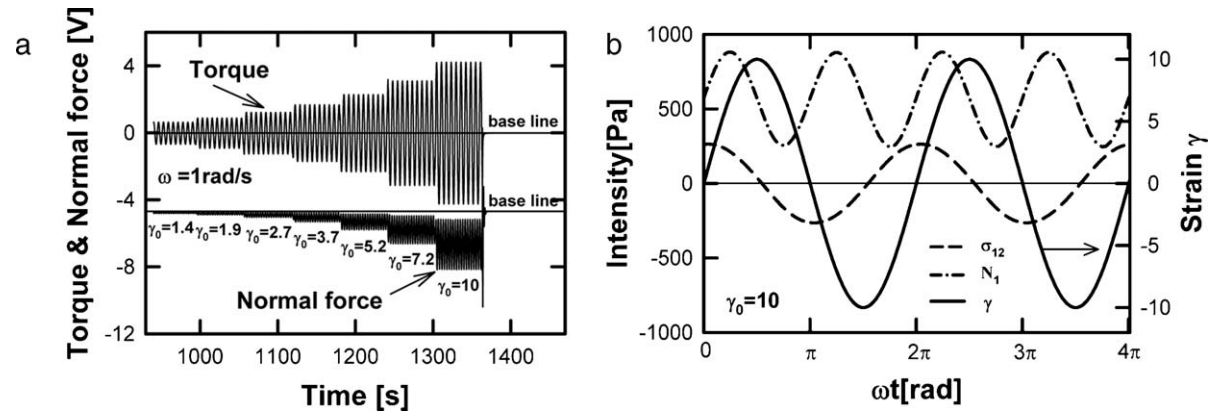

Fig. 14. (a) Raw torque and normal force signal of a Boger Fluid (0.5 wt% of PIB in PB, PIB with a molecular weight 6×10^5 g/mol and PB with a molecular weight 920 g/mol) during the strain sweep test (increasing strain amplitude from $\gamma_0 = 1.38$–10) at fixed frequency of 1 rad/s, and (b) strain (γ), shear stress (σ_{12}) and first normal stress difference (N_1) at the strain amplitude of $\gamma_0 = 10$. The rheological measurements were performed using a strain-controlled rheometer, ARES (100NFRT) with cone-and-plate (radius: 25 mm, angle: ~5°).

can be uniquely divided into three terms, given by Eq. (20). On the contrary, the simulation results of Giesekus model (Fig. 15c) show highly distorted waveforms for the first and second normal stress differences and the shear stress. As the nonlinear parameter α increases, shear thinning becomes pronounced. The concentrated polymer solution with strong shear thinning behavior also displays distorted, non-sinusoidal behavior for both the first normal stress difference and shear stress under LAOS (Fig. 15d). From this comparison of a constant viscosity elastic liquid (Boger

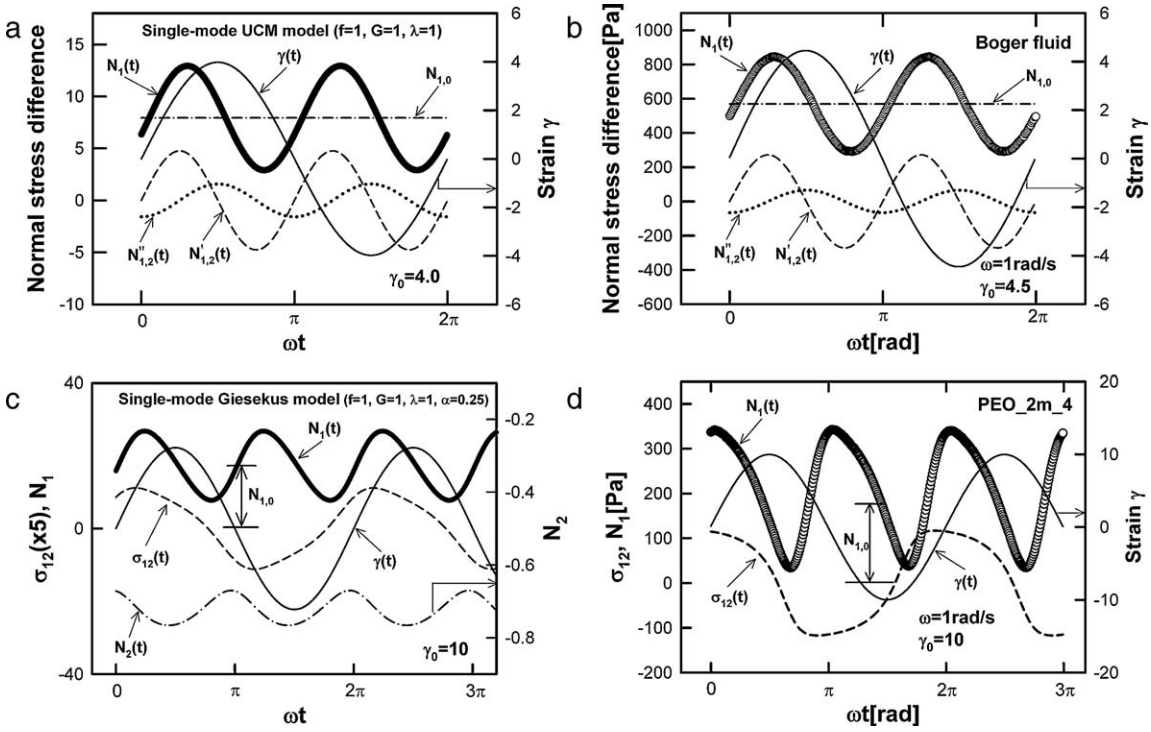

Fig. 15. (a) Shear strain (thin solid line) and first normal stress difference (thick solid line) as predicted by the UCM model (dimensionless parameters $f = 1$ (frequency), $G = 1$ (modulus), $\lambda = 1$ (relaxation time), $\gamma_0 = 4$). The first normal stress difference is decomposed into three parts; one for the non-zero mean value (dashed dot line) and the other two for the in-phase and out of phase oscillating terms (dashed line and dot line). (b) Shear strain (solid line), and first normal stress difference (open symbols) of a Boger fluid at the frequency 1 rad/s and strain amplitude $\gamma_0 = 4.5$. The first normal stress difference is also decomposed into three parts. (c) Shear strain (thin solid line), shear stress (dashed line), first normal stress difference (thick solid line), and second normal stress difference (dashed dot line) from the simulation results of a single mode Giesekus model based on the work of Nam et al. [72]. The related model parameters are $f = 1$, $G = 1$, $\lambda = 1$, and $\alpha = 0.25$ (nonlinear parameter). The shear stress is magnified by a factor of 10. (d) Shear strain (solid line), shear stress (dashed line), and first normal stress difference (open symbol) of an aqueous polyethylene oxide (PEO) soulution (concentration of 4 wt% with a molecular weight 2×10^6 g/mol) [124]. The strain amplitude is $\gamma_0 = 10$ and frequency is 1 rad/s.

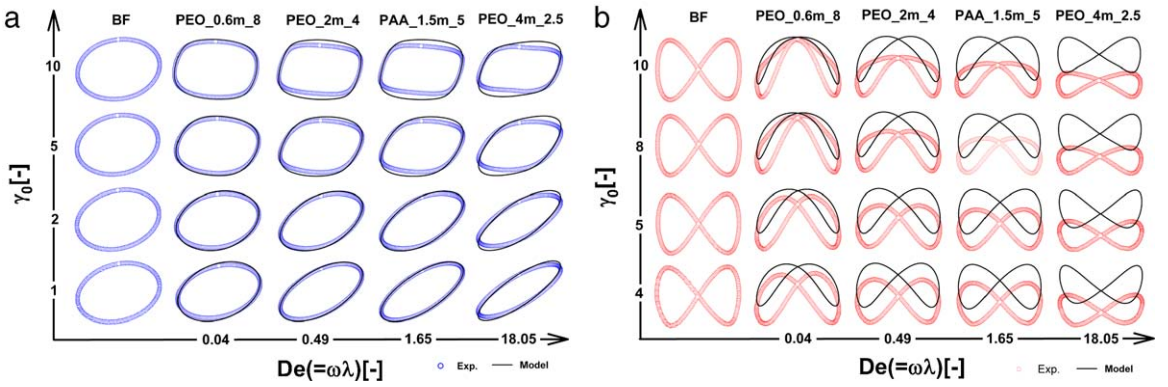

Fig. 16. The experimental Lissajous patterns obtained for various polymer solutions; BF (Boger fluid), PEO (polyethylene oxide) and PAA (polyacryl amide) solutions at a range of concentrations. (a) The loop for shear stress vs. strain, (b) the loop for first normal stress difference vs. strain. The results are arranged in a Pipkin space (strain amplitude vs. frequency ($De = \omega/\omega_c$, ω_c is crossover frequency at $G' = G''$)). For four aqueous polymer solutions, the experimental data (symbols) are compared with model data (lines). For the Boger fluid only the experimental data is shown.

fluid and UCM model) and a viscoelastic shear-thinning fluid (polymer solution and Giesekus model), it can be concluded that a viscoelastic shear-thinning fluid is more likely to show nonlinear behavior in the normal stress difference and shear stress at moderate Deborah number $De = \omega/\omega_c$ (ω_c is crossover frequency at $G' = G''$) compared to an elastic liquid with constant viscosity. In Fig. 16 we show the Lissajous curves of the periodic shear stress and first normal stress as a function of De for various entangled polymer solutions. Results for the Giesekus model are also shown as a function of De and strain amplitude [124,125].

From an experimental point of view, the aim of nonlinear oscillatory experiments is to investigate the progressive evolution of the non-sinusoidal behavior with increasing deformation, and to quantify the nonlinear material coefficients that characterize the material nonlinearity. Furthermore, it is desirable to correlate these nonlinear coefficients with physical changes in the microstructure or polymer topology. The descriptions of $G_1'(\gamma_0)$ and $G_1''(\gamma_0)$ presented so far have focused only on the evolution in the 1st harmonic terms and are thus the simplest quantitative method. However, such rankings discard information about the nonlinear stress shape which arises from the higher order odd harmonic terms (Figs. 8 and 9), for example the 3rd harmonic contribution. Several quantitative methods have been proposed for analyzing non-sinusoidal waveforms of shear and normal stresses. In the next section, we will review these techniques and summarize the relationship between different analytical methods.

4. Quantitative methods for analyzing nonlinear stress waveforms

Oscillatory stress waveforms can be analyzed from the perspective of two complementary coordinate frames. Traditionally, the most common analytical representation is the time-domain waveform $\sigma(t)$ (e.g. Figs. 8 and 10), which can be transformed into a Fourier series, and is discussed below in Sections 4.1 and 4.2. Alternatively, the stress response can be represented as a function of the strain $\gamma(t)$ and strain-rate $\dot{\gamma}(t)$, written within the deformation-domain as $\sigma[\gamma(t), \dot{\gamma}(t)]$ (e.g. the Lissajous curves in Fig. 11 which are a 2D projection of $\sigma(t)$ vs. $\gamma(t)$). This alternative representation within the deformation-domain is a fundamental aspect of Sections 4.3–4.5. After reviewing the current analytical methods, Section 4.6 and Table 3 summarize the comparative benefits of these two inter-related coordinate frame representations.

4.1. Fourier transform (FT)

A Fourier transformation represents a time dependent signal $s(t)$ with respect to the different frequencies $\omega/2\pi$, amplitudes, and phases in a spectrum $S(\omega)$. This section describes the principles of the Fourier transformation needed to implement Fourier Transform Rheology (FT-Rheology). More details are provided in Refs. [30,31,33].

A Fourier transformation represents the inherent periodic contributions to a time dependent signal and displays the corresponding amplitudes and phases (or real and imaginary part) as a function of frequency. To implement FT-Rheology, a half-sided, discrete, complex Fourier transformation is applied to the shear stress signal $\sigma(t)$. To obtain highly resolved, artifact-free spectra with a low noise level, the time signal has to be acquired with sufficient care. In particular, mechanical and electrical shielding are typically used in combination with data oversampling techniques [34,126] to increase significantly the quality of the raw time data (see Section 2). The Fourier transformation (FT) of any real or complex time signal, $s(t)$, and the corresponding inverse transform of a frequency dependent spectrum $S(\omega)$ are usually defined in the following way:

$$S(\omega) = \int_{-\infty}^{\infty} s(t) e^{-i\omega t}\, dt, \quad s(t) = \frac{1}{2\pi} \int_{-\infty}^{\infty} S(\omega) e^{+i\omega t}\, d\omega \tag{23}$$

In general the Fourier transformation is an invertible, linear, complex transformation over the infinite interval from $-\infty$ to $+\infty$. The FT is a linear mathematical transformation defined on any signal $s(t)$ which we use to quantify mechanical nonlinearities. By supplying a "monochromatic" or single input frequency, ω, we ensure that any output from the system at frequencies other than ω is asso-

ciated with nonlinearity in the system response. These two aspects should be clearly separated. Any linear superposition of different signals in the time domain will also lead to a linear superposition in the frequency domain since a Fourier Transformation is a mathematically linear operation.

The FT is inherently complex; thus even for a real time-domain data set $s(t)$, this transformation results in a complex spectrum $S(\omega)$ with real $R(\omega)$ and imaginary $I(\omega)$ components of the spectrum. The complex spectra can alternatively be presented as magnitude $m(\omega)$ and phase $\phi(\omega)$ spectra, where the inter-relation is given by $\tan\phi = I/R$ and $m = (R^2 + I^2)^{1/2}$. Applying the Euler relation $(\exp(i\phi) = \cos\phi + i\sin\phi)$, the basic definition in Eq. (23) can also be separated into a cosine- and sine transformation, commonly termed the Fourier cosine and Fourier sine transformation. A half-sided Fourier transformation corresponding to the case when the integration in Eq. (23) is only carried out in a semi-infinite domain, specifically from $t = 0$ to $t = +\infty$. This transform is most commonly used for experimental data since acquisition begins at a finite time.

In the case of discrete and digitized sampling, the data is taken point by point with a fixed increment t_{dw} (the dwell time, or inverse sampling rate) over a total acquisition time $t_{aq} = t_{dw}N$. Thus, both time and amplitude have discrete values. Since the peaks in the FT-Rheology spectrum are in principle infinitely narrow, a long acquisition time t_{aq} over multiple cycles will decrease the observed line width and increases the signal-to-noise (S/N) ratio. The S/N-ratio can be defined as the ratio of the amplitude of the highest peak (="signal") divided by the standard deviation of the noise (="noise"). The noise level is the average value measured in a spectral window where no peak is anticipated. Typically about 5–50 cycles of the fundamental deformation frequency are acquired at a given strain amplitude, to achieve high S/N $\sim 10^5$. This leads to a number of acquired time data points N in the range of 1000–10,000. In most experiments, the time data $s(t)$ is not measured continuously but discretely after fixed time steps and is then digitized via a k-bit analog-to-digital converter (ADC) having 2^k discrete values for representing the measured signal. Typically a 100–200 kHz, 16-bit ADC prior to oversampling is used for FT-Rheology experiments (see also Section 2 for details of the "oversampling" technique).

A fast Fourier transformation (FFT) is a very common and particularly fast algorithm for discrete Fourier transformation (DFT) but is not suitable for FT-Rheology. While the more general discrete FT algorithm is formulated for an arbitrary numbers of points N, the simplest and most common FFT algorithms, e.g. the butterfly, require $N = 2^n$ data points. This restriction leads to fixed discrete values for the acquisition time t_{aq} and thus for the spectral resolution $\Delta\nu = 1/t_{aq}$. As a result, the fundamental frequency $\nu_1 = \omega_1/2\pi$ or the odd multiples at $(2k+1)\omega_1/2\pi$ are rarely located exclusively at a single data point having the precise frequency corresponding to integer multiples of the fundamental excitation within the FT-Rheology spectra. The application of a butterfly FFT can therefore introduce misleading results for the intensities and phases of the spectral intensities. For example the intensity of a higher harmonic cannot be read out at exactly the expected frequency value. A maximum error of up to a factor 2 might be introduced this way. More advanced FFT-algorithms exist that can provide an FT for arbitrary number of data points, and the most fundamental discrete Fourier transform (DFT) algorithms also allow for arbitrary data points. It is therefore important to report if the applied algorithm does simple zero-filling to generate artificially 2^n temporal data points prior to the transformation into frequency space.

The experimental setup for a high performance FT-Rheology experiment is based on the modification and extension of a commercial strain controlled rheometer (see Fig. 3). In these parallel configurations, the absolute values of the rheometer output signals must be calibrated with respect to the magnitude, phase, and frequency behavior and must also capture the non-linear contributions introduced by the instrument itself [33]. To avoid such calibration issues, the signal can be normalized to the fundamental frequency, which changes the absolute intensity (an extensive, additive quantity) to a relative intensity (an intensive, non-additive quantity). The relative intensity is much less vulnerable to non-systematic errors. The reproducibility has been tested [31] and reported to be typically in the range of 0.1% for the intensity of the higher harmonics relative to the intensity of the response at the fundamental frequency I_n/I_1. A crucial point is the accuracy of the torque transducer at higher frequencies. Torque transducers are typically specified up to 100 or 600 rad/s but it is often unknown if internal corrections are applied within this range. Calibration in the literature results in 80% efficiency of the torque transducer at 70 Hz excitation frequency [33]. In this work, an entire rheometer was calibrated with respect to the inherent non-linear contributions originating from the instrument itself. The applied torque, the excitation frequency and the strain amplitude were varied on a logarithmic scale and the non-linear contributions from the instrument itself ranged from 10^{-4} to 10^{-3} at maximum. Obviously the introduction of new instrumentation will further push these current hardware limits.

FT-Rheology allows for the averaging of multiple spectra to increase sensitivity, e.g. the magnitude spectra $I(\omega)$ are averaged so that the peaks are all positive and independent of the phase of the higher harmonics. The averaging of phase sensitive spectra needs either mechanical triggering or phase sensitive averaging. In general, spectral averaging increases the signal to noise (S/N) ratio of the acquired data proportional to the square root of the number of spectra captured, i.e. $S/N \propto \sqrt{n_{spectra}}$ provided systematic noise is of minor importance. When all precautions have been taken, S/N ratios up to 10^5 have been achieved for a single scan FT-Rheology experiment. A typical FT-Rheology spectrum is shown in Figs. 17 and 18 (nonlinear stress curve and FT-spectrum). With such a large signal to noise ratio, FT-Rheology can detect very low levels of nonlinearity in the FT spectrum. For example, from Fig. 18b, the time-dependent stress curve at an excitation frequency of $\omega_1 = 1$ rad/s and a strain amplitude of $\gamma_0 = 0.37$ appears as a single sinusoid. However, a substantial peak in the Fourier spectra at $3\omega_1$ can be quantified even at this small intensity ($I_3/I_1 < 10^{-2}$). Using a high performance ADC card [31], peaks can be quantified down to 10^{-4} relative intensity.

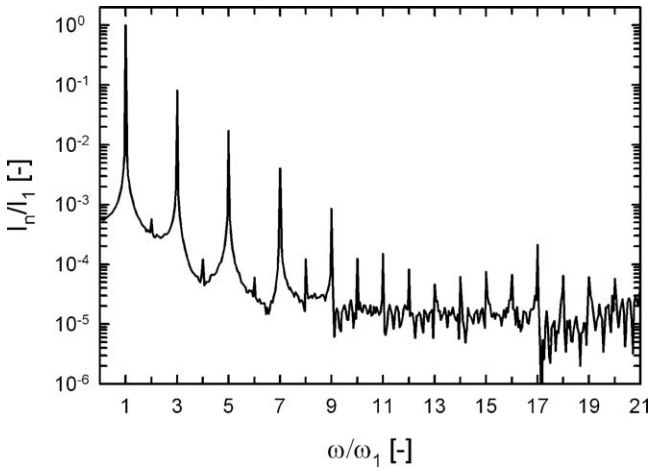

Fig. 17. FT-Rheology spectra of polyvinylalcohol (PVA) solution, at $T = 5\,^{\circ}C$, $\gamma_0 = 20$, frequency 1 Hz, where a S/N ratio of 100,000:1 could be achieved. Reproduced by permission of Wilhelm [33], copyright (2002) of WILEY-VCH.

High performance FT-rheology setups not only have a high sensitivity with respect to the *signal-to-noise ratio*, but can also quantify the system response up to very high multiples of the input signal. Currently spectra have been recorded spanning up to the 151st harmonic for an emulsion system (Fig. 19). Obviously such a large amount of higher harmonic contributions can lead to a rather complex interpretation. Fortunately, among the higher harmonics, the

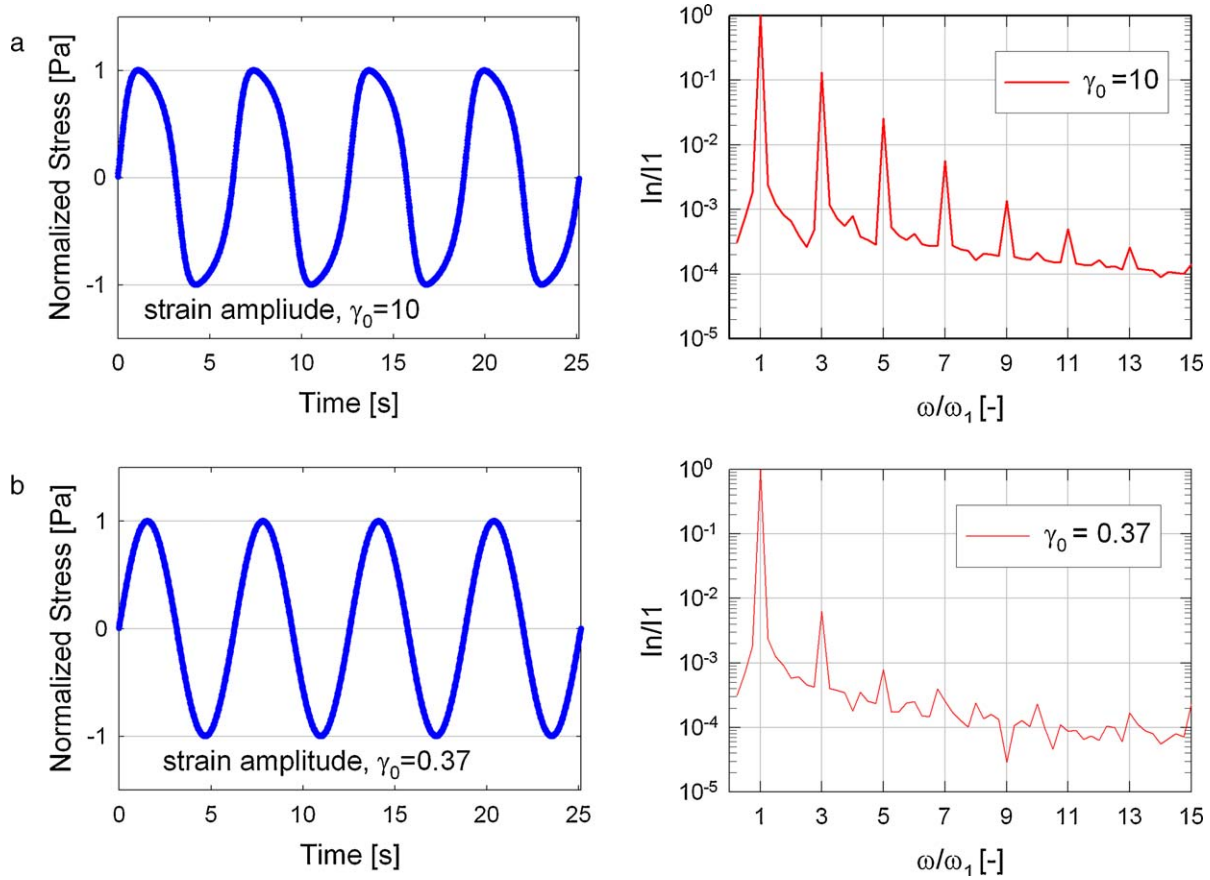

Fig. 18. The stress curve and FT spectrum of hyaluronic acid 1% aqueous solution at frequency, $\omega_1 = 1$ rad/s. (a) Normalized stress and FT spectrum at strain amplitude $\gamma_0 = 10$. A non-sinusoidal shape is observed, and the FT-method quantifies the extent of the nonlinear response via the magnitude (and phase) of the odd higher harmonics. (b) Normalized stress and FT spectrum at a strain amplitude $\gamma_0 = 0.37$, which corresponds to intermediate strain amplitude. To a naked eye, the time-dependent stress is similar to a perfect sinusoid. However, the presence of a 3rd harmonic is clearly shown by the Fourier spectra.

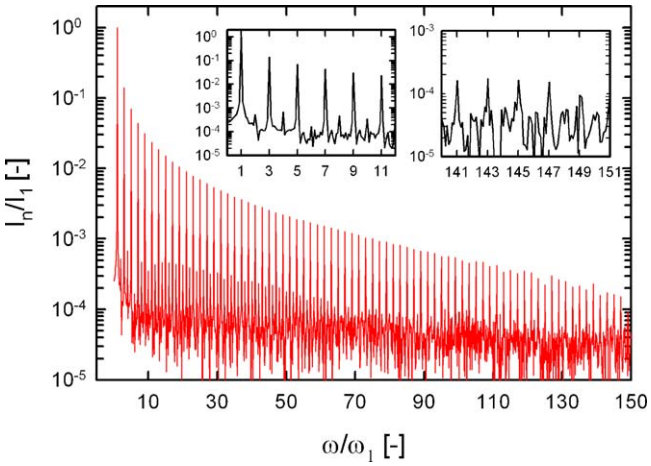

Fig. 19. FT-Rheology spectra at $\omega_1/2\pi = 0.1$ Hz and $\gamma_0 = 870$ of a water-in-oil emulsion. Mechanical overtones up to the 151st order could be detected.

relative intensity of the third harmonic ($I_{3/1} \equiv I(3\omega)/I(\omega)$, where ω is the excitation frequency) is generally the most intense.

4.1.1. New nonlinear quantitative coefficient, Q from FT-Rheology

If a strain sweep is performed at a fixed frequency, two main regimes can generally be observed. One is the linear regime at small amplitude (SAOS, small amplitude oscillatory shear) in which the rheological properties do not depend on the strain amplitude – at least not in an observable way. This is followed by a nonlinear regime in which viscoelastic properties depend systematically on the strain amplitude (LAOS, large amplitude oscillatory shear) (see also Fig. 1). Hyun et al. [42] subdivided the nonlinear region into two sub-regions, MAOS (medium amplitude oscillatory shear) and LAOS. MAOS is defined as an intermediate region (between SAOS and LAOS), where a particular scaling behavior is observed for the 3rd harmonic contribution. The strain amplitude for the MAOS regime typically ranges from $\gamma_0 \approx 0.1$ to $\gamma_0 \approx 1$ for most concentrated polymer solutions and polymer melts, although this range depends on the excitation frequency and material characteristics. In this intermediate region, $I_{3/1}$ is typically very low, around $3 \times 10^{-4} < I_{3/1} < 10^{-2}$, as compared to its magnitude in the LAOS region which may be as large as 10%.

Within the framework of *linear* viscoelasticity theory, $I_{3/1}$ asymptotically approaches zero because there is, by definition, no stress distortion. In the nonlinear regime, however, $I_{3/1}$ is finite and its intensity increases with strain amplitude. From the series expansions discussed in Section 3, the Fourier intensities of the nth harmonics grow with the corresponding *odd* powers of the strain amplitude ($I_n \propto \gamma_0^n, n = 1, 3, 5 \ldots$) in the small and intermediate strain amplitude range, e.g. Eq. (10) (note that each of *decomposed* sine and cosine components, G'_{nm} and G''_{nm}, also scale according to odd powers of the strain amplitude). Therefore, the total intensity of the third harmonic normalized by the first harmonic should be expected to initially scale quadratically with the strain amplitude ($I_{3/1} \equiv I_3/I_1 \propto \gamma_0^3/\gamma_0^1 = \gamma_0^2$). At small and medium strain amplitude, one may write this scaling relationship as a function of strain amplitude [41–43],

$$\log\left(\frac{I_3}{I_1}\right) = y_0 + s \log \gamma_0 \quad \text{or} \quad \frac{I_3}{I_1} = 10^{y_0}\gamma_0^s \tag{24}$$

Hyun et al. [42,43] reported the experimental value of $s = 2$, i.e. a quadratic scaling with strain amplitude γ_0 ($s = 2$ in Eq. (24)) for multiple polymer melts including linear polydisperse polypropylene (PP), monodisperse polystyrene (PS), and comb PS. This scaling was reported to be independent of molecular weight, molecular weight distribution (MWD) and imposed excitation frequency (see also Section 5.1). However, Hyun et al. [41,42] also reported that the polymers which show strain hardening behavior, e.g. branched PP, branched HDPE, PLA with epoxy chain extension agent, and LDPE exhibit a power-law scaling exponent $s < 2$. They suggested that this asymptotic log–log slope of $I_{3/1}(\gamma_0)$ is a good measure of the degree of strain hardening or long chain branching. Liu et al. [127] also reported that the log–log slope of $I_{3/1}(\gamma_0)$ for Polyolefin elastomer decreases from 2 with increased long chain branching (LCB) content.

The experimental results which give $s \neq 2$ contradict the simulation results of canonical constitutive models such as the Giesekus, exponential Phan-Thien Tanner (E-PTT), or pom-pom model, which produce $s = 2$. The mathematical power law expansion, Eq. (6), also predicts that the leading-order power-law scaling of $I_{3/1}(\gamma_0)$ is two, i.e. $s = 2$ in Eq. (24). Discrepancies between experimental results and theoretical asymptotic predictions are not unique to the scaling of $I_{3/1}(\gamma_0)$, and appear also for linear rheological properties. For example, in the linear viscoelastic regime it is well known that the storage modulus scales as $G'(\omega) \propto \omega^2$ in the terminal region for viscoelastic liquids. However, blockcopolymer systems show different terminal behavior $G'(\omega) \propto \omega^n$ depending on the microdomain shape, e.g. disordered structure ($n = 2$), lamellar structure ($n = 1/2$), cylinders ($n \approx 1/3$), and cubic ($n \approx 0$) [128]. As another example, for a PP/Clay nanocomposite it has been observed that the slope of $G'(\omega)$ at low frequency approaches zero with increased exfoliation of the clay layer [129]. We may therefore expect that some materials may not show the

simple theoretical prediction that $I_{3/1} \propto \gamma_0^2$. Nonetheless, most viscoelastic materials and constitutive models *do* show such asymptotic behavior with $s = 2$ in the medium amplitude oscillatory shear (MAOS) regime. As additional examples, we note that Sim et al. [91] also reported a quadratic power-law scaling of $I_{3/1}$ based on molecular dynamics-like simulations of ER fluids, and Yu et al. [130] and Liu et al. [127] reported the same behavior using the coupled double-convection-reptation with chain stretching (cDCR-CS) model.

In Fig. 20, we show the variation in $I_{3/1}$ as a function of strain amplitude for both simulations (Giesekus model and pom-pom model) and experimental observations (monodisperse linear PS). From the results, it may be deduced that a normalized third-harmonic nonlinearity can be defined which depends quadratically on strain amplitude even if there are some exceptional experimental results that need further investigation. Thus Hyun et al. [43] proposed a new nonlinear coefficient Q, defined as

$$Q \equiv \frac{I_{3/1}}{\gamma_0^2} \tag{25}$$

By convention, the absolute strain amplitude value is used in Eq. (25), not the % strain amplitude. This new nonlinear coefficient provides insight in how a material response develops and transitions from the linear to nonlinear regime. This new nonlinear material coefficient $Q(\omega, \gamma_0)$ characterizes FT-Rheology and will be a function of both strain amplitude (γ_0) and frequency (ω). However, just like other rheological properties such as viscosity ($\eta \equiv \sigma_{12}/\dot{\gamma}$), first normal stress coefficient ($\Psi_1 \equiv N_1/\dot{\gamma}^2$), and second normal stress coefficient ($\Psi_2 \equiv N_2/\dot{\gamma}^2$), these material coefficients are expected to approach constant values at low shear rates; these are commonly called the *zero-shear values*, for example η_0, $\Psi_{1,0}$, $\Psi_{2,0}$ [131]. We can similarly define the *nonlinear zero-strain value*, Q_0, as the asymptotic limiting constant value achieved at low strain amplitude,

$$Q_0(\omega) = \lim_{\gamma_0 \to 0} Q(\omega, \gamma_0) \tag{26}$$

Using this coefficient Q_0 we can quantify the intrinsic nonlinearity of complex fluids as a function of frequency. In Fig. 20, the coefficient Q is plotted as a function of strain amplitude for simulations (Giesekus and pom-pom model) and experimental results (monodisperse linear PS melt).

The underlying mathematics of oscillatory shear deformation is very similar to dielectric spectroscopy in which a sinusoidal electric field is applied and the resulting current is quantified with respect to the dielectric storage ε' and loss ε''. Increasing the magnitude of the electric field leads to detectable optical nonlinearities as quantified via hyperpolarizabilities, e.g. $\chi^{(2)}$ or $\chi^{(3)}$. The hyperpolarizablity is a material constant independent of the electric field. The rheological nonlinear coefficient Q is analogous to the nonlinear optical coefficient $\chi^{(3)}$ [71]. As is the case for the nonlinear optical coefficients, the Q coefficient does not vanish but rather approaches a constant value in the limit of zero strain amplitude. Consequently this material coefficient reflects the inherent and normalized leading-order nonlinear mechanical properties of the material under investigation.

The meaning of the nonlinear coefficient Q can be explored mathematically using the Fourier series, Eq. (8), and power series, Eq. (10), representations of the nonlinear stress response under LAOS flow. As a modification to Eq. (8), the shear stress under nonlinear oscillatory shear from FT-Rheology can be written as

$$\begin{aligned}\sigma(t) &= \sigma_1 \sin(\omega t + \delta_1) + \sigma_3 \sin(3\omega t + \delta_3) + \cdots \\ &= \sigma_1 \cos\delta_1 \sin\omega t + \sigma_1 \sin\delta_1 \cos\omega t \\ &\quad + \sigma_3 \cos\delta_3 \sin 3\omega t + \sigma_3 \sin\delta_3 \cos 3\omega t + \cdots\end{aligned} \tag{27}$$

From the above equation we can calculate the relative intensity of the third-harmonic from FT-Rheology as

$$I_{3/1} = \frac{I_3}{I_1} = \frac{\sigma_3}{\sigma_1} = \frac{\sqrt{(\sigma_3 \cos\delta_3)^2 + (\sigma_3 \sin\delta_3)^2}}{\sqrt{(\sigma_1 \cos\delta_1)^2 + (\sigma_1 \sin\delta_1)^2}} \tag{28}$$

For the power-law representation of the shear stress waveform, we refer to Eq. (10) (see also Pearson and Rochefort [20]),

$$\begin{aligned}&\text{1st nonlinear term} = [G'_{11}\gamma_0 + G'_{31}\gamma_0^3 + O(\gamma_0^5) + \cdots] \\ &\sin\omega t + [G''_{11}\gamma_0 + G''_{31}\gamma_0^3 + O(\gamma_0^5) + \cdots]\cos\omega t\end{aligned} \tag{29}$$

$$\begin{aligned}&\text{3rd nonlinear term} = [G'_{33}\gamma_0^3 + G'_{53}\gamma_0^5 + O(\gamma_0^7) + \cdots] \\ &\sin 3\omega t + [G''_{33}\gamma_0^3 + G''_{53}\gamma_0^5 + O(\gamma_0^7) + \cdots]\cos 3\omega t\end{aligned} \tag{30}$$

These two distinct representations, i.e. Fourier series from Eq. (8) and power series from Eq. (10), describe the same nonlinear phenomena, therefore we can obtain the Q coefficient by inserting Eq. (29) and (30) into (28),

$$\begin{aligned}\frac{I_3}{I_1} &= \frac{\sqrt{(G'_{33}\gamma_0^3 + G'_{53}\gamma_0^5 + \cdots)^2 + (G''_{33}\gamma_0^3 + G''_{53}\gamma_0^5 + \cdots)^2}}{\sqrt{(G'_{11}\gamma_0 + G'_{31}\gamma_0^3 + \cdots)^2 + (G''_{11}\gamma_0 + G''_{31}\gamma_0^3 + \cdots)^2}} \\ &= \frac{\sqrt{G'^2_{33}\gamma_0^6 + G''^2_{33}\gamma_0^6 + O(\gamma_0^8)\cdots}}{\sqrt{G'^2_{11}\gamma_0^2 + G''^2_{11}\gamma_0^2 + O(\gamma_0^4)\cdots}} \\ &= \frac{\sqrt{G'^2_{33} + G''^2_{33} + O(\gamma_0^2)\cdots}}{\sqrt{G'^2_{11} + G''^2_{11} + O(\gamma_0^2)\cdots}} \times \frac{\gamma_0^3}{\gamma_0} = Q(\omega, \gamma_0)\cdot\gamma_0^2\end{aligned} \tag{31}$$

In the limit of the small-strain amplitudes we thus obtain the zero-strain nonlinearity, $Q_0(\omega)$

$$\begin{aligned}Q_0(\omega) &= \lim_{\gamma_0 \to 0} Q(\omega, \gamma_0) = \lim_{\gamma_0 \to 0} \frac{\sqrt{G'^2_{33} + G''^2_{33} + O(\gamma_0^2)\cdots}}{\sqrt{G'^2_{11} + G''^2_{11} + O(\gamma_0^2)\cdots}} \\ &= \frac{\sqrt{G'^2_{33}(\omega) + G''^2_{33}(\omega)}}{\sqrt{G'^2_{11}(\omega) + G''^2_{11}(\omega)}} = \frac{|G^*_{33}(\omega)|}{|G^*_{11}(\omega)|}\end{aligned} \tag{32}$$

From Eq. (32), it can be seen that $Q_0(\omega)$ is the normalized 3rd nonlinear complex modulus (3rd nonlinear

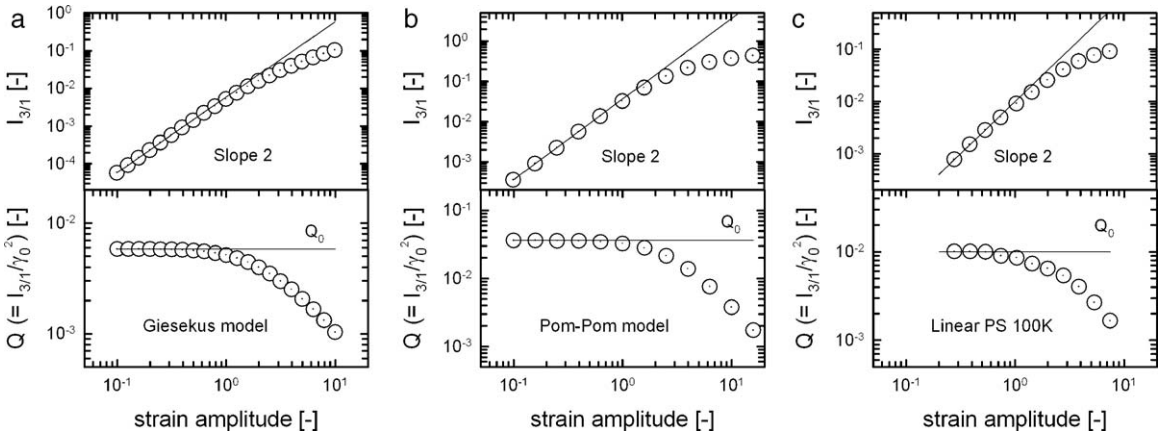

Fig. 20. $I_{3/1}$ and Q as a function of strain amplitude from medium strain amplitude ($\gamma_0 \approx 0.1$) to large strain amplitude ($\gamma_0 \approx 10$). (a) Giesekus model with $G = 1$, $\lambda = 1$, $\alpha = 0.3$, $\omega/2\pi = 1$ Hz, (b) integral pom-pom model with $q = 5$, $s_a = 6$ and $s_b = 20$, $\omega/2\pi = 0.1$ Hz, and (c) monodisperse linear PS (PS 100K) at $\omega = 4.25$ rad/s, $T = 160\,^\circ$C.

term) divided by the linear complex modulus (1st nonlinear term). The magnitude of this intrinsic nonlinearity can be evaluated for any complex fluid, as with any other rheological properties; for example, Hyun et al. [43] have used the strain and frequency dependence of the Q coefficient, $Q_0(\omega)$ and $Q(\gamma_0)$, to distinguish linear PS and comb PS (see Section 5.1). Further investigations are suggested to more fully explore the scaling behavior of $I_{3/1}$ as a function of strain amplitude for various complex fluids.

4.1.2. Transition between linear and nonlinear viscoelasticity

The higher-harmonic contributions in LAOS emerge according to the quadratic scaling behavior discussed in the previous section, but eventually deviate from this leading order dependence. As the strain amplitude (γ_0) increases, the variation in the higher harmonics, e.g. $I_{3/1}(\gamma_0)$ is often observed to be a sigmoidal function and can empirically be described via [33]

$$I_{3/1}(\gamma_0) = A\left(1 - \frac{1}{1 + B\gamma_0^C}\right) \tag{33}$$

In this equation, the parameter A reflects the maximum intensity of $I_{3/1}$ at high strain amplitudes (and is often $A = 0.2$–0.3), B is approximately the point of inflection and the parameter C reflects the scaling exponent (e.g. $C = 2$ from Section 4.1.1). The sigmoidal behavior of $I_{3/1}$ is reminiscent of the empirical equations often used to describe shear-rate dependent viscosity, which also show asymptotic limits at low and high shear-rates, e.g. the Carreau-Yasuda or the Cross models [1,2,132]. The parameters used in these empirical equations reflect the underlying physics, including asymptotes at low and high deformations and the pivot point where nonlinearities appear. Non-sigmoidal behavior has also been observed for $I_{3/1}(\gamma_0)$. For example, with dispersed systems the sigmoidal behavior of $I_{3/1}$ has shown a "bump" or "overshoot" at intermediate strain amplitude due to the disperse phase [59]. This non-sigmoidal behavior is obtained for systems in which strong interactions occur between a viscoelastic matrix and a dispersed phase, e.g. the major volume phase and carbon black. Nonlinearity therefore reflects the superposition of two responses: one qualitatively common to all "pure" (unfilled) polymers and another related to the "filler" response [60]. Leblanc suggested a simple five parameter equation for the behavior of such highly filled rubber systems [59] (original equation is modified by this review format; see also Section 5 for more detail),

$$I_{n/1}(\gamma_0) = (I_{n/1,m} + \alpha\gamma_0) \times \{[1 - \exp(-\alpha\gamma_0)]^{I_{n/1,m}} + B(C\gamma_0)^{D-1}\exp[-(C\gamma_0)^D]\} \tag{34}$$

The above equation consists of three members: one describing the asymptotic high strain behavior

$$(I_{n/1,m} + \alpha\gamma_0) \tag{35}$$

one describing the matrix response, the so-called polymer component

$$(I_{n/1,m} + \alpha\gamma_0) \times [1 - \exp(-\alpha\gamma_0)]^{I_{n/1,m}} \tag{36}$$

and one describing the filler response, the so-called filler component

$$(I_{n/1,m} + \alpha\gamma_0) \times B(C\gamma_0)^{D-1}\exp[-(C\gamma_0)^D] \tag{37}$$

At low strain amplitude, the nonlinearity is essentially controlled by the filler component (dispersed phase) and at higher strain amplitude the influence of the filler vanishes and the nonlinearity is controlled by the continuous phase of the polymer component [59].

Any suitable functional form of $I_{3/1}(\gamma_0)$, whether sigmoidal or non-monotonic, must be continuous and differentiable. These functions describe an asymptotic transition from the linear (SAOS) to the non-linear regimes (MAOS and LAOS) and the deviation from the limiting value is a measure of the limit of the linear response. This result is striking, since it suggests that any improvement in instrumentation could affect the apparent limit of the linear regime for a specific sample. Within the concept of the Q coefficient and the high sensitivity of FT-Rheology a linear regime is only the asymptotic approximation for vanishing nonlinearities. Having e.g. $Q_0 = 0.01$ and a strain

amplitude of $\gamma_0 = 0.01$ the expected non-linearity of the third-harmonic is $I_{3/1} = 10^{-6}$. This value is outside the detection range of any current commercial rheometer, but is evidently nonzero.

This whole argument is recognition that the linear response is only achieved for vanishing deformations, and therefore never precisely achieved in any real experiment. Nevertheless it is commonly accepted that the linear response can accurately describe the limiting mechanical response. An alternate definition of the linear viscoelastic regime in oscillatory shear might be the regime in which the experimental response obeys the leading-order nonlinear scaling and can be extrapolated to the limit of zero strain amplitude. Additionally, one may define a criteria that the nonlinearity in the signal response must be smaller than a critical threshold, e.g. $I_{3/1} < 0.5\%\,(\sim 5 \times 10^{-3})$ as determined from FT-Rheology, in which case the linear response (i.e. the moduli G' or G'', or the intensity I_1) would describe the overall response by 99.5%. This new definition of the linear regime under oscillatory conditions may be helpful in the unambiguous determination of the limit of a linear response in a clear and reproducible way that is independent of the instrumentation.

4.1.3. Even harmonics of the normal stress differences

In the nonlinear regime, the normal stress differences can also show higher harmonic contributions (cf. Section 3.4). FT-Rheology can also quantify the even higher harmonic intensities ($N_{1,0}$, $N_{1,2}$, $N_{1,4}$, ...) and phase angles ($\delta_{1,2}$, $\delta_{1,4}$, ...) from the time-dependent first normal stress difference, Eq. (22). To illustrate this, in Fig. 21 we plot the FT intensity spectrum of the normal stress difference (in which even higher harmonics dominate) measured experimentally for an entangled polymer solution and a multimode Giesekus model simulation [124,125]. The higher order even harmonics grow with an even power of the strain amplitude ($I_n (= N_{1,2n}) \propto \gamma_0^n, \quad n = 2, 4, 6 \ldots, I_0$ is the non-zero mean or average normal stress) in the small and intermediate strain amplitude range. It is difficult to experimentally observe that the nth harmonics grow with an *even* power of strain amplitude due to technical limitations (small rectangular box in Fig. 21b). From the multi mode Giesekus model, however, this terminal scaling can be directly observed (Fig. 21b). It can be observed that the intensity of the 4th harmonic normalized by the 2nd harmonic of first normal stress difference scales quadratically with the strain amplitude ($N_{1,4}/N_{1,2} \equiv I_4/I_2 \propto \gamma_0^4/\gamma_0^2 = \gamma_0^2$), in the same way that the shear stress varied (i.e. $\sigma_3/\sigma_1 \equiv I_3/I_1 \propto \gamma_0^3/\gamma_0^1 = \gamma_0^2$) in the region we have defined as medium amplitude oscillatory shear (MAOS). We can therefore define once again a nonlinear normal stress coefficient ($\equiv I_{4/2}/\gamma_0^2$), e.g. like Q coefficient ($\equiv I_{3/1}/\gamma_0^2$) for shear stress using the quadratic strain amplitude scaling of the normalized harmonic intensity.

4.1.4. Even harmonics within the shear stress

As discussed in Section 3.1, only odd harmonics of shear stress are expected for typical and idealized material responses to LAOS. However, even harmonics can be observed experimentally, e.g. Figs. 17, 18a, 19 show small peaks in the even higher harmonics of the Fourier transformed shear stress. These even harmonics are relatively small compared with the odd higher harmonics. Similarly, in Fig. 21a, we can also observe peaks at odd higher harmonics in the first normal stress difference. The occurrence of even higher harmonics within the shear stress (or odd higher harmonics of normal stress difference) in the response signal is often considered as an experimental artifact and the peaks are neglected [14].

However, even harmonics can be reproducibly generated and quantified using the FT-Rheology technique [5]. Wall slip is expected to be one of the main reasons for the occurrence of even harmonic contributions [22,133]. Graham [74] demonstrated the occurrence and growth of even harmonics in a dynamic wall slip model. This leads to a break in the symmetry of the shear flow, and the material response no longer meets the symmetry of the measuring geometry. These calculations support the experimental investigations of Adrian and Giacomin [23]. Yoshimura and Prud'homme [134] used a simple slip model at the bounding surface and demonstrated that, in general, slip at the bounding surfaces does not produce even harmonics. Atalık and Keunings [77] have also shown that wall slip is not a necessary condition for the occurrence of even harmonics using the Giesekus model (see Appendix C) with no-slip boundary conditions. They concluded that a combination of elasticity (i.e. a finite Weissenberg number = $\lambda\gamma_0\omega$, where λ is the relaxation time, γ_0 is the strain amplitude, ω is angular frequency) and shear thinning yields transient even harmonics in shear stress. The life span and intensity of these even harmonics were considerably extended by inertia. Wilhelm et al. [30] have also explained the appearance of even harmonics arising from a time-dependent memory effect or a nonlinear elastic contribution in the system. These results are in contrast with the results of Yosick et al. [135]. Yosick et al. [135] reported that inertia does not create even harmonics using the upper convected Maxwell (UCM) model supplemented with a kinetic rate equation. Mas and Magnin [136] have argued that a finite yield stress can also be a reason for the occurrence of even harmonics. Yu et al. [130] report that the yield stress is not a sufficient condition to cause even harmonics from the Bingham model even though they observed some even harmonic contributions at the lower limits of their experimental resolution.

In contrast with the above macroscopic points of view, Sagis et al. [137] explained the possibility of even harmonics from a microscopic point of view. They incorporated an orientation tensor which represents an anisotropic internal microstructure with constitutive equations for an elastic material containing anisotropic rigid particles. They also predicted that the intensity of the even harmonics first increases to a maximum as strain amplitude increases, beyond which the intensity decreases continuously with strain amplitude. Their experimental data for a 4 wt% Xanthan gel also showed significant even harmonic contributions with similar trends as strain amplitude increased. The authors concluded that the even harmonics in the stress response arise as a consequence of changes in the structure of the material arising from shear-induced alignment of the anisotropic colloidal par-

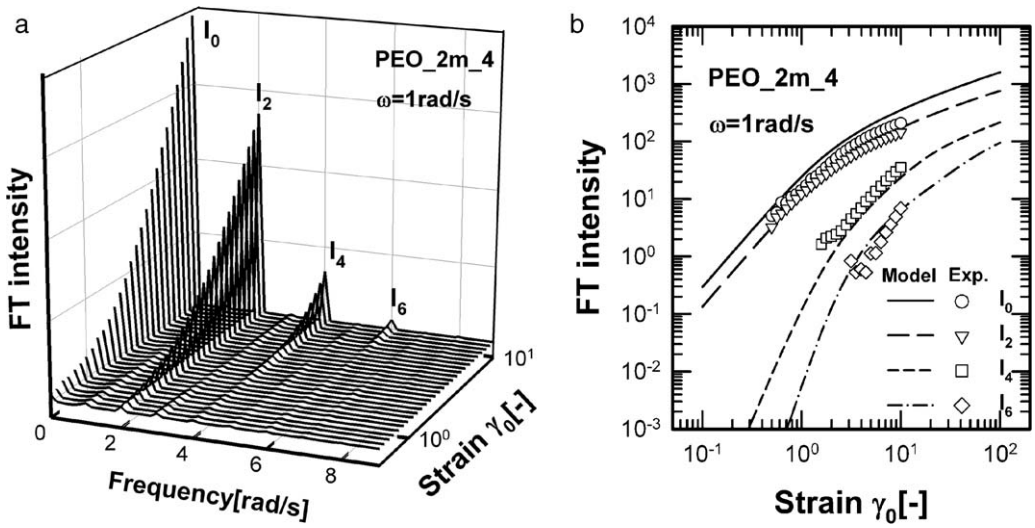

Fig. 21. (a) 3D plot for the FT of the oscillating first normal stress difference for a 4 wt% PEO solution with a molecular weight 2×10^6 g/mol. There are trace contributions from the odd harmonics for the entire range of strain amplitudes tested. (This non-idealized behavior is similar to the even harmonics present in the nonlinear shear stress.) (b) FT intensity as a function of strain amplitude. The experimental data are compared with simulations using a multi-mode Giesekus model [124]. Experimental measurements of the higher harmonic intensities (I_4, I_6) have severe errors at low strain amplitude.

ticles in the system. Sim et al. [91] also investigated the appearance of even harmonics of electrorheological fluids (ER fluids) using numerical simulation. Sim et al. [91] concluded that the appearance of even harmonics arose from the abrupt release of shear stress during the structural reformation process of the anisotropic microstructure in an ER fluid. Carotenuto et al. [46] report even harmonics which appeared to be material independent for an immiscible polymer blend system. They investigated the second harmonic for different samples (pure PIB, pure PDMS, PDMS/PIB-1/9) at different temperatures and geometries (cone and plate and plate and plate). They concluded that the second harmonics they observed could be attributed to imperfect alignment of the upper and lower plates of the rheometer. As we have noted above, it is difficult to accurately measure the relatively small even harmonic contributions compared with the high intensity odd harmonic contributions to the shear stress. For completeness, we note that the Fourier spectrum of strain (for a strain-controlled test) should not show higher harmonic contributions. However, there are always technical limits to producing perfect sinusoidal signals [57]. These defects which come from non-sinusoidal strain can affect the stress curve itself [95]. Therefore, imperfect excitation can also create even higher harmonics.

As of this writing, we conclude that analysis of even harmonics in the shear stress can give some additional information for microstructured materials (e.g. orientation) but care must be taken to avoid systematic experimental artifacts (e.g. fluid inertia, imperfect excitation, or misalignment). However the origin of even harmonics may not always be clear, therefore additional investigation is needed before a definitive conclusion can be reached. Similar comments apply to reports of odd harmonics in the first normal stress difference. In Table 1 we summarize the current understanding of the presence of even harmonics in the shear stress.

4.2. Characteristic functions

A simple physical interpretation of the oscillatory stress waveforms in terms of the Fourier amplitudes and phases is not always possible. In this section we review an interpretive method which considers the whole frequency spectrum as a superposition of different overtone sub spectra that characterize different non-linear rheological effects. For simplicity, four canonical rheological effects are considered: a base linear viscoelastic response, strain hardening, strain softening, and stick-slip (e.g. asymmetric shear-banding or wall slip). The waveforms which correspond to these known rheological phenomena are referred to as *characteristic functions* [5]. These four characteristic waveforms, and the associated Fourier spectra, are shown in Fig. 22. The total stress response can then quantitatively be described by a superposition of these characteristic functions.

The relative contributions are based on the magnitude of the normalized higher harmonics (I_n/I_1) and the determination of the corresponding phases δ_n of the higher harmonics. The measured signal can be fitted in the time domain or the frequency domain with the four characteristic contributions (Fig. 22 on the top). Specifically, these characteristic contributions are a sinusoidal function describing the linear response, a rectangular function describing strain softening, a triangular function describing strain hardening, and finally a saw tooth function describing shear bands or wall slip (see Eqs. (38)–(41) below). This final characteristic function is the only one that can represent the even harmonics contributions within stress described in the previous section. The strain softening contribution (a square wave) and the strain hardening contribution (a triangular wave) only have peaks at odd higher harmonics of the excitation frequency. One main distinction between the square and triangle functions is the rate of decay in the intensity of the higher harmonics. In the

Table 1
The summary of research regarding the appearance of even harmonics in shear.

The origin of even harmonics		Reference	Comment
Even harmonics are within the range of experimental error		• Onogi et al. [14] -Carbon black dispersed in PS solution	• Even harmonics are negligibly small
		• Carotenuto et al. [46] -Immiscible polymer blends	• Even harmonic is attributed to an imperfect alignment of geometry
Macroscopic view	Wall slip	• Yoshimura and Prud'homme [134] • Hatzikiriakos and Dealy [22,133] • Graham [74] -Simulation with dynamic wall slip model (memory slip)	• Wall slip is not a sufficient condition
	Inertia	• Yosick et al. [135] -Simulation with the UCM model supplemented with a kinetic rate equation	• Fluid inertia produces no even harmonics
		• Atalık and Keunings [77] -Simulation with Giesekus model with no-slip boundary condition and Johnson-Segalman models	• The combined effects of inertia, elasticity, and shear thinning. Inertia increases even harmonics
	Yield stress	• Mas and Magnin [136]	• Yield stress fluid
		• Yu et al. [130] -Simulation with Bingham model	• Yield stress is not a sufficient condition
Microscopic view	Anisotropic microstructure - the change of microstructure	• Sagis et al. [137] -Simulation with constitutive equation for an elastic material with anisotropic rigid particle and experimental results of Xanthan gel	• The even harmonics are the result of a change in the structure of the material
		• Sim et al. [91] -Simulation of ER materials	• The abrupt change of shear stress during reformation process

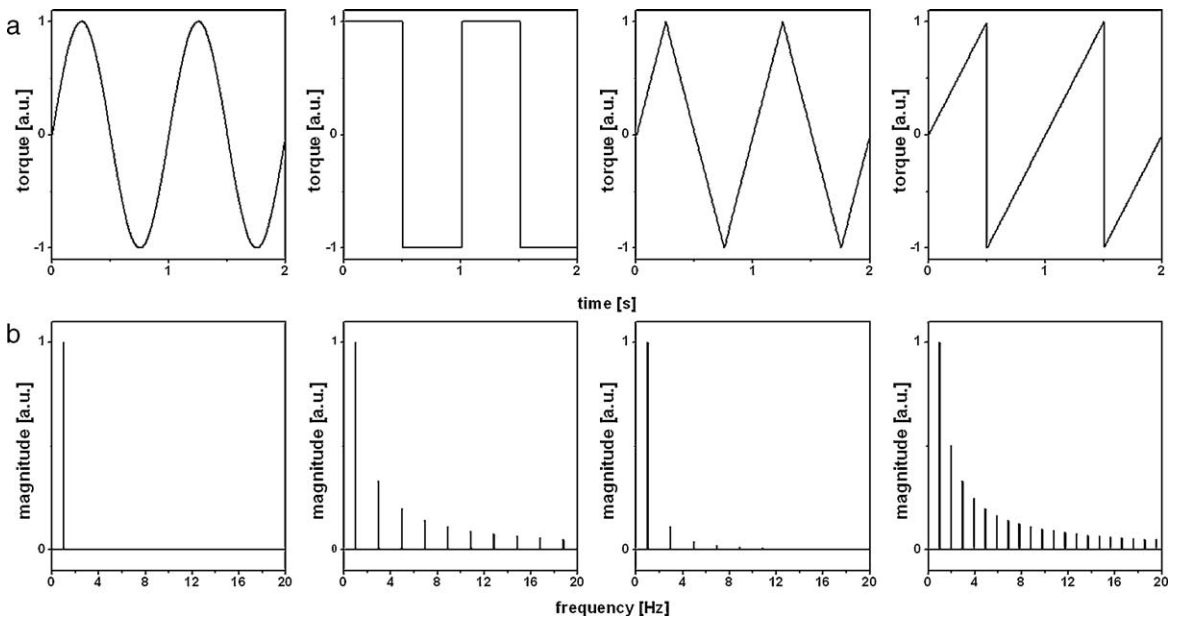

Fig. 22. The four characteristic functions (from left to right): a sine, a rectangular, a triangular and a saw tooth shaped wave, representing viscoelastic, strain softening, strain hardening, and shear bands. The time domain data is displayed on the top (a) and the corresponding FT magnitude spectra in the bottom (b). Reproduced by permission of Klein et al. [5], copyright (2007) of American Chemical Society.

case of strain softening (rectangular wave) the intensities of the higher harmonics decay as $1/n$ ($n = 1, 3, 5, \ldots$), and in the case of strain hardening (triangle wave) they decay as $1/n^2$ ($n = 1, 3, 5, \ldots$). In addition to the scaling in the rate of decay, the phase of the higher harmonics is also different. For the rectangular function the phases of the higher harmonic contributions are the same (for $\delta_r = 0$), for the triangular function they alternate between 0 and π (for $\delta_l = 0$). The fourth characteristic function captures the influence of shear bands or wall slip contributions. Peaks are present at all multiples of the excitation frequency and the intensity decreases progressively by a factor of $1/n$ ($n = 1, 2, 3, \ldots$).

The linear response function is given by:

$$\sigma_l(t) = A_l \sin(\omega_1 t + \delta_l) \tag{38}$$

The periodic rectangular function is given by:

$$\sigma_r(t) = A_r \frac{4}{\pi}\left(\sin(\omega_1 t + \delta_r) + \frac{\sin 3(\omega_1 t + \delta_r)}{3} + \frac{\sin 5(\omega_1 t + \delta_r)}{5} + \cdots\right) \tag{39}$$

The periodic triangular function is given by:

$$\sigma_t(t) = A_t \frac{4}{\pi}\left(\sin(\omega_1 t + \delta_t) - \frac{\sin 3(\omega_1 t + \delta_t)}{3^2} + \frac{\sin 5(\omega_1 t + \delta_t)}{5^2} - \cdots\right) \tag{40}$$

The periodic saw tooth is given by:

$$\sigma_{st}(t) = A_{st} 2\left(\sin(\omega_1 t + \delta_{st}) - \frac{\sin 2(\omega_1 t + \delta_{st})}{2} + \frac{\sin 3(\omega_1 t + \delta_t)}{3} - \cdots\right) \tag{41}$$

The superimposed total signal is given by:

$$\sigma(t) = \sigma_l(t) + \sigma_r(t) + \sigma_t(t) + \sigma_{st}(t) \tag{42}$$

By superimposing these different contributions in Eq. (42), the measured time domain signal of the torque response can be reconstructed. Both the reconstructed time data and the corresponding FT representation of the experimental signal are used to determine the different contributions of strain softening and hardening. This novel analysis, based on FT-Rheology experiments, gives easy access to the quantification of the non-linear mechanical regime with respect to strain hardening, softening and shear bands.

4.3. Stress decomposition

The viscoelastic stress measured in oscillatory shear flow can readily be decomposed into elastic and viscous parts in the linear regime (i.e. SAOS), however, it is not easy to unambiguously decompose the stress in the non-linear regime (i.e. LAOS). FT-Rheology does not decompose the nonlinear shear stress in terms of the deformation inputs themselves, but rather operates on the time-domain representation of the stress waveform, $\sigma(t)$, and quantifies nonlinear viscoelastic responses through intensity and phase angle of higher harmonics. The higher harmonics from FT-Rheology are used individually to interpret nonlinear behavior, especially the third harmonic contribution ($I_{3/1}$ or Q coefficient). The characteristic functions introduced in the previous section may be thought of as a set of "basis functions" used to represent a superposition of different physical phenomena, however in contrast to the harmonic series considered from FT-Rheology [69], they are not mutually orthogonal (in a mathematical sense) nor is the set of functions a unique basis.

Cho et al. [66] used symmetry arguments to propose a method of decomposing the total stress in non-linear measurements into a superposition of elastic stress $\sigma'(\gamma)$ (a single-valued function of strain) and viscous stress $\sigma''(\dot{\gamma})$ (a single-valued function of strain-rate). This is related to Eq. (4) and the corresponding discussion in Section 3, in which the nonlinear shear stress is expanded by a polynomial or Taylor expansion as a function of the strain and strain-rate with the assumption that shear stress must be a function of the direction of shearing. Eq. (4) can be reformulated as

$$\sigma(x, y) = \sum_{i=1}\sum_{j=1}[C_{2i-1,2(j-1)}x^{2i-1}y^{2(j-1)} + D_{2(i-1),2j-1}x^{2(i-1)}y^{2j-1}] \tag{43}$$

where $x \equiv \gamma = \gamma_0 \sin\omega t$ and $y \equiv \dot{\gamma}/\omega = \gamma_0 \cos\omega t$.

From Eq. (43), the relationship $\sigma(x, -y) = -\sigma(-x, y)$ can be also confirmed. With this symmetry, shear stress can be decomposed as follows:

$$\sigma(x, y) = \frac{\sigma(x, y) + \sigma(x, -y)}{2} + \frac{\sigma(x, y) + \sigma(-x, y)}{2} = \sigma_{OE}(x, y) + \sigma_{EO}(x, y) \tag{44}$$

In Eq. (44), the first and the second subscript denote the parities of x and y, respectively. Hence $\sigma_{OE}(x, y)$ is an odd function (O) for x and even (E) for y and $\sigma_{EO}(x, y)$ is an even function for x and odd for y. From Eq. (43), we can calculate σ_{OE} and σ_{EO} as follows:

$$\sigma_{OE}(x, y) = \sum_{i=1}\sum_{j=1}C_{2i-1,2(j-1)}x^{2i-1}y^{2(j-1)},$$

$$\sigma_{EO}(x, y) = \sum_{i=1}\sum_{j=1}D_{2(i-1),2j-1}x^{2(i-1)}y^{2j-1} \tag{45}$$

Since the stress σ_{OE} exhibits odd symmetry with respect to x and even symmetry with respect to y, whereas σ_{EO} exhibits even symmetry with respect to x and odd symmetry with respect to y, it is clear that over one cycle we have:

$$\oint \sigma_{OE}\, dx = 0, \quad \oint \sigma_{EO}\, dy = 0 \tag{46}$$

Plots of σ_{OE} vs. x and σ_{EO} vs. y therefore do not enclose any area in contrast to plots of σ vs. x or σ vs. y. This implies that σ_{OE} is only a function of x (strain) and σ_{EO} is only a function of y (strain-rate), therefore σ_{OE} and σ_{EO} can be referred to as the elastic stress $\sigma'(x)$ and viscous stress $\sigma''(y)$, respectively. Using the relation $x^2 + y^2 = \gamma_0^2$ in Eq. (45), it can be

confirmed that the elastic stress σ' is an odd function of x (strain) and the viscous stress σ'' is an odd function of y (strain-rate). The functional form of each stress contribution depends on the oscillatory inputs of strain amplitude γ_0 and frequency ω,

$$\sigma' = \sigma'(x; \gamma_0, \omega), \quad \sigma'' = \sigma''(y; \gamma_0, \omega) \tag{47}$$

In Fig. 23, decomposition of the total shear stress into σ' and σ'' are plotted for a polypropylene melt at 170 °C and 1 rad/s. These elastic and viscous stresses are also related directly to the Power series as follows:

$$\sigma' = \sum_{k=0}^{\infty} g'_{2k+1}(\omega, \gamma_0)x^{2k+1}, \quad \sigma'' = \sum_{k=0}^{\infty} g''_{2k+1}(\omega, \gamma_0)y^{2k+1} \tag{48}$$

The work W_E done by the elastic stress is stored in the system and completely released during a cyclic deformation. In oscillatory shear flow, if σ' is truly an elastic stress then the following equation should be satisfied:

$$W_E \equiv \int_{t=0}^{t=2\pi/\omega} \sigma' \, dx = 0 \tag{49}$$

Eq. (49) is easily proved because from Eq. (48) we have

$$W_E = \int_{t=0}^{t=2\pi/\omega} \sum_{k=0}^{\infty} g'_{2k+1}(\omega, \gamma_0)x^{2k+1} \, dx = \left[\sum_{k=0}^{\infty} \frac{g'_{2k+1}}{2k+2} x^{2k+2} \right]_{t=0}^{t=2\pi/\omega}$$
$$= \left[\sum_{k=0}^{\infty} \frac{g'_{2k+1}}{2k+2} \gamma_0^{2k+2} \sin^{2k+2} \omega t \right]_{t=0}^{t=2\pi/\omega} = 0 \tag{50}$$

It should be noted that $g'_1(\omega, \gamma_0)$ and $g''_1(\omega, \gamma_0)$ are not, strictly speaking, storage and loss moduli associated with nonlinear viscoelasticity, although they do reduce to the familiar linear viscoelastic moduli in the limit $\gamma_0 \to 0$. This is because the polynomial expansions in Eq. (48) are not orthogonal. The principal achievement of stress decomposition (SD) is to decompose the nonlinear viscoelastic stress measured in LAOS tests into physically meaningful elastic and viscous components. This alternate representation is achieved by considering the stress to be a function of the independent deformation inputs of strain and strain-rate, i.e. $\sigma(\gamma, \dot{\gamma})$, rather than the initial time-domain representation $\sigma(t)$.

This original stress decomposition approach suffers from non-orthogonality of polynomial regression fitting to calculate nonlinear coefficients in Eq. (48). What is preferable is to use an orthogonal polynomial basis such as the Legendre or the Chebyshev polynomials. Use of Chebyshev polynomials of the first kind seems to be the best and this approach is discussed in more detail in Section 4.4. When applying the stress decomposition approach to measurements of the first normal stress difference, difficulties are encountered both in the experimental measurement and in the theoretical analysis. It is currently not clear whether normal stress differences can usefully be decomposed into elastic and viscous parts.

4.4. Chebyshev polynomial representation

Although the decomposition of the nonlinear stress response can be carried out for any complex material, the challenge is to obtain a physical understanding of the higher harmonic components of the stress response. It has recently been demonstrated that a direct physical interpretation can be obtained by representing the individual curves of the decomposed elastic stress σ' and viscous stress σ'' (introduced in Section 4.3, see Fig. 24) with an orthogonal set of polynomial functions, such as the Chebyshev polynomials of the first kind [69,138]. These polynomials represent a set of basis functions that can describe the measured material stress in the orthogonal space formed from the oscillating strain and strain-rate. This simplifies the description of the material response because it is no longer necessary to consider the explicit (and superfluous) temporal dependence in the stress, and instead focus on how the material response varies with magnitude and rate of deformation.

The decomposed stress curves inherently have odd symmetry with respect to either γ or $\dot{\gamma} = 0$. The first few Chebyshev functions with odd symmetry are $T_1(x) = x$, $T_3(x) = 4x^3 - 3x$, and $T_5(x) = 16x^5 - 20x^3 + 5x$. A series of Chebyshev functions, with corresponding weighting coefficients, is then used to represent the elastic and viscous stresses according to

$$\sigma'(\bar{x}) = \gamma_0 \sum_{n=odd} e_n(\omega, \gamma_0)T_n(\bar{x})$$
$$\sigma''(\bar{y}) = \dot{\gamma}_0 \sum_{n=odd} v_n(\omega, \gamma_0)T_n(\bar{y}) \tag{51}$$

where $\bar{x} = x/\gamma_0 = \gamma/\gamma_0$ and $\bar{y} = y/\gamma_0 = \dot{\gamma}/\dot{\gamma}_0$ represent the instantaneous strain and rate of strain suitably normalized with the magnitude of the input values ($x \equiv \gamma_0 \sin \omega t$ and $y \equiv \gamma_0 \cos \omega t = \dot{\gamma}/\omega$ are defined in Eq. (43), Section 4.3). The Chebyshev weighting coefficients $e_n(\omega, \gamma_0)$ and $v_n(\omega, \gamma_0)$, i.e. italic English letters 'e' and 'v', respectively describe the elastic and viscous contributions and have units of modulus and viscosity. The use of an orthogonal polynomial series may be contrasted with the alternate option of using a polynomial series of arbitrary order, e.g. $\sigma'(\gamma) = a_1 + a_3\gamma^3 + a_5\gamma^5 + \cdots + a_m\gamma^m$, in which the coefficients a_m are fit by the method of least squares [66,139]. Such regressions result in coefficient values a_m which depend on the highest order of the polynomial used for the fit, in contrast to the use of orthogonality relations that enable unique determination of the Chebyshev coefficients e_n and v_n [68]. It is important that coefficients at each order n can be determined independently of the highest harmonic of interest because improvements in the signal/noise ratios of LAOS measurement techniques continue to reveal the presence of ever-higher harmonics, e.g. harmonics as high as $n = 151$ (see Fig. 20) can now be observed. The Chebyshev polynomials also represent a near-optimal basis set for capturing the variation in continuous functions such as $\sigma'(\gamma)$, $\sigma''(\dot{\gamma})$, and thus enable interpolation of material properties to arbitrary intermediate strains.

The third-order coefficients determine the concavity of each curve (to leading order), and it is this curva-

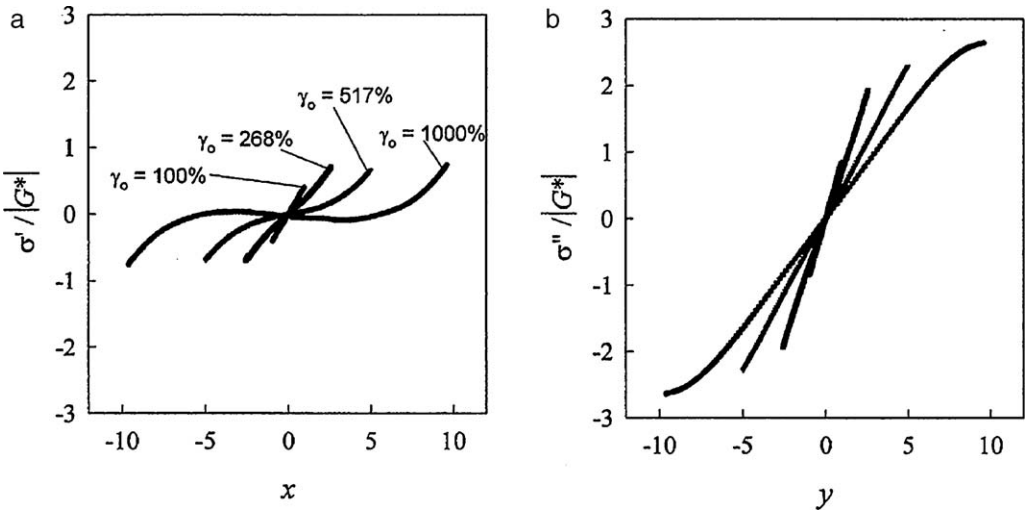

Fig. 23. Decomposition of shear stress into elastic and viscous part for polypropylene melt at 170 °C and 1 rad/s. The shear stress is normalized by the complex modulus in the linear regime. (a) Elastic stress vs. strain $x \equiv \gamma = \gamma_0 \sin \omega t$, (b) viscous stress vs. $y \equiv \dot{\gamma}/\omega = \gamma_o \cos \omega t$. Reproduced by permission of Cho et al. [66], copyright (2005) of the Society of Rheology.

ture of the measured material response with respect to strain or strain-rate which corresponds to a physical interpretation of the nonlinearity *within* a steady-state oscillatory cycle (intra-cycle nonlinearities of a nonlinear waveform). For the following discussion we focus on the positive domains ($\gamma > 0$, $\dot{\gamma} > 0$). The curvature (second derivative) of the elastic stress $\sigma'(\gamma)$ with respect to input strain amplitude can indicate either strain-stiffening (positive concavity; $d^2\sigma'/d^2\gamma > 0$), strain-softening (negative concavity; $d^2\sigma'/d^2\gamma < 0$), or linear elastic behavior (zero concavity). Similarly, the curvature of the viscous stress $\sigma''(\dot{\gamma})$ indicates shear-thickening (positive curvature; $d^2\sigma''/d^2\gamma > 0$) or shear-thinning (negative curvature). The magnitude of each Chebyshev coefficient typically decays monotonically with n, therefore to leading order positive curvature results for e_3, $v_3 > 0$, whereas negative curvature results for e_3, $v_3 < 0$.

The Chebyshev coefficients can be directly related to the more traditional Fourier coefficients described in Section 4.1. Although there is no explicit time dependence apparent in Eq. (46), the temporal variation in the stress can always be recovered by noting that $\bar{y} = \cos \omega t$ and $\bar{x} = \sin \omega t$, along with the identities $T_n(\cos\theta) = \cos(n\theta)$ and $T_n(\sin\theta) = \sin(n\theta)(-1)^{(n-1)/2}$ (n: odd). These Chebyshev coefficients are thus directly related to the Fourier coefficients of Section 4.1, Eq. (9), $e_3 = -G'_3$ and $v_3 = G''_3/\omega$. Similar identities are available for all of the higher Chebyshev coefficients [68]. The Fourier coefficients represent a complete mathematical description of the time-domain response, but the physical interpretation of higher harmonics is only revealed by considering the Chebyshev coefficients in the orthogonal space formed by the input strain and strain-rate.

The utility and interpretation of the Chebyshev coefficients is illustrated by examining a prototypical single mode nonlinear viscoelastic constitutive equation, the Giesekus model (see Appendix C). For a polymer solution, the Giesekus model captures the independent contributions of both a polymer stress ($\boldsymbol{\sigma}_p$) and a Newtonian solvent with viscosity η_s [131],

$$\sigma_s = 2\eta_s D \tag{52}$$

The total stress tensor is then

$$\sigma = \sigma_s + \sigma_p \tag{53}$$

This model (in multi-mode form) has been used by Calin et al. [140] to describe LAOS experiments with viscoelastic polymer solutions based on polyacrylamide [5]. Here the stresses predicted by the nonlinear Giesekus model are simulated under imposed oscillatory simple shear strain $\gamma = \gamma_0 \sin \omega t$, and analyzed as described previously [68]. For illustrative purposes, the following model parameters are used: $\lambda_1 = 1$ s, $\eta_s = 0.01$ Pa s, $\eta_p = 10$ Pa s, and the nonlinear parameter $\alpha = 0.3$. These four independent parameters result in a retardation time scale $\lambda_2 = \lambda_1 \eta_s/(\eta_s + \eta_p) = 0.001$ s and a polymer shear modulus $G = \eta_p/\lambda_1 = 10$ Pa. The Giesekus model for polymer solutions reduces to the linear Jeffreys model in the linear viscoelastic regime [2]. A frequency sweep in the linear regime ($\gamma_0 = 10^{-3}$) is shown in Fig. 24a. A strain-sweep at fixed frequency ($\lambda_1\omega = 1$) is shown Fig. 24b–f. This strain-sweep corresponds to the cross-over frequency at which $G' = G''$ in the linear regime. Fig. 24b shows the first-harmonic viscoelastic moduli, $G'_1(\gamma_0)$ and $G''_1(\gamma_0)$. Both moduli decrease as the strain amplitude is increased, and this is referred to as type I behavior (see Section 3.1). In other words, one observes *inter-cycle strain-softening* of G'_1 and *inter-cycle shear-thinning* of G''_1.

The coarse-level description of the actual material response using the first-harmonic moduli alone is insufficient to completely understand the nonlinear LAOS response. The full oscillatory response at each imposed strain amplitude is first revealed by presenting the raw steady-state oscillatory data in the form of parametric plots, correctly referred to as "Lissajous-Bowditch curves" [69] but for convenience we will simply use the term "Lis-

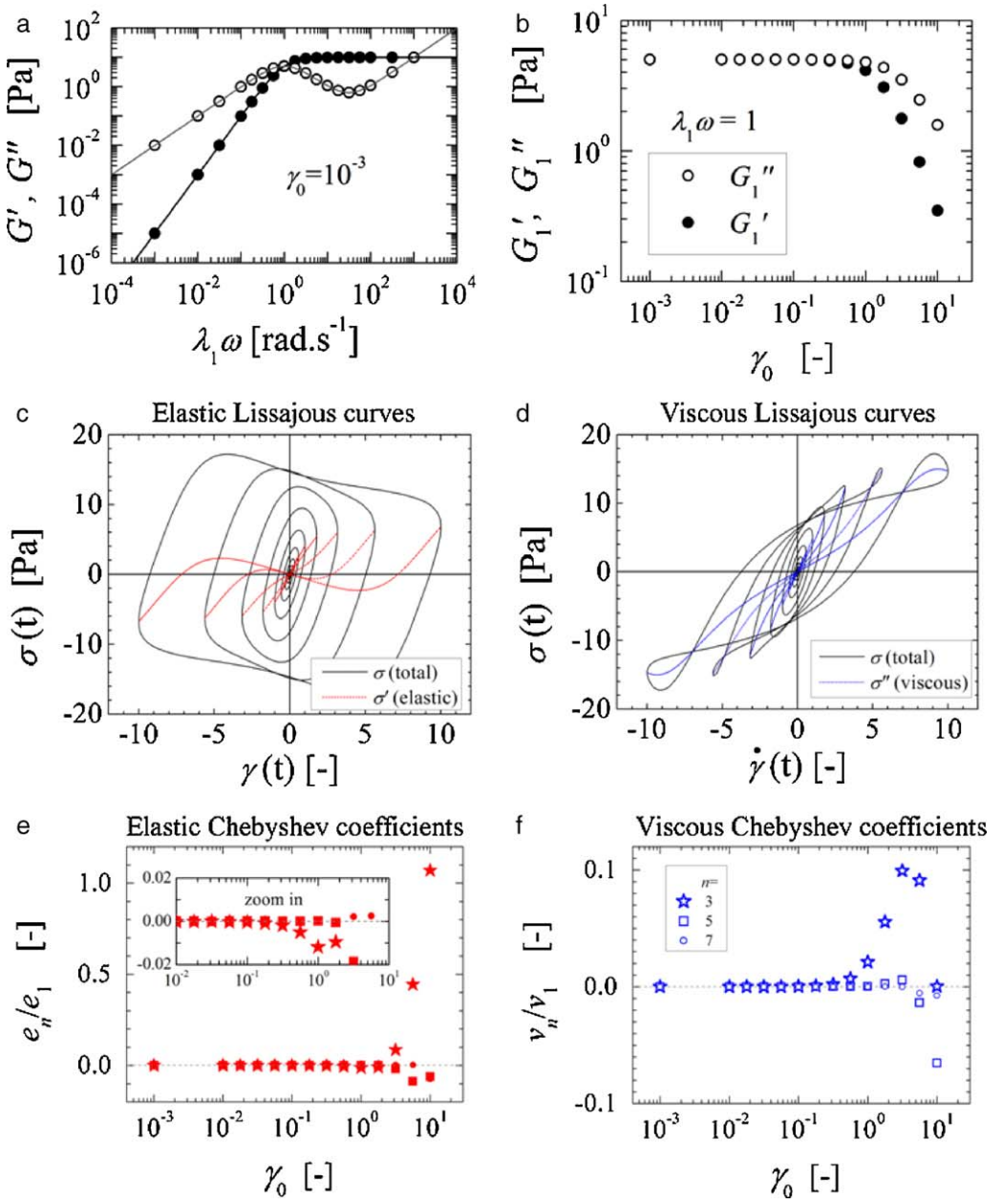

Fig. 24. Giesekus model simulation, characterized by LAOS. (a) Linear viscoelastic frequency sweep for $\gamma_0 = 10^{-3}$, points from numerical simulation of the Giesekus model, lines from analytical solution to Jeffreys model. (b–f) LAOS strain amplitude sweep at $\lambda_1\omega = 1$. (b) Coarse description using first-harmonic viscoelastic moduli shows a Type I response with strain thinning in both moduli. A more complete characterization is shown by Lissajous curves and Chebyshev coefficients, characterizing the model from the elastic perspective (c and e), and the viscous perspective (d and f). In (d) and (f) the higher harmonic coefficients are represented as $n = 3$ (⋆), $n = 5$ (■), and $n = 7$ (●), where filled symbols are used for elastic coefficients (e) and open symbols for viscous coefficients (f).

sajous curves." Elastic Lissajous curves are presented in Fig. 24c, and these plots display the total stress $\sigma(t; \gamma_0, \omega)$ (hysteretic loops) and the elastic stress (single-valued functions $\sigma'(\gamma(t))$ shown by red dashed lines) as the strain varies. In Fig. 24d we show the corresponding viscous Lissajous curves; i.e. parametric plots of stress vs. strain-rate; the total stress $\sigma(t; \gamma_0, \omega)$ (hysteresis loops) and the corresponding viscous stress $\sigma''(\dot{\gamma}(t))$ (single-valued blue dotted lines). The curvature in the decomposed stress contributions (red and blue lines) indicates the nature of the intra-cycle nonlinearities that contribute to the evolution of the polymer stress, and lends itself to a physical interpretation in terms of strain-hardening/softening, etc.

Quantitative values of the elastic and viscous Chebyshev coefficients for this simulation are shown in Fig. 24e and f, normalized by the first-harmonics as e_n/e_1 and v_n/v_1. From the third-order coefficients, it is observed that the initial elastic nonlinearity is strain-softening ($e_3 < 0$),

but this is followed by strain-stiffening ($e_3 > 0$) at larger imposed strains. The intracycle viscous nonlinearity is shear-thickening at this frequency, $\lambda_1\omega = 1$, as indicated by the sign of $v_3 > 0$.

The signs of the third-order Chebyshev coefficients are related to an alternate but equivalent representation of the nonlinear stress response in the time-domain. The stress output can be expressed by the magnitude and phase shift (similar to Eq. (8)), so that $\sigma(t) = \gamma_0 \sum |G_n^*| \sin(n\omega t + \delta_n)$, where the complex modulus at each order n depends on both imposed strain and frequency, and the phase shift δ_n is referenced to the input strain $\gamma = \gamma_0 \sin\omega t$. Trigonometric expansion of this expression gives $e_3 = -|G_3^*| \cos\delta_3$ and $v_3\omega = |G_3^*| \sin\delta_3$ for the third-order harmonics; thus the magnitude of the single parameter δ_3 conflates the nature of both viscous and elastic nonlinearities. Physical interpretation of the third-harmonic phase angle (δ_3) as revealed by the signs of the Chebyshev coefficients, is sketched diagrammatically in Fig. 25. Note that a given value of δ_3 can be simultaneously associated with both elastic and viscous nonlinearities, e.g. $\delta_3 = 45^\circ$ corresponds to viscous shear-thickening and also elastic strain-softening.

As we noted in Section 3.3, consideration of the phase angle δ_3 of the third harmonics helps understanding of the leading order influence of material nonlinearities on the shape of stress waveforms at large strain amplitude (see Figs. 8 and 9). However care must be taken to know how such phase angles are defined; here the phase angle relative to the input strain is used, δ_3, in contrast to Fig. 9 which used the phase angle relative to the fundamental harmonic of the stress output δ_3'. The Chebyshev decomposition naturally references the total system output to the input deformation.

The utility of the Chebyshev representation was recently demonstrated in the explanation of secondary loops (self-intersection) of Lissajous curves, interpreting the behavior with elastic stress overshoot [141]. Experimental measurements to demonstrate the advantages of the Chebyshev polynomial representation are presented in Section 5.3.3 (application to a biopolymer gel), and independent experimental studies are beginning to be published, e.g. [142,143].

4.5. Viscoelastic moduli in the nonlinear regime

The familiar viscoelastic moduli G' and G'' are clearly and uniquely defined only for the linear viscoelastic regime in which the stress response is a single-harmonic sinusoid. In the nonlinear regime the definition of viscoelastic moduli is not unique [144]. Here we review various methods of determining viscoelastic moduli from oscillatory data and discuss the interpretation in LAOS.

Methods for calculating viscoelastic moduli can be grouped into two categories: full-cycle methods and local methods. Full-cycle methods require at least one entire cycle of oscillatory data (or a half-cycle which is then mirrored), and include: (i) first-order Fourier or Chebyshev coefficients, which are defined by orthogonality relationships, e.g. $G_1' = \omega/(\pi\gamma_0^2) \oint \sigma(t)\gamma(t)\,dt$, and are the common output from commercial rheometers (note that in practice various methods can be used for determining G_1', as discussed by Franck et al. [145]); (ii) the so-called generalized elastic modulus $G_N' \equiv \sigma'_{max}/\gamma_0$ introduced by Cho et al. [66], in which σ'_{max} may occur at any value of instantaneous strain; (iii) a single-harmonic sine wave regression fit to the oscillatory stress curve $\sigma(t;\gamma_0,\omega)$, with elastic coefficient denoted as G_{SR}'; (iv) a first order polynomial regression fit to the elastic stress-strain curve $\sigma'(\gamma)$, denoted as G_{LR}' for linear regression; and (v) a polynomial regression fit of degree $M > 1$ in which the linear coefficient is denoted as G_{PR}' (for polynomial regression).

In contrast to full-cycle methods, local methods characterize the elastic modulus at a pre-defined instantaneous strain on a Lissajous curve and may equate to either a secant modulus or a tangent modulus. As described by Ewoldt et al. [68,69], two particularly useful measures of the nonlinear elastic modulus of a material can be determined from the raw stress curve of $\sigma(t)$ vs. $\gamma(t)$. At the minimum imposed strain the tangent modulus, or minimum strain modulus, can be defined as $G_M' \equiv d\sigma/d\gamma$ at $\gamma = 0$. At the largest imposed strain the secant modulus, or large strain modulus, is defined as $G_L' \equiv \sigma/\gamma$ at $\gamma = \gamma_0$. These measures are both identically equal to the elastic modulus G' for a linear viscoelastic response. An additional local measure of elastic modulus can be determined from the decomposed elastic stress curve $\sigma'(\gamma)$. It has been suggested that the differential elastic modulus (or tangent modulus) at the largest imposed strain be defined as $G_K' \equiv d\sigma'/d\gamma$ at $\gamma = \gamma_0$ [69]. All of the methods noted above will accurately determine the elastic modulus G' associated with the linear viscoelastic regime, but results may be distinctly different for a nonlinear response. Analogous viscous moduli (dynamic viscosities) can also be calculated from each methodology described above.

Table 2 shows the use of these methods to calculate the elastic moduli for the response of the Giesekus model at $\lambda_1\omega = 1$ and $\gamma_0 = 10^{-3}, 3.16, 10$ (using the model parameters described in Section 4.4). Each method results in the same value of elastic modulus in the linear regime, $\gamma_0 = 10^{-3}$, with some small variation due to different susceptibilities to numerical inaccuracy. In the nonlinear regime the modulus calculation is not unique, and different methods result in different values of elastic modulus.

The local measures have a precisely defined interpretation, since each is associated with a pre-defined instantaneous strain ($\gamma = 0$ or $\gamma = \gamma_0$). Full-cycle measures can have various interpretations, e.g. as average measures in the cases of G_1', G_{SR}', and G_{LR}'. These competing definitions may also overlap; for example, the generalized modulus G_N' is equivalent to the large strain modulus G_L' if the maximum elastic stress σ'_{max} occurs at maximum strain $\gamma = \gamma_0$. Another full-cycle measure, G_{PR}', connects with the local measure of minimum strain modulus $G_M' \equiv d\sigma/d\gamma$ at $\gamma = 0$. This connection arises because the polynomial regression acts as a Taylor expansion about $\gamma = 0$, and the leading order linear term therefore approximates the slope $d\sigma'/d\gamma$ at $\gamma = 0$.

Due to these differing and ambiguous interpretations of viscoelastic moduli in the nonlinear regime, it is imperative to state the method used for the calculation of such parameters. Each definition of viscoelastic modulus discussed here is a correct but non-unique measure of the

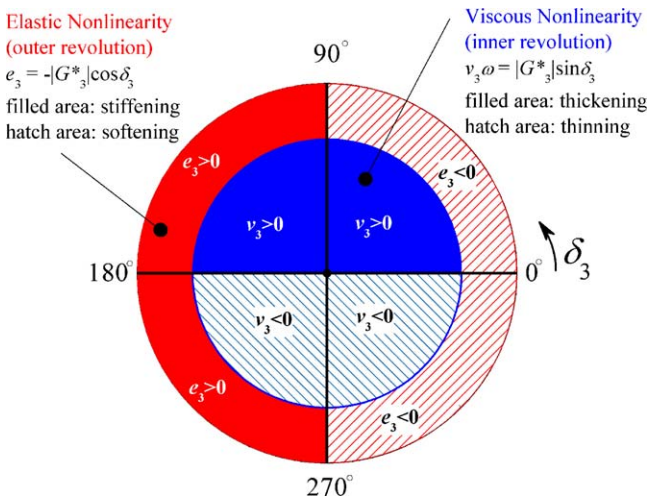

Fig. 25. Diagram summarizing the interpretation of the third-harmonic phase angle δ_3 (cf. Eq. (8)) as revealed by the third-order Chebyshev coefficients (cf. Eq. (51)).

material response in the nonlinear domain. The authors hope this discussion will emphasize why it is critical for researchers and instrument companies to report clearly the methods being used to calculate "viscoelastic moduli" from a nonlinear stress response. The proper combination of various methods can result in a more complete description of the complex nonlinear viscoelastic response [69].

4.6. Summary of quantitative methods

The aim of oscillatory rheological experiments is to systematically investigate nonlinear viscoelastic material responses, to connect quantitative nonlinear measures with microstructure or polymer topology, and to provide useful information about the behavior of materials during processing operations in which large strains are necessarily encountered. To achieve this, several different quantitative methods have been proposed. Different nonlinear material coefficients can be extracted depending on the method and the chosen frame of reference (i.e. time-domain or deformation-domain).

Within the framework of FT-Rheology ([33], Section 4.1), the higher harmonic contributions (intensity and phase angle) can be differentially observed and distinguished beyond the 100th harmonic contribution (Fig. 19). Of these higher harmonic contributions, the 3rd harmonic contribution represents the dominant nonlinear contribution as the leading-order emergence of nonlinearity. A new nonlinear coefficient, $Q \equiv I_{3/1}/\gamma_0^2$, was proposed by focusing on the relationship between the 1st and 3rd harmonic contributions ($I_{3/1} = I_3/I_1$) ([43], Section 4.1.1). In the case of polymer melts and solutions, the intensity ratio $I_{3/1}$ (γ_0) displays a sigmoidal or S-shape behavior ([33], Section 4.1.2). By contrast, dispersion systems typically exhibit a nonmonotonic behavior at intermediate strain amplitude as a consequence of the two phases present ([59], Section 4.1.2). Klein et al. ([5], Section 4.2) suggested an alternate method of analysis which integrates the higher harmonic contributions that are observed at sufficiently large strain amplitudes. This involves decomposition of the nonlinear response into a superposition of several periodic time-dependent basis functions representing canonical rheological behavior, e.g. sine (linear response), rectangle (strain softening), triangular (strain hardening), and saw tooth shaped waves (wall slip or shear banding). This method has the advantage of simplicity but the main disadvantage of this method is that the selected four basis functions are neither orthogonal nor unique.

By viewing the stress as a function of the mechanical input, Cho et al. ([66], Section 4.3) succeeded in decomposing nonlinear oscillatory stress waveforms (σ) into elastic stress (σ') and viscous stress (σ'') components. This perspective has been described as a geometrical interpretation, and is also referred to as stress decomposition (SD). Extending the concept of SD, Ewoldt et al. ([69], Section 4.4) resolved issues of uniqueness and nonorthogonality by using orthogonal Chebyshev polynomials of the first kind as basis function. The third-harmonic

Table 2
Various methods for reporting an elastic modulus from oscillatory shear data (analogous methods exist for reporting dynamic viscosity), applied to the Giesekus LAOS response at $\lambda_1\omega = 1$ (cf. Fig. 24). Units of elastic modulus are Pa, strain amplitude is unitless. The different definitions are given in the text.

γ_0	Full-cycle methods					Local methods		
	G'_1	G'_N	G'_{SR}	G'_{LR} ($M=1$)	G'_{PR} ($M=9$)	G'_M	G'_L	G'_K
10^{-3}	5.0000	4.9995	5.0013	5.0000	5.0108	5.0108	4.9995	5.0098
3.16	1.7690	1.8916	1.7918	1.7693	1.1172	1.1180	1.8916	2.4807
10	0.34760	0.67730	0.34733	0.34760	−0.65214	−0.67280	0.67730	2.3478

Table 3
Summary of quantitative methods used to analyze higher harmonics under LAOS deformations.[a]

	Time domain	Strain and strain-rate domain (orthogonal mechanical inputs)
Visualization	Oscillatory time series, $\sigma(\omega t)$	Lissajous curves, $\sigma(\gamma(\omega t), \dot{\gamma}(\omega t))$
Analytical representation	Fourier transform (FT) method, Fourier series	Stress decomposition (SD) method[b], polynomial series
Original publications	Philippoff [13] and Onogi et al. [14] – 1960, 1970 • First meaningful efforts to quantify nonlinear stress • Suffered from noise problem and the lack of technology at that time	Cho and Ahn et al. [66] – 2005 • Physical interpretation of nonlinear stress • "Elastic" and "Viscous" contributions of nonlinear stress
Subsequent developments	Giacomin and Dealy [8] – 1993 • Solved problem of high torque and edge fracture of high viscosity polymer melt system by mounting torque transducer at the middle of SPR (sliding plate rheometer) and Fourier series	Kim and Cho et al. [139] – 2006 • Least squares fitting of a polynomial series suffered from non-orthogonality issues during numerical calculation
	Wilhelm et al. [33] – 2002 • Dramatic increase of S/N ratio ($\approx 10^5$) and coupling of commercial rheometer with "high sensitivity oversampling" method using high performance ADC card • Focus on relative 3rd harmonic contribution, e.g. its intensity $I_{3/1}$ and its phase angle	Ewoldt and McKinley et al. [69] – 2008 • Solved non-orthogonality problem in evaluation of material functions by using orthogonal Chebyshev polynomials of the first kind • Suggested local measures for viscoelastic moduli, e.g. minimum-strain (G'_M) and large-strain (G'_L) elastic moduli and minimum-rate (η'_M) and large-rate (η'_L) dynamic viscosities
	Klein and Wilhelm et al. [5] – 2007 • Analyzing FT-spectra using superposition of various characteristic basis functions Leblanc [59] – 2008 • Simple five parameter equation of $I_{3/1}$ for filled compounds (or dispersion system) which show "overshooting" or "bump" at intermediate strain amplitude in plot of $I_{3/1}$ vs. γ_0	
	Hyun and Wilhelm [43] – 2009 • New nonlinear coefficient $Q \equiv I_{3/1}/\gamma_0^2$; other rheological properties which define scaling relationship between stress and amplitude of deformation	Yu et al. [130] – 2009 • Generalized the stress decomposition method for treating both odd and even higher harmonics using orthogonal Chebyshev polynomials of the first and second kind
Advantage	Detects odd, even, and non-integer higher harmonic contributions, high sensitivity, and traditionally easier to implement	Tends to enable a physical interpretation of the nonlinear viscoelastic response
Disadvantage	Physically-meaningful interpretation can be difficult	Detects only desired response, e.g. integer higher harmonics.
Summary	These two representations (time domain vs. deformation domain) complement each other and are interrelated. Many material measures can be calculated using either approach	

[a] In this table only quantitative methods are summarized, other analysis methods (e.g. visual inspection of Lissajous curve and stress shape analysis) are excluded.
[b] SD method itself is a stress shape analysis method, but other quantitative methods are based on the SD method.

contributions are still the leading-order nonlinearity, and in the deformation-domain the sign of the third-order coefficients can be physically interpreted in terms of elastic strain-stiffening/softening (for $e_3 = -G'_3$) and viscous shear-thickening/thinning (for $v_3 = G''_3/\omega$) (cf. Eq. (9) and (51), Fig. 25). Ewoldt et al. [69] also suggested local measures of the viscoelastic moduli in the nonlinear regime; the corresponding elastic moduli (the minimum-strain modulus G'_M and the large-strain modulus G'_L) and the dynamic viscosity (minimum-rate dynamic viscosity η'_M and large-rate dynamic viscosity η'_L), can be related to the Fourier coefficients (Eq. (9)) as follows

$$G'_M = \sum_{n=odd} nG'_n, \quad G'_L = \sum_{n=odd} G'_n(-1)^{(n-1)/2} \tag{54}$$

$$\eta'_L = \frac{1}{\omega}\sum_{n=odd} G''_n, \quad \eta'_M = \frac{1}{\omega}\sum_{n=odd} nG''_n(-1)^{(n-1)/2} \tag{55}$$

These new nonlinear viscoelastic moduli can also be used to effectively and unambiguously define terminology such as strain-stiffening/softening and shear-thinning/thickening (Section 4.5).

In Table 3 we summarize and categorize these quantitative methods. The methods are grouped according to the primary association with either a time-domain representation (Sections 4.1 and 4.2) or a deformation-domain representation (Sections 4.3–4.5). These two representations complement each other and are sometimes used interchangeably since the different nonlinear coefficients evaluated from each method are interrelated. The relative merits of each approach are typically associated

with ease of data processing (in the time-domain) compared to the ease of a physical interpretation (in the deformation-domain). The goal of any analysis method is to find meaningful nonlinear parameters to describe nonlinear data as a result of LAOS excitation. The next section demonstrates the application of this array of quantitative methods in rheological tests of various classes of viscoelastic materials.

5. Applications

In this article we have reviewed several methods to analyze the nonlinear response of materials undergoing large amplitude oscillatory shear flow. These methods can be applied to a wide range of different material systems. Because the nonlinear response of each subclass of complex fluid (e.g. polymer solution or melt, dispersed system, blockcopolymer, or biopolymer gel) can be very different, each approach has its own merits and disadvantages. Here we survey several recently published LAOS investigations of different complex fluids. These examples are not intended to be exhaustive but rather to serve as case studies that illustrate the utility of the analysis tools reviewed in the previous sections.

5.1. Entangled polymer systems

FT-Rheology under LAOS is now recognized as a very sensitive characterization method for detecting long chain branching (LCB) – or more generally to distinguish different polymer topologies. Experiments have shown that the ratio $I_{3/1}$ and the phase angle of the third harmonic (δ_3) are sensitive to macromolecular architecture, specifically the molecular weight distribution, number of branches, and their length [36,37,39,45]. However, these early publications did not systematically explore LAOS using a well defined, entangled homopolymer to provide a baseline for our rheological understanding of the influence of excitation frequency, temperature, or molecular weight. Hyun et al. [43] presented the first systematic investigation of the evolution in the nonlinear ratio ($I_{3/1}$) obtained from FT-Rheology, and proposed a new nonlinear coefficient $Q(\omega, \gamma_0)$ for quantifying the response of monodisperse linear polystyrene and comb polystyrene melts. They also investigated the *zero-strain nonlinearity*, Q_0 obtained in the limits of small strain amplitude ($\lim_{\gamma_0 \to 0} Q \equiv Q_0$) that characterizes the onset of nonlinearity of each sample (Section 4.1.1). We provide a review of this systematic study here, in which anionically synthesized monodisperse linear and comb polystyrenes (PS) were used (see Table 4). The PS comb series C6 consists of a linear backbone with weight-average molecular weight of the backbone M_b = 275 kg/mol, and approximately q = 25–30 linear branches of varying molecular weight arms with M_a varying from 11.7 to 47 kg/mol. For PS a typical literature value of the entanglement molecular weight is M_e = 17 kg/mol [43]. The sample C622 therefore has unentangled arms, whereas sample C632 is expected to have entangled arms. The ratio of intensities $I_{3/1}$ was measured as a function of strain amplitude at various excitation frequencies from 0.1 rad/s to 10 rad/s and the corresponding value of the Q coefficient ($= I_{3/1}/\gamma_0^2$) was then calculated (Fig. 26). It is clear that the coefficient approaches a constant value (corresponding to a 'zero-strain nonlinearity', Q_0) at small strain amplitude (Fig. 26c and d) with residual fluctuations that arise from the low magnitudes of the intensity ratio ($3 \times 10^{-4} < I_{3/1} < 10^{-2}$) in the limiting asymptotic regime. Because Q_0 is evaluated from several data points (typically 5–10), very reliable values of the asymptotic value obtained in the limit of zero-strain can be determined.

5.1.1. Frequency-dependence of $Q_0(\omega)$ in the asymptotic regime

In Fig. 27, the values of Q_0 for the linear and comb PS samples are plotted at a reference temperature of T_{ref} = 190 °C. The data for the monodisperse linear PS as a function of frequency displays a single local peak value and terminal quadratic behavior ($Q_0 \propto \omega^2$) at low frequencies (Fig. 27b). The quadratic scaling ($Q_0 \propto \omega^2$) at the low-frequency limit is expected from the analysis for the Doi-Edwards model presented by Pearson and Rochefort [20] (see Appendix D). As the molecular weight increases, the transition to terminal behavior shifts to lower frequencies (analogous to the familiar frequency shift observed in conventional linear viscoelastic properties) and the peak becomes increasingly broad. In the case of the comb PS sample with unentangled branch chains (C622), $Q_0(\omega)$ displays a similar shape as a function of frequency (with one maximum value and a terminal regime ($Q_0 \propto \omega^2$)). In contrast to the linear samples, however, the maximum value of Q_0 is lower than for the comb PS PS melts. The authors conjectured that this might result from the dynamic tube dilution induced by the side branches. For the comb PS with entangled side branches (C632 and C642), $Q_0(\omega)$ has two peak values, one corresponding to the branches' disentanglement at higher frequencies and the second arising from backbone relaxation at lower frequencies (see Fig. 27a). As a consequence of having entangled branches, the maximum value of Q_0 can be associated with the backbone relaxation ($Q_{0,b}$) and is much lower than that of the comb PS with unentangled branches (C622). As the entangled branch chain length becomes longer, the value of $Q_{0,b}$ drops progressively and the frequency dependence becomes narrower and sharper (see Fig. 27b). In the case of the comb PS series (C622, C632 and C642), the volume fraction of the backbone chain decreases as the side branch length increases. From the viewpoint of dynamic tube dilution, the fully-relaxed side-branches act as an effective solvent for the unrelaxed backbone chain. The increasing length of the side branches has a similar effect to decreasing the concentration of the main backbone chain in a viscous solvent. Quantitative measurement of $Q_0(\omega)$ can thus effectively probe frequency dependence in the relaxation processes associated with disentanglement for a range of polymer melts.

5.1.2. Strain-dependence of $Q(\gamma_0)$ under LAOS

The behavior of the coefficient Q with increasing strain amplitude is investigated at a fixed frequency in Fig. 28. For monodisperse linear PS melts, Q decreases as the strain amplitude increases at various frequencies, which is reminiscent of the shear thinning observed in the viscosity as

Table 4
Molecular characteristics of the samples used.

Sample	M_b (kg/mol) backbone	M_a (kg/mol) branch	q (branches/backbone)	M_{total} (kg/mol)	$\langle\tau_G\rangle_w$ (s)[a] at 190 °C	Molecular structure
PS 76k	75.9	–	–	75.9	0.05	Linear
PS 100k	100	–	–	100	0.14	Linear
PS 220k	214	–	–	214	2.66	Linear
PS 330k	330	–	–	330	12.44	Linear
C622-PS	275	11.7	30	624	11.63	Comb
C632-PS	275	25.7	25	913	28.59	Comb
C642-PS	275	47	29	1630	102.06	Comb

[a] The terminal relaxation time was evaluated from linear moduli data at 190 °C.

a function of shear rate. By contrast, the value of $Q(\gamma_0)$ for the comb PS sample with entangled side branches (C642) increases as the strain amplitude increases. The normalized variation in the nonlinearity Q/Q_0 as a function of strain amplitude can be compared to the normalized complex modulus $|G^*/G_0^*|$ where $|G_0^*|$ is the complex modulus measured under SAOS conditions at a fixed frequency, see Fig. 28a. For the linear PS melt, both functions decrease as the strain amplitude increases. Similar results are obtained for the comb PS melt with unentangled side branches. On the contrary, for the comb sample with entangled side branches (C642), $|G^*/G_0^*|$ decreases, whereas the ratio Q/Q_0 increases with strain amplitude (Fig. 28c) for specific frequencies. It is well known that the extent of strain hardening behavior in elongational flow is directly connected to branched polymer chains. The increase in the nonlinear coefficient Q also reflects the role of chain branching. Although it is clear that chain topology plays a role, the underlying nonlinear physics controlling the variation in $Q(\gamma_0)$ with increasing strain amplitude are still not fully understood. The strain-dependence observed in $Q(\gamma_0)$ appears to be a promising parameter for detecting long chain branching in commercial branched polymers, e.g. LCB-PE, however further theoretical and experimental work is required to fully evaluate the sensitivity of such a probe.

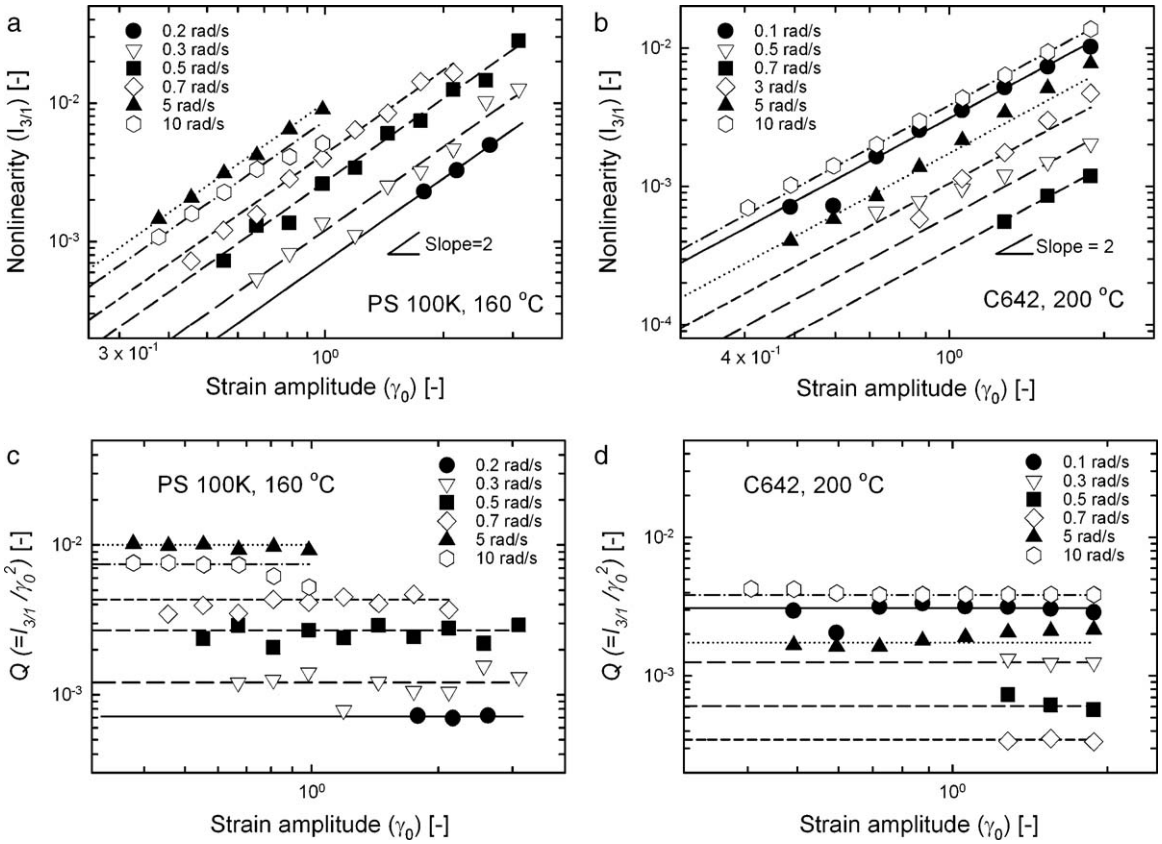

Fig. 26. The nonlinear intensity ratio ($I_{3/1}$) as a function of strain amplitude for linear and comb PS at various frequencies: (a) linear monodisperse polystyrene (PS 100K) at 160 °C, (b) entangled branched melt C642 at 200 °C. Also shown are the corresponding values of the Q coefficient as a function of strain amplitude evaluated from the intensity ratio data for (c) PS 100K at 160 °C and (d) C642 at 200 °C. Reproduced by permission of Hyun et al. [43], copyright (2009) of American Chemical Society.

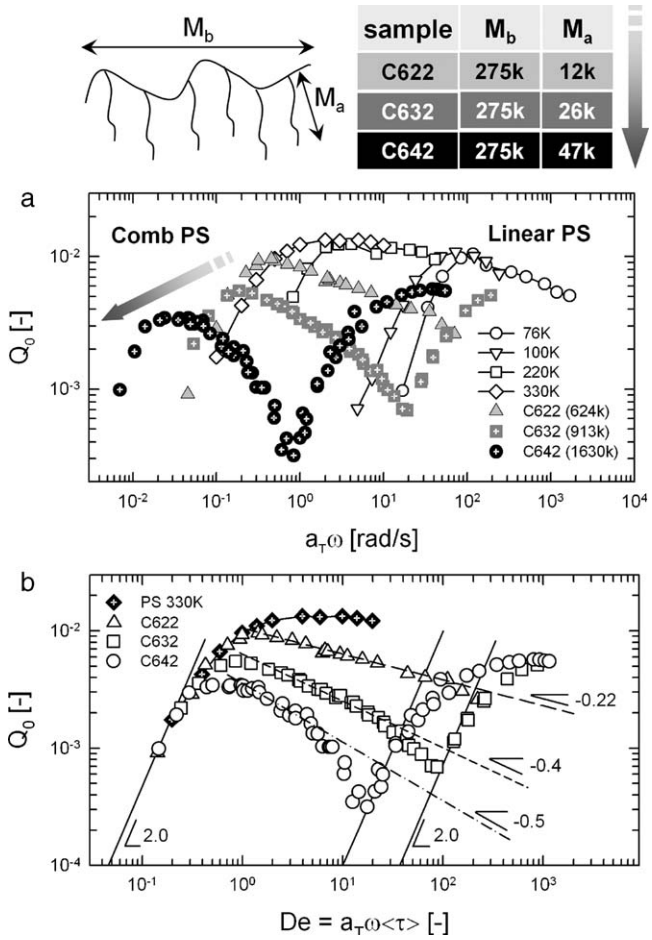

Fig. 27. (a) Frequency dependence of the zero-strain nonlinearity Q_0 for linear PS chains (PS 76K, 100K, 220K, 330K) and PS combs (C622, C632 and C642) at T_{ref} = 190 °C. With increasing molecular weight of the branched chain (M_a), the maximum corresponding backbone chain ($Q_{0,b}$) is decreasing. (b) For clear comparison, the coefficient Q_0 is plotted against Deborah number ($De = a_T\omega\langle\tau\rangle$) of linear PS 330K and comb PS (C622, C632 and C642) at T_{ref} = 190 °C. Reproduced by permission of Hyun et al. [43], copyright (2009) of American Chemical Society.

5.2. Dispersion systems

There have been many LAOS investigations of the non-linear rheology exhibited by dispersed systems and these include some of the very first reports of the LAOS protocol. Materials of interest have included clay–water systems [12], carbon black in PS solution [14], spherical polymer particles in PS solution [16], soft hydrogel microspheres [80], particle suspensions [5], immiscible polymer blends [46,146] and others.

5.2.1. Suspensions

Analysis of the non-linear oscillatory properties of water-based polymer dispersions do not always result in a simple physical picture of how the amplitudes and phases of the harmonics evolve. As we have noted above, the bulk of previous studies have focused on the magnitude of the third harmonic $I_{3/1}$ and the corresponding phase δ_3. In many cases this restricted analysis is justified due to the fact that the intensity of the higher harmonics, e.g. 5th, 7th, etc., are negligibly small. However, in the hard sphere model systems examined here, a large number of higher harmonics of the excitation frequency with high intensity are often detected (possibly up to the 45th harmonic). Moreover, in such samples not only odd harmonics, but also even harmonics are observed. In this limit, The Characteristic Functions method (see Section 4.2) enables convenient analysis of the Fourier spectra of the non-linear mechanical behavior of dispersions because each selected characteristic function is composed of many higher order contributions [5]. To illustrate this, we use two model hard-sphere suspensions with different average particle diameters (Table 5). The measured and reconstructed LAOS data for sample 1 and sample 2 is shown

Table 5
Characterization of samples using particle dispersity index (PDI), solid content, and particle diameter for two monodisperse hard-sphere suspensions (denoted sample 1 and 2).

	Sample 1	Sample 2
PDI	1.04	1.01
Solid content [%]	35.4	32.7
Particle diameter [nm]	69.7	133.2

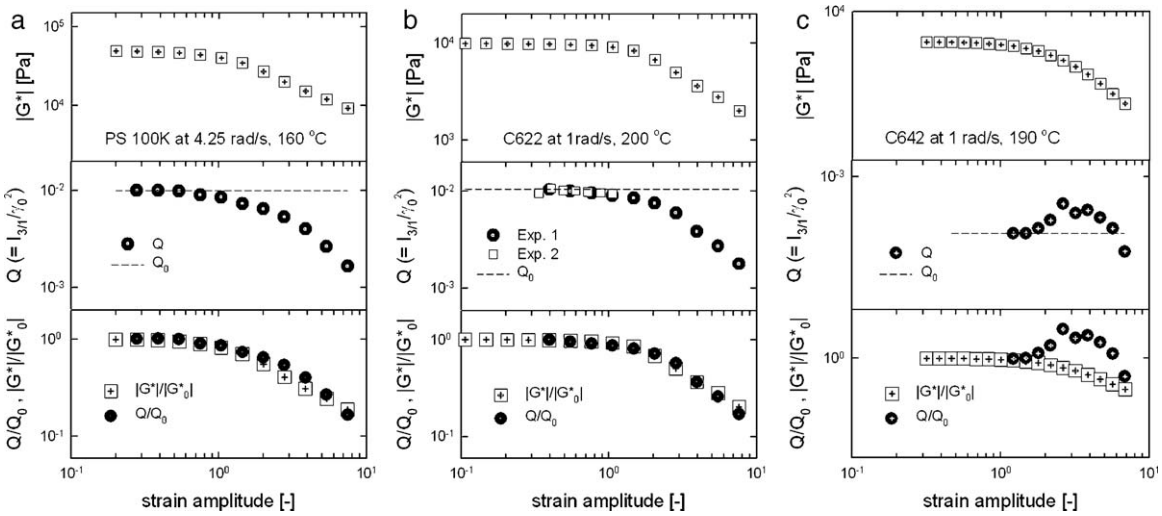

Fig. 28. The magnitude of the complex modulus $|G^*|$ and Q as a function of strain amplitude from medium strain amplitude ($\gamma_0 \approx 0.25$) to large strain amplitude ($\gamma_0 \approx 7$). (a) Monodisperse linear PS (PS 100K) at $\omega = 4.25$ rad/s, $T = 160\,^{\circ}$C, (b) comb PS with unentangled side chains (C622) at $\omega = 1$ rad/s, $T = 200\,^{\circ}$C, and (c) comb PS with entangled branches (C642) at $\omega = 1$ rad/s, $T = 190\,^{\circ}$C. The $|G^*|(\gamma_0)$ curves display only strain softening for all three samples. In contrast, the curves of $Q(\gamma_0)$ for the linear PS and comb PS with unentangled branches (C622) exhibit strain softening with increasing strain amplitude, whereas the corresponding curve for the comb PS with entangled branches (C642) displays strain hardening. Reproduced by permission of Hyun et al. [43], copyright (2009) of American Chemical Society.

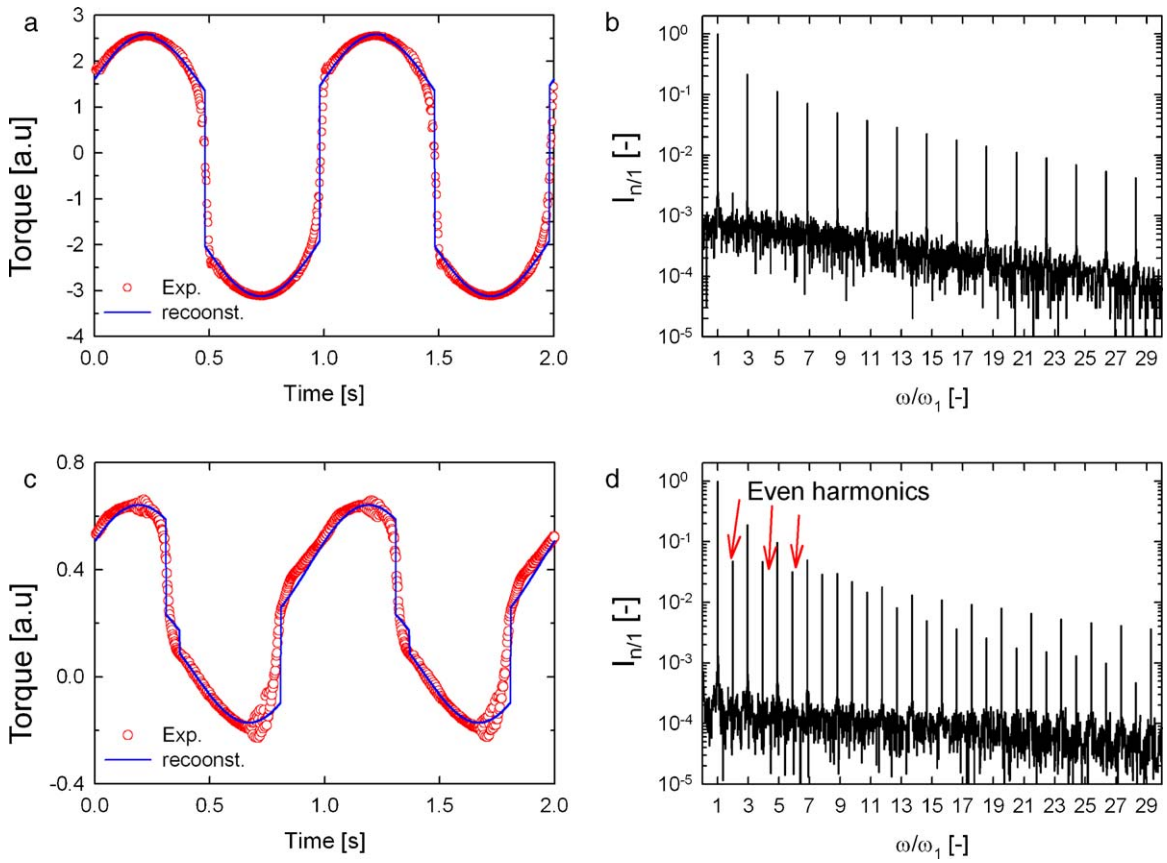

Fig. 29. The overlay of the time-dependent torque response and the reconstructed time data and the corresponding FT spectra of the experimental data for sample 1 (a and b) and sample 2 (c and d). The time domain signals were recorded at 298 K with $\omega_1/2\pi = 1$ Hz, $\gamma_0 = 1$ for sample 1 and $\gamma_0 = 6$ for sample 2. Reproduced by permission of Klein et al. [5], copyright (2009) of American Chemical Society.

Table 6
Amplitude, phase angle and time lag of the three characteristic functions that generate the reconstructed response of sample 1 and sample 2 shown in Fig. 29.

	Sinusoidal		Rectangular		Saw tooth	
	Sample 1	Sample 2	Sample 1	Sample 2	Sample 1	Sample 2
Normalized amplitude	1	1	1.47	1.4	<0.01	0.36
Phase angle [°]	0	0	35	51	[a]	~0
Time-lag [ms]	0	0	97	142	[a]	~0

[a] Below accuracy.

in Fig. 29a and c. The FT magnitude spectrum for each suspension is presented in Fig. 29b and d. The measured and reconstructed data superpose well near the maxima, but deviations appear close to the turning point of the periodic functions (where the torque is zero). The different relative contributions of the four characteristic functions, their amplitudes, phases, and time-lags, are presented in Table 6. The triangular-wave function (representing thickening) was not used because the system showed only shear-thinning behavior. The time-lag is defined from the phase shift between the linear contribution and the strain softening or shear-banding contribution. Note the dramatic differences between both the time and frequency-domian data for the two samples, this is readily identified as arising from the big difference in the saw-tooth contribution for the two suspensions.

In a subsequent stage, this decomposition of the mechanical response was then applied to a complete data set of oscillatory responses varying only in the applied strain amplitudes. In a strain sweep test, both of the samples showed the same LAOS type III behavior (see Section 3.2). However, the characteristic functions obtained from the reconstructed stress data can distinguish the two samples, especially due to the contribution of the saw-tooth functions. Because the characteristic functions method incorporates the contributions of many higher-order harmonics, it can readily differentiate between the two samples. The amplitude and phase angle of each basis function as a function of strain amplitude for two hard sphere model systems are represented in Fig. 30. The values of the amplitudes are normalized with respect to the amplitude of the pure sinusoidal function. The sinusoidal response was used as reference with the amplitude set to $A_l = 1$ and a phase angle $\delta_l = 0$ (Eq. (38)). The phase values of the rectangular, triangular, and saw tooth function are referenced to this sine function phase angle. The three characteristic functions that capture the linear response, strain softening, and wall slip are needed to obtain a satisfactory match to the experimental data, in particular at high strain amplitudes. With increasing strain amplitude γ_0, the amplitude of the rectangular function increased until a maximum is reached. For sample 1, the amplitude of the saw-tooth function is considerably lower as compared with the rectangular function (please note the double logarithmic scale). The phase angles of the two functions increase slowly with increasing γ_0, but the difference between them is almost constant. The phase angle of the rectangular function is about 360°, and therefore in-phase with the linear contribution. About 20 different dispersions were found to respond in a similar way. An exception to this finding is the behavior of sample 2. In fact, at small values the saw tooth function is larger in amplitude than the rectangular function. At a value of $\gamma_0 = 0.06$, both contributions show a strong increase and a cross-over in relative amplitude. A large change is also observed in the phase angle of both functions.

5.2.2. Emulsions

Small amplitude oscillatory shear tests are a reliable way of extracting a characteristic droplet size for emulsions [147]. Carotenuto et al. [46] proposed using LAOS to determine not only the characteristic dimension of an immiscible polymer blends but also to infer the size distribution of the drops. The principal idea is that even an emulsion formed from two immiscible Newtonian fluids will exhibit a viscoelastic response due to the interfacial tension, and this response will become nonlinear when sufficiently large amplitude shear is applied to the emulsion droplets. Consequently the droplet size and the size distribution will drastically affect the intensity and phase of the different higher harmonics in the FT-rheology spectra. Conversely, some information about this size distribution can be obtained from analysis of the FT-Rheology spectrum as shown in Fig. 31.

5.2.3. Polymer blends

Filipe et al. [47,48] investigated the evolution in the morphological and rheological properties along the length of a screw extruder for blends of a commercial liquid crystalline polymer (LCP) and polypropylene. They collected samples at different locations (labeled v1–v11) along the extruder (Fig. 32a), and examined the morphology of the samples using SEM and light microscopy. Rheological properties of the collected samples were measured using linear oscillatory tests (SAOS) and nonlinear oscillatory tests (LAOS). It was concluded that the nonlinear tests, e.g. the nonlinearity ratio ($I_{3/1}$) obtained from FT-Rheology, were more sensitive than linear viscoelastic tests (SAOS) for probing the morphology evolution along the extruder length. During the extrusion process, the morphology of the LCP dispersed phase can change from spherical to elongated droplets or fibrillar structures depending on the position along the extruder, and this is reflected in a progressive change in the nonlinear rheology from the beginning to the end of the extrusion process (Fig. 32). It is thus possible to extract information about both the average dimension of the dispersed phase structure as well as the change in morphology under large amplitude shear. This

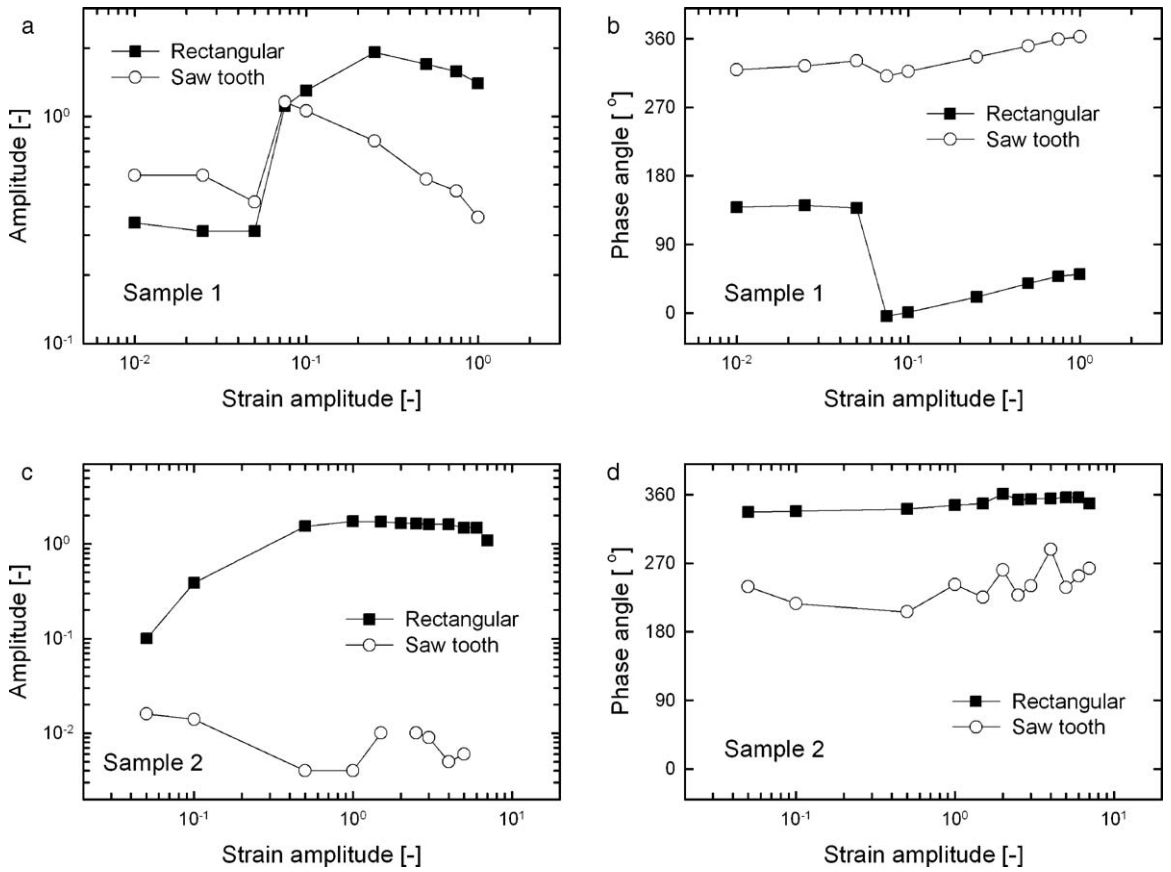

Fig. 30. Dependence of the amplitude and the phase angle on the strain amplitude of the characteristic functions for sample 1 ((a) amplitude and (b) phase angle) and sample 2 ((c) amplitude and (d) phase angle). The characteristic response contains strain softening (rectangular basis function) and wall slip or shear banding (saw tooth wave form). In rare cases, experimental problems such as wall slip appeared. In those cases the data is not shown. Reproduced by permission of Klein et al. [5], copyright (2009) of American Chemical Society.

conclusion is consistent with the results of Carotenuto et al. [46] discussed in the previous section.

5.2.4. Filled rubber compounds

Leblanc [52,55–60] and Leblanc et al. [53,54,61] have investigated many kinds of industrial rubber and elastomers both with and without added filler. They observed that the ratio $I_{3/1}$ of filled rubber compounds does not show simple sigmoidal function (see Eq. (33)) because of a strain overshoot detected at intermediate strains (around $\gamma_0 \approx 5$–6) [59]. Such behavior is obtained using systems in which strong interactions occur between the viscoelastic matrix, i.e. the major volume phase, and the dispersed phase, i.e. the carbon black. Therefore, the nonlinearity

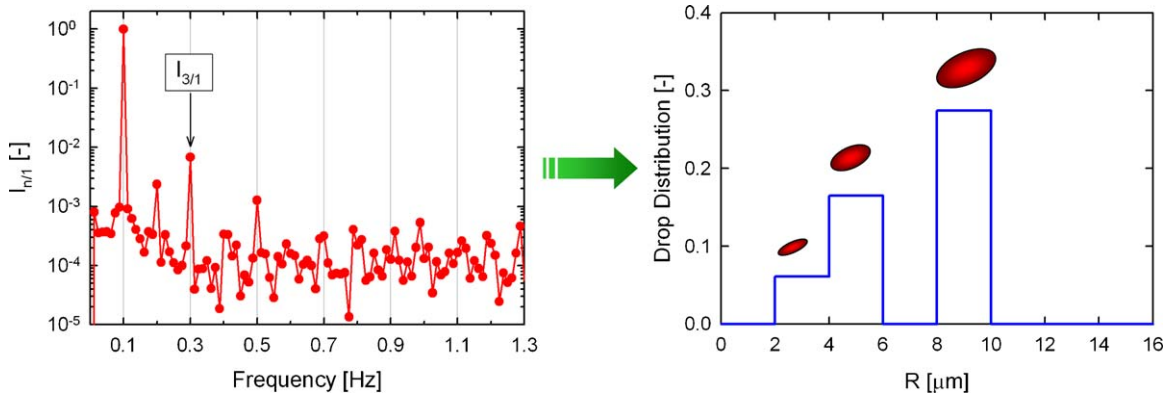

Fig. 31. Drop distribution estimated with the regression procedure for blend C (10% PDMS and 90% PIB) using the FT-Rheology spectra. Reproduced by permission of Carotenuto et al. [46], copyright (2009) of American Chemical Society.

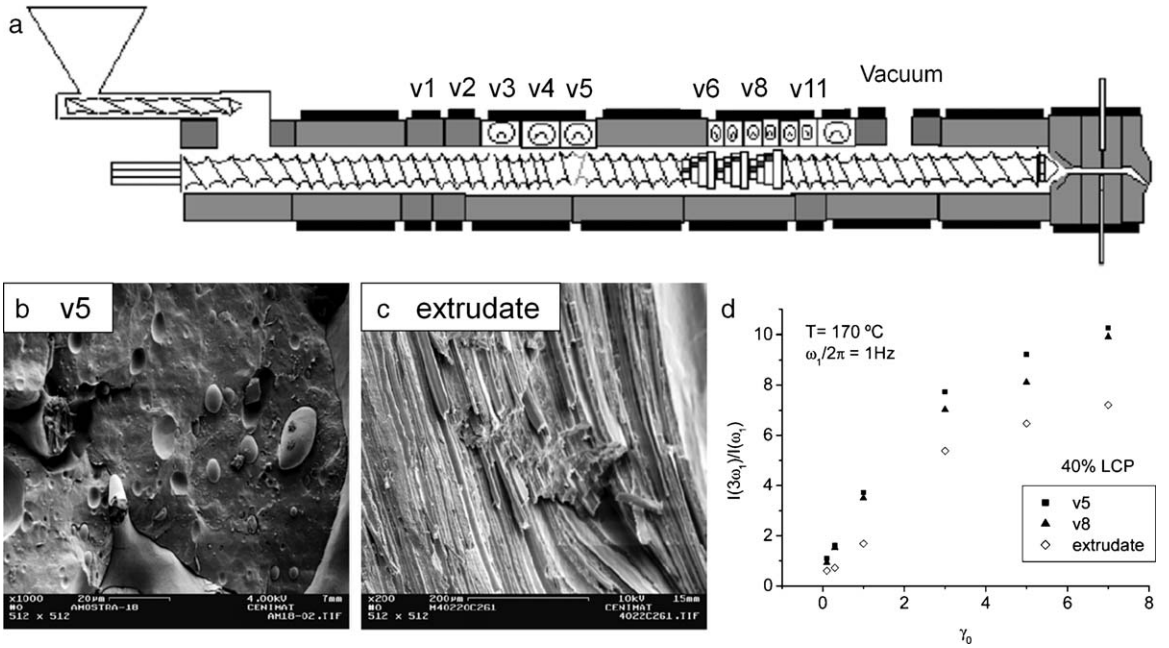

Fig. 32. (a) Screw and cylinder profile used for the processing of the blends. Here "v*i*" is *i*th valve that allows local removal of samples along the extruder length. Morphological evolution along the length for the blend with 40 wt% LCP processed at 220 °C (SEM). (b) location v5 in the extruder and (c) final extrudate. (d) Ratio $I_{3/1}$ from FT-Rheology as a function of the applied strain amplitude for the different samples collected along the extruder length (blend with 40 wt% LCP at 170 °C). Reproduced by permission of Filipe et al. [47], copyright (2004) of Elsevier Science.

appears to reflect the superposition of two responses: one qualitatively common to all "pure" (unfilled) polymers and a separate "filler" response ([60], see also Section 4.1.2). At low strain amplitude, the nonlinearity is essentially dominated by the filler component (dispersed phase) and at higher strain amplitude the influence of the filler is less pronounced and the nonlinearity arises primarily from the polymer component (continuous phase) [59]. A fitting of model parameters provides information on the viscoelastic behavior of filled rubber compounds affected by the filler content with little effect of the matrix material (typically limited to high cis-1,4-polybutadiene and natural rubber). The type and grade of carbon black added to the system is also found to affect the nonlinear shear stress of filled rubber compounds, and results, for example, in the "forward" tilted or "backward" tilted stress forms discussed in Section 3.3. Leblanc suggested quantifying the "backward" and "forward" tilted shapes of the shear stress using quarter cycle integration from one cycle of shear stress data as a function of time. The ratio of the first quarter stress (Q1) and second quarter stress (Q2) signal integration, i.e., Q1/Q2 (=1 in case of no distortion sinusoidal shear stress curve) allows a clear distinction between "forward" tilted (Q1/Q2 > 1) and "backward" tilted (Q1/Q2 < 1). The unfilled material was found to exhibit a Q1/Q2 ratio that is always larger than unity and increases with strain amplitude i.e. a "forward" tilted stress [59]. In the case of a carbon black filled elastomer, the Q1/Q2 ratio was first found to be higher than one at low strain amplitudes, then quickly dropped below one with increasing strain amplitude corresponding to a "backward" tilted stress. With these two methods, Leblanc [61] investigated thermoplastic vulcanizates (TPV) which are blends of a crystalline thermoplastic polymer (polypropylene) and a vulcanizable rubber composition and Leblanc and Nijman [148] investigated silica-based rubber compounds.

5.3. Block copolymers and gels

5.3.1. Block copolymer melts

LAOS has been used to study the orientation/reorientation processes in microphase-separated lamellar PS-*b*-PI diblock copolymers as well as in diblock and triblock copolymers of styrene and butadiene (PS-PB; PS-PB-PS) which form lamellar microphases [50,149] at temperatures well above the glass transition temperature (T_g) of PS. The alignment kinetics can be studied in detail via online monitoring of the degree of mechanical nonlinearity exhibited during the orientation process – as determined via the higher harmonics in FT-Rheology – coupled with investigation of the orientational distribution by *ex situ* two-dimensional small angle X-ray scattering (2D-SAXS). For the PS-PI polymer, both methods detected parallel alignment of the lamellae after increasing the frequency of shearing as well as spatially heterogeneous alignment via bimodal parallel and perpendicular alignment of the lamellae [149].

The rheological behavior of both unaligned and aligned diblock and triblock copolymers of styrene and butadiene (PS-PB; PS-PB-PS) lamellar phases were studied later in [50]. The evolution of the microstructure during the flow alignment process can be easily quantified using the FT-Rheology technique.

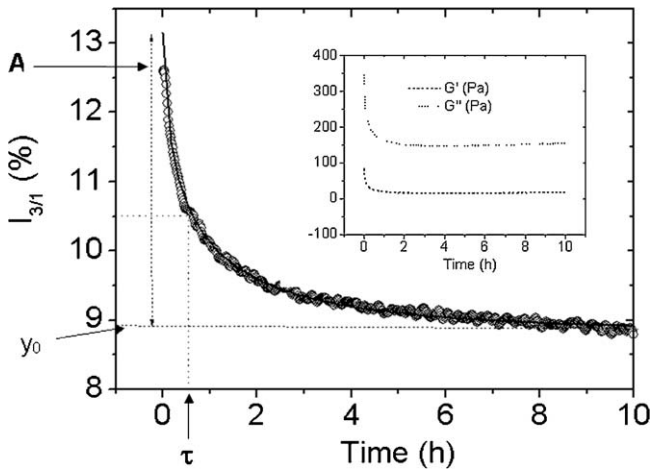

Fig. 33. Variation of the relative intensity of the third harmonic $I_{3/1}$ (○) during the 10hours of the macroscopic orientation process of a styrene–butadiene (9 kg/mol–9 kg/mol) sample. The solid line represents the stretched exponential fit. The insert represents the variation of the storage modulus and the loss modulus as a function of time. Reproduced by permission of Oelschlaeger et al. [50], copyright (2007) of WILEY-VCH.

For di- and triblocks, parallel alignment is achieved at low frequency and temperatures below the order/disorder transition temperature T_{ODT}. The kinetics of orientation can be quantified by the intensity of the third harmonic $I_{3/1}(t)$ as shown in Fig. 33. Specifically $I_{3/1}(t)$ can be described by a stretched exponential function with a characteristic relaxation time τ.

$$I_{3/1} = y_0 + A \exp\left[-\frac{t}{\tau}\right]^{\beta} \tag{56}$$

For di- and triblock copolymers, the kinetics of orientation strongly depend on the strain amplitude and the time constant varies with a scaling exponent: $\tau \propto \gamma_0^{-4}$ for the diblock and $\tau \propto \gamma_0^{-2.85}$ for the triblock. This scaling exponent greatly exceeds the expected scaling of $\tau \propto \gamma_0^{-1}$ which corresponds to a physical process in which the total applied deformation is responsible for the observed orientation. The larger scaling exponent might be explained by the cooperative nature of the underlying processes. Analysis of the time-dependent variation in the phase difference related to the third harmonic ($\delta_3(t)$) enables further differentiation between the diblock and triblock for the PS-PB and PS-PB-PS model systems. The plateau value of δ_3 is independent of the strain amplitude and frequency but depends on the morphology of the system, at least within the lamella systems investigated to date. For the PS-PB diblock, $\delta_{3\,plateau} \approx 170^{\circ}$ and for the PS-PB-PS triblock $\delta_{3\,plateau} \approx 140^{\circ}$. The reorientation from a parallel to a perpendicular orientation is only possible for the diblock copolymer. For the triblock samples, the complementary X-ray analysis revealed a time-dependent bimodal orientation distribution. This observation suggests a complex mechanism for reorientation from parallel to perpendicular alignment, which is the subject of ongoing investigations. In summary, FT Rheology offers a new and simple way for online monitoring of complex reorientation kinetics in blockcopolymer melts or solutions.

5.3.2. Block copolymer solutions

Poly(ethylene oxide)–poly(propylene oxide)–poly (ethylene oxide) (PEO–PPO–PEO) triblock copolymers, often referred to by their trade names of Pluronic (BASF) or Synperonic (ICI), have been widely used in industry as amphiphilic rheology modifiers. Aqueous solutions of poly(propylene oxide) (PPO) exhibit a dramatic temperature dependence; below approximately 15 °C, water is a good solvent for PPO, whereas PPO aggregates at higher temperature. Poly(ethylene oxide) (PEO), on the other hand, is hydrophilic over the whole temperature range from 0 to 100 °C. With a block of PPO and two blocks of PEO combined into a single polymer chain, one can expect amphiphilic characteristics with interesting aggregation phenomena [150]. Daniel et al. [49] studied the nonlinear response of a face-centered cubic (fcc) micellar structure formed by a PEO–PBO diblock copolymer in aqueous solution. Hyun et al. [6] investigated a 20 wt% aqueous solution of PEO–PPO–PEO triblock copolymers subjected to LAOS at different temperature. As the sample temperature changes, the transition between a soft gel and a hard gel is revealed by LAOS measurements and the material response can be classified with respect to LAOS type according to the definitions proposed by Hyun et al. [63]. The sol shows Newtonian behavior (strain-independent G'') at temperatures below the transition. By increasing the temperature a soft gel forms and type I (monotonic strain thinning) appears. As the temperature increases, type IV responses (strong strain overshoot; local maxima in G' and G'') are observed at large strain amplitude. Therefore the LAOS signature of a soft gel displays a combination of type I and type IV behaviors (Fig. 34a). However, as the temperature is increased further, the type IV response becomes weaker, and finally the strain overshoot (characteristic of a type IV response) disappears at the transition temperature from soft gel to hard gel. Finally, the hard gel shows a type III response (G' decreasing, with a local maximum in G'' alone) as shown in Fig. 34b.

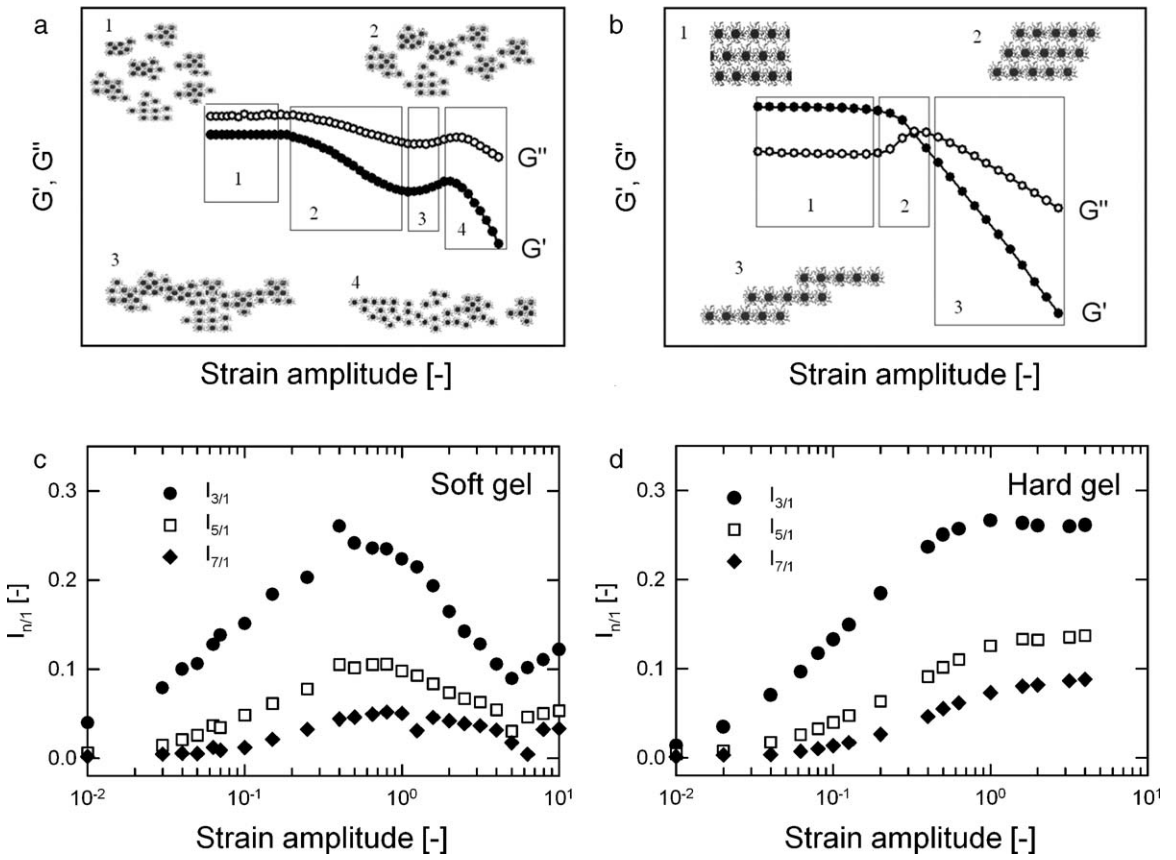

Fig. 34. (a) LAOS pattern (type I + type IV) of a soft gel at 25 °C and microstructural interpretation: (1) clusters of micelles in the solution, (2) strain thinning (type I) due to the alignment of clusters with flow direction, (3) strong strain overshoot (type IV) due to the formation of larger clusters, (4) second strain thinning due to the break up or alignment with flow direction. (b) LAOS pattern (type III) of a hard gel and corresponding microstructural interpretation: (1) close-packed (cubic) array of micelles, (2) weak strain overshoot due to the break up of structures, (3) strain thinning due to layers sliding past each other in the flow direction. Fourier spectra as a function of strain amplitude: (c) soft gel (24 °C), (d) hard gel (26 °C). Reproduced by permission of Hyun et al. [6], copyright (2006) of Springer.

The FT spectra for the hard gel and soft gel states were also compared. The LAOS measurements show that the intensity of the higher harmonics (3rd, 5th, 7th) in the soft gel reached a maximum and then decreased with strain amplitude, before slightly increasing again with further increase of the strain amplitude (Fig. 34c). This result is similar to the "hump" in $I_{3/1}$ observed for carbon black filled rubber compounds in the previous section [59]. On the other hand, the higher harmonics of a hard gel increase as a function of strain amplitude before approaching an asymptote (Fig. 34d). Decreases in the intensity of the higher harmonics with increasing strain amplitude is perhaps initially unexpected, but can also be observed with the Giesekus model LAOS response in Fig. 24e and f, in which some higher harmonic components decrease in magnitude and subsequently change sign. Heymann et al. [79] have investigated highly concentrated suspensions of PMMA particles in PDMS, which show a combination of type I and type IV response like a soft gel, and also exhibited a local maximum in the intensity of the third harmonic. Kallus et al. [51] characterized rigid polymer dispersions by FT-Rheology, and also found a local maximum in the Fourier intensities as a function of strain amplitude. By analogy, we may infer that the micellar aggregates in the soft gel behave like the rigid particles studied in [51]. However, the subsequent increase in the intensities after the local minimum shown in Fig. 34c has not been reported previously. It seems to be related to the alignment and rupture of large aggregates at very high strain amplitudes. From the experimental results shown in Fig. 34, it is clear that the flow-aligned microstructure of a soft gel and hard gel can be clearly distinguished by LAOS experiments.

5.3.3. *Biopolymer gel*

LAOS characterization is also useful for probing the nonlinear rheological properties of biopolymer gels that are critical for the successful locomotion of gastropods. Snails and slugs utilize a rheologically complex fluid, called pedal mucus, as part of their locomotory strategy in order to adhere to and climb upon vertical surfaces [151]. This biopolymer gel acts as a yield stress fluid, in which the local magnitude of the applied stress reversibly transforms the mucus between an apparently solid and liquid state [151].

Natural pedal mucus (the excreted slime trail) was collected from the slug *Limax maximus*. Similar analysis has been previously discussed in [69,152], and the

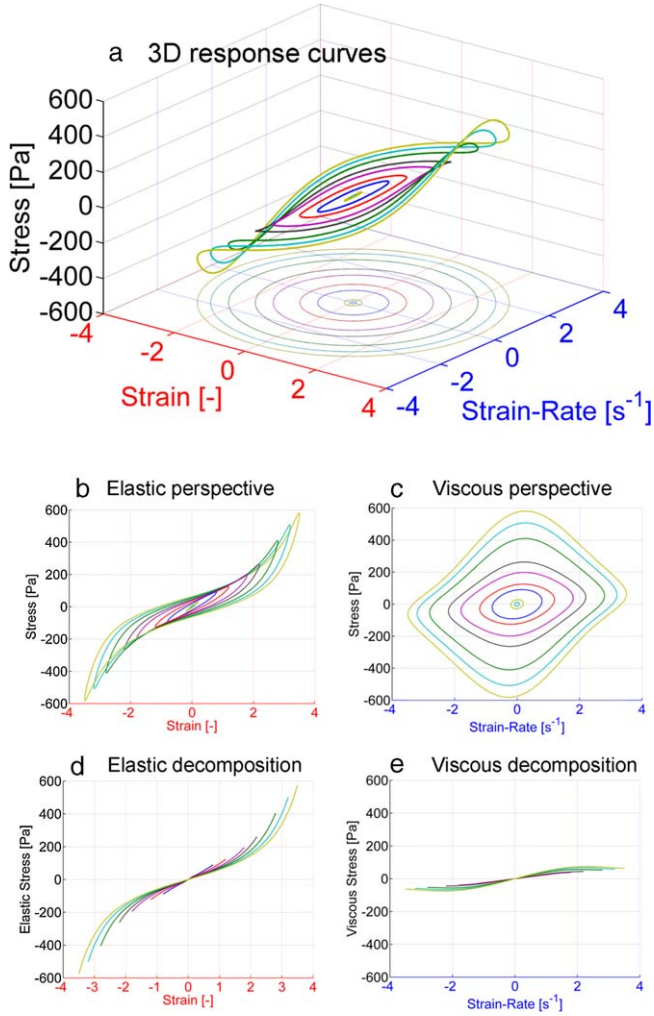

Fig. 35. Strain-controlled LAOS response of natural pedal mucus from the slug *Limax maximus* at $\omega = 1$ rad/s. (a) steady state 3D response curves showing measured stress as a function of the orthogonal oscillatory inputs of strain and strain-rate, i.e. $\sigma[\gamma(t), \dot{\gamma}(t)]$. The closed 3D curves shown in (a) can be projected onto planes which emphasize an elastic interpretation (b), or a viscous interpretation (c). The response can be decomposed into the components of elastic stress $\sigma'(\gamma)$ as shown in (d), or the viscous stress contribution $\sigma''(\dot{\gamma})$ as shown in (e). The ordinate scale in (e) is deliberately chosen to be the same as in part (d), emphasizing the dominant elastic response in the mucus.

same sample preparation and data acquisition protocols are used for the results presented here. The nonlinear behavior of these physically-crosslinked hydrogels is revealed by considering the distorted stress waveforms in the deformation-domain (Lissajous curves) and quantifying the higher harmonics with Chebyshev polynomials of the first kind. Strain-controlled LAOS tests are used with increasing strain amplitude at a fixed frequency $\omega = 1$ rad/s that is characteristic of actual molluscan locomotion. Strain amplitudes up to $\gamma_0 = 3.5$ were imposed, but the sample was not fully yielded due to experimental limitations of the instrument (i.e. the maximum allowable angular displacement amplitude). Fig. 35 displays the steady state oscillatory data in the form of Lissajous curves at each strain amplitude γ_0. The closed 3D curves shown in Fig. 35a can be projected onto complementary 2D planes. The elastic perspective results from projection onto the plane of stress $\sigma(t)$ vs. strain $\gamma(t)$, shown in Fig. 35b. In such a projection, a purely elastic response would be a single-valued function $\sigma(\gamma)$. By contrast, the Lissajous figure for the pedal mucus sample encloses a finite area on this plot, and thus viscous dissipation is also evident. The corresponding viscous perspective of the LAOS response is shown in Fig. 35c, in which the response curves are projected onto the plane of stress $\sigma(t)$ vs. strain-rate $\dot{\gamma}(t)$.

The tools of stress decomposition can be applied to this data set to decompose the total stress into a superposition of elastic and viscous stresses, according to $\sigma(t) = \sigma'(\gamma) + \sigma''(\dot{\gamma})$ (Section 4.3). The decomposed stresses are shown in Fig. 35d and e, in which these component stresses are single-valued functions within their respective 2D projections. It is the non-constant slope of these component elastic and viscous stresses which immediately indicate the nature of the intra-cycle viscoelastic nonlinearities. For this pedal mucus sample, the elastic stresses are initially linear but develop a convexity as the strain amplitude

increases. In this case the curves of elastic stress display intra-cycle strain stiffening. Similarly, the concavity of the viscous stress $\sigma''(\dot{\gamma})$ reveals the viscous nonlinearity, and in this case shear-thinning within a steady state oscillation is observed.

The leading order elastic and viscous nonlinearities are quantified by the third-order Chebyshev coefficients $e_3 = -G'_3$ and $v_3 = G''_3/\omega$, as described in Section 4.4. In Fig. 36 we display the $n = 1, 3, 5$ coefficients for both the elastic and viscous stress decompositions. Each of the third-harmonic contributions, e_3 and v_3, initially appear with a dependence on γ_0^2, which is expected from the integral expansion of the Boltzmann superposition principle [153], and is furthermore consistent with the observed behavior of the Q-parameter (Section 4.1.1), which effectively lumps together the contributions of both e_3 and v_3 (Section 4.4). It is the sign of the third-order Chebyshev coefficients which allows interpretation of the leading order nonlinearity. Fig. 36 is a log–log plot, and the sign of each data point is indicated by a filled symbol (positive value) or open symbol (negative value). For all strain-amplitudes, and for torque contributions above the critical noise threshold, it is found that $e_3 > 0$ and $v_3 < 0$. These results correspond to intra-cycle elastic strain-stiffening and viscous shear-thinning, and this quantitative analysis is consistent with the visual analysis and interpretation of the decomposed elastic and viscous stress shown in Fig. 35d and e.

The intra-cycle stiffening likely results from polymeric components within the pedal mucus gel which exhibit stretch-stiffening. However, the structure of the polymeric mucus gel must be more complicated than affine stretching of polymeric components to account for the distinct behavior revealed by the minimum-strain elastic modulus, $G'_M \equiv d\sigma'/d\gamma|_{\gamma=0}$, which decreases as a function of the imposed strain amplitude γ_0. The LAOS decoupling of simultaneous overall softening with local stiffening was also reported recently for a filled elastomer system [154]. Such physical insight may be able to inform constitutive models of this and other materials tested with LAOS, as recently demonstrated with nonlinear constitutive models to capture the biomechanics of hagfish gel [155] and gluten dough networks [156].

6. Microstructural probes under LAOS flow

Substantial efforts have been made to correlate the measured relationship between the nonlinear mechanical response in LAOS and the underlying microstructural orientation or molecular topology of the viscoelastic material. The macroscopic behavior of any complex fluid depends strongly on its microscopic structural state, thus an intimate relationship exists between rheological properties and microscopic structure. As an example, for flexible polymer chains under shear, orientational anisotropy is the structural origin of the shear-thinning in the macroscopic stress and the thermal motion of the chains which erases this anisotropy results in stress relaxation properties [157]. Consequently, quantitative prediction of both molecular scale structure and macroscopic flow properties in realistic flow fields is a central goal of research in complex fluids [158].

However, purely rheological methods provide only macroscopic measurements (e.g. the total measured torque or normal force response). This means that macroscopic rheological techniques can only be used to determine continuum-level averaged material functions, in which case any information regarding microscopic or molecular structure is inherently indirect. Simultaneous determination of additional information on the microstructure or even molecular level structure is often needed for a deeper understanding of rheological behavior. Thus, several methods have been developed to cross this bridge with respect to the length scales involved. One example is the simultaneous measurement of rheological and optical properties, e.g. via optical microscopy, light scattering or measurement of birefringence and dichroism. Rheo-optics has been widely utilized in combined rheological and microstructural investigation of various materials [159,160]. Several companies have introduced various rheo-optical tools, for example, optical microscopes (Thermo Fisher Scientific Inc.: HAAKE RheoScope rheometer; Anton Paar: Physica MCR rheometer; Malvern Instruments: Bohlin rheometer), flow-birefringence measurement (TA instruments: ARES), and small angle light scattering (SALS) (Anton Paar: Physica MCR rheometer).

There have also been numerous investigations designed to investigate microscopic or molecular scale morphology under various flow conditions with various optical tools, e.g. SALS, SANS (small-angle neutron scattering), SAXS (small-angle X-ray scattering), flow-induced birefringence (FIB) etc. For example, Safinya et al. [161] investigated the nematic to smectic-A phase transition of a liquid crystal (LC) under shear flow with synchrotron X-rays. Bent et al. [158] investigated the flow field of an entangled polymer melt through a planar contraction, typical of many polymer processes, by using both optical imaging and SANS. Dootz et al. [162] demonstrated shear-induced alignment within microchannels by utilizing *in situ* SAXS measurements. Block copolymer melts and solutions have also been investigated in great detail using LAOS. For example, Chen et al. [163] studied the flow alignment of a diblock copolymer melt under LAOS flow with *in situ* birefringence measurements and *ex situ* SAXS measurements. Wiesner [164] reviewed the effects of LAOS deformation (as a function of both frequency and strain amplitude) on the orientation behavior of lamellar structures of block copolymers with *ex situ* SAXS measurements. Hamley and coworkers [165,166] have examined the effect of flow fields on the orientation of block copolymer nanostructures in both melt and solution with *in situ* SANS and SAXS measurement. Tapadia et al. [78] reported shear banding with an entangled polymer fluid under LAOS flow at various frequency and strain amplitude using a particle-tracking velocimetry method. In addition to the above examples, there have been many other studies conducted to investigate the effect of flow on the microscopic or molecular scale structure using a variety of optical and scattering tools.

For rheo-optical methods to be applied, the material must be (at least partially) transparent at the interrogation wavelengths being utilized. More importantly, the rheo-optical measurement usually detects just an isochronal average of the material microstructure, and molecular

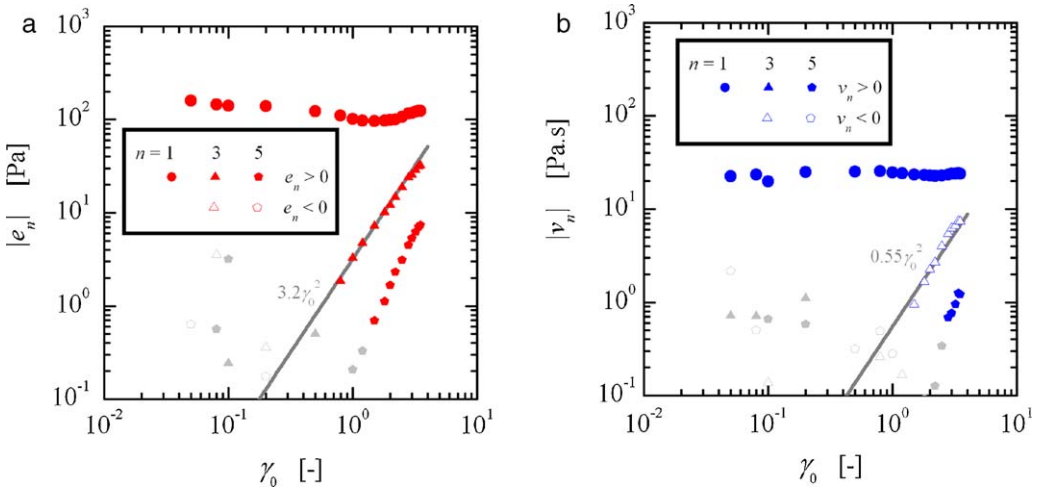

Fig. 36. Chebyshev analysis (Section 4.4) applied to the measured data shown in Fig. 35. (a) Elastic Chebyshev coefficients, and (b) Viscous Chebyshev coefficients. The sign of the third-order coefficients reveals a physical interpretation of the leading order nonlinearities, here $e_3 > 0$ indicates elastic strain-stiffening and $v_3 < 0$ reveals viscous shear-thinning. Symbols in light gray indicate data points which are below a critical torque measurement threshold, $T_{min} = 0.1\ \mu N\,m$.

motion is observed as a time-dependent change of this average [167]. Furthermore there are constraints with respect to the size of the observed objects. A detailed review of all these studies is beyond this review article. Therefore, in this section, we introduce and focus on two different *in situ* combination setups, i.e. the rheo-dielectric setup and the rheo-SAXS setup in order to illustrate the effect of LAOS deformation on the sample microstructure.

6.1. Rheo-dielectric setup

As a complementary method to rheo-optical techniques, the rheo-dielectric combination is applicable to any material having permanent electrical dipoles or charge-induced electrical dipoles. Rheo-dielectric setups allow for simultaneous measurements of dielectric and viscoelastic properties of a sample subjected to external electric and deformation fields [167], and have been used to study liquid crystals [168–170], the dynamics of polyisoprene chains [167,171,172], block-copolymers [171], carbon nanotube networks dispersed within polymer melts [173] and carbon black suspensions [174]. This method has also been extended to the nonlinear regime under LAOS deformations [83,168,175].

The dielectric property reflects the orientational correlation of two segments at two separate times (e.g. $t_0 = 0$ and $t_1 = \tau$) and can be converted to provide measures of the motion and fluctuations of the dipolar constituents with respect to the molecular axis. The chain conformations and local motions are differently averaged in the viscoelastic and dielectric properties [176]; thus, the combination of rheological and dielectric property measurements provides distinct information compared to mechanical measurements alone. This includes detailed information about the relationship between local molecular relaxation dynamics and the corresponding macroscopic rheological response, as well as insight into the evolution of molecular conformation, specifically stretch and orientation. In addition to polymer chain dynamics, the rheo-dielectric combination can be used to investigate shear-induced changes in various materials, e.g. in block copolymers or liquid crystals under shear.

A polymer chain is called type-A if it has monomer dipoles oriented parallel along the chain backbone [177]. Therefore, for type-A polymers the overall electric dipole of the molecule is directly related to the end-to-end vector orientation and its fluctuations. Consequently the spectra reflect the global chain motion [178]. These specific dielectric features of type-A chains have been successfully utilized in recent studies to reveal interesting equilibrium and non-equilibrium dynamics of linear and branched polymer chains [167,171,172]. Furthermore, the *in situ* combination of dielectric and mechanical methods reveals quite novel dynamic features [171]. Watanabe et al. [167,172,176] have studied polymer chain dynamics under steady shear in this way. They analyzed their rheo-dielectric and viscoelastic data for entangled PI melts within the molecular picture of convective constraint release (CCR) induced by dynamic tube dilation (DTD). The rheo-dielectric method also allows the investigation of global chain dynamics under LAOS flow. The effect of LAOS on the dielectric response of 1,4-cis-polyisoprene as a type-A polymer has been studied in some detail [83,168,175]. For the rheo-dielectric experiments, a new setup was built using a combination of the ARES-Rheometer (TA Instruments) and a very sensitive dielectric analyzer (Alpha analyzer from Novocontrol Technologies) [83,175].

Rheological measurements were carried out on a strain controlled rheometer using a modified parallel plate fixture and oven (Fig. 37). FT-Rheology was conducted as described in Section 4.1 and a separate PC was used to control the Alpha-analyzer. Fig. 37a shows the experimental setup of the combination of a rheometer and a dielectric analyzer *in situ*. To realize this rheo-dielectric setup with a conventional rheometer, a new measuring plate and fixture had to be designed and constructed and some parts of the

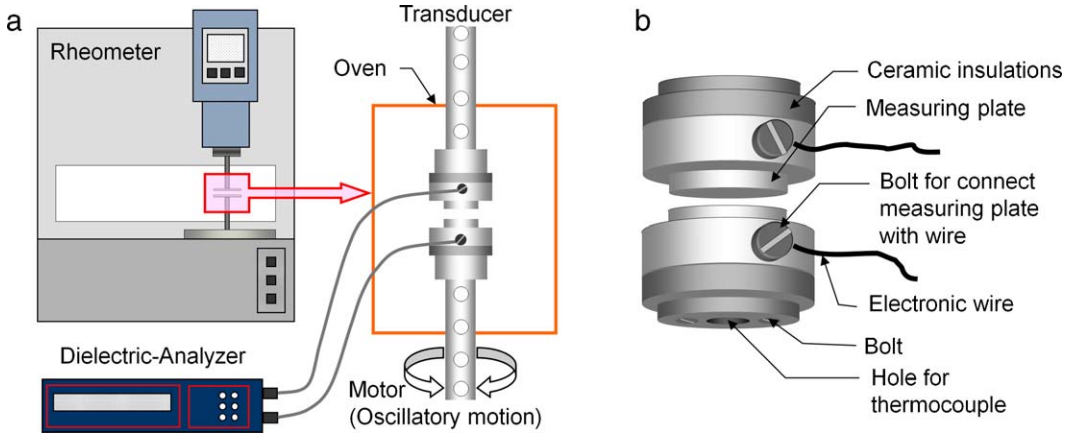

Fig. 37. (a) Experimental setup for the *in situ* combination of rheometry and dielectric spectroscopy. (b) Schematic 3D view of the measurement geometry, which consists of parallel electrode plate, ceramic insulation, and bolts for connecting the measuring plate with the electronics. Reproduced by permission of Hyun et al. [175], copyright (2009) of Elsevier.

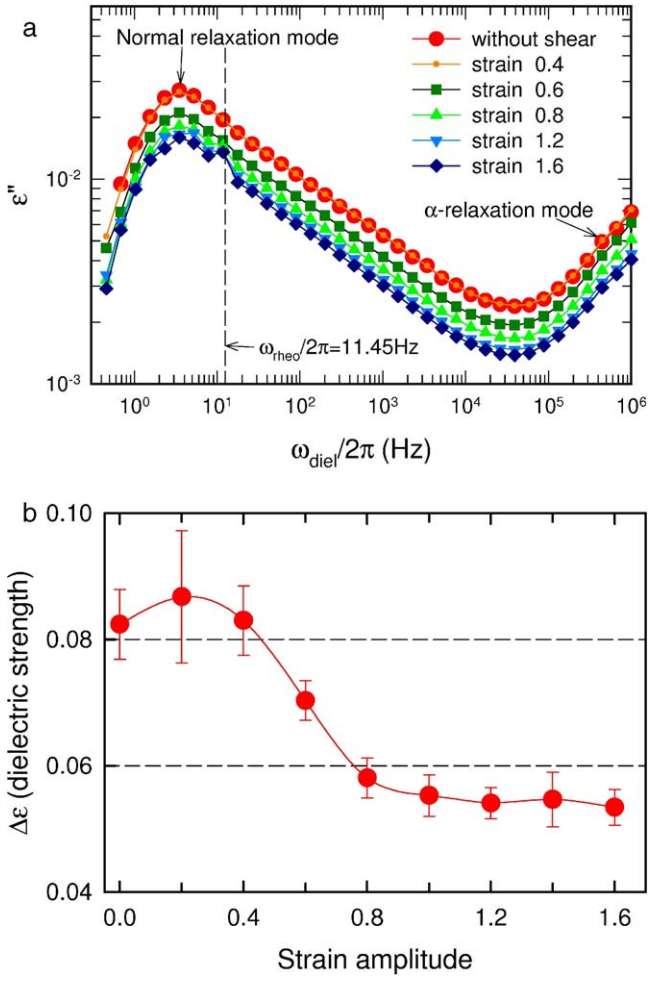

Fig. 38. (a) The dielectric loss ε'' as a function of dielectric frequency under LAOS with PI 55K at 10 °C. The LAOS tests were carried out at a rheological test frequency $\omega_{rheo}/2\pi = 11.45$ Hz. (b) The dielectric strength as a function of strain amplitude is divided into three regions for the PI 55K, an initially constant value ($0 < \gamma_0 < 0.4$), decreasing ($0.4 < \gamma_0 < 1$), and asymptotic plateau at high strains ($\gamma_0 > 1$). Reproduced by permission of Hyun et al. [175], copyright (2009) of Elsevier.

oven were also modified (see Fig. 37b). Fig. 38a displays the dielectric spectra as a function of $\omega_{diel}/2\pi$ under LAOS with different strain amplitudes for a PI sample (M_w = 55K) at 10 °C. The intensity decreases with increasing strain amplitude, but the peak position and shape of the curve remain unchanged. This means that LAOS affects neither the mean relaxation time nor the relaxation time distributions of the normal mode process. Fig. 38b shows the dielectric strength ($\Delta\varepsilon$) as a function of strain amplitude. It was observed that $\Delta\varepsilon$ shows significant changes as the shear strain amplitude is increased. At small or medium strain amplitude (γ_0 = 0.2 and 0.4) the dilectric strength $\Delta\varepsilon$ remains unchanged from the value observed under no-flow conditions; however, for strain amplitude between γ_0 = 0.4 and γ_0 = 1, it decreases rapidly before leveling off and approaching an almost constant asymptote for strain amplitudes γ_0 > 1.

6.2. In situ Rheo-SAXS setup

The combination of rheometry and X-ray scattering allows investigation of the effect of macroscopic shear on molecular ordering at the nanometer scale. Since this question is of general interest, there have been many *in situ* rheo-SAXS experiments using a range of test geometries, including Couette cells [106,161,179–181], a toothed geometry [182,183], annular cone and plate [184], a conventional plate-plate geometry by reflecting X-ray beam [185,186], and others [107,187]. These *in situ* Rheo-SAXS setups offer great potential for investigating the shear-induced changes in the microstructure of various complex fluids under nonlinear oscillatory shear flow. The advent of very bright x-ray sources will enable development of time-resolved experiments that provide a large amount of new information regarding non-equilibrium chain dynamics and evolution in orientation and shape of micro- or nano-structure during nonlinear oscillatory shear flow. *An in situ* Rheo-SAXS setup can directly correlate this structural information with changes in the nonlinear coefficients obtained from LAOS, e.g. the ratio $I_{3/1}$ calculated from FT-rheology.

7. Concluding remarks

In this article we have reviewed the current status of large amplitude oscillatory shear (LAOS) rheological measurements. The primary focus has been with respect to strain-controlled shear tests and measurement of the oscillating nonlinear shear stress and first normal stress difference for a wide range of complex fluids, with a primary focus on polymeric systems. LAOS tests are substantially more complex rheological probes than small amplitude oscillatory shear (SAOS) tests because of the non-sinusoidal and nonlinear system response. The complexity of the material response to LAOS is both the strength and weakness of the technique. The additional information obtained can help characterize the response of complex fluids to nonlinear deformation, but it also makes the results more difficult to interpret.

Recent hardware and software advances have contributed to impressive advances in quantitative analysis of LAOS measurements. These quantitative techniques enable systematic investigation of nonlinear responses under large amplitude deformation; consequently, LAOS is becoming adopted more broadly. As a result of the very recent technical implementation of high performance LAOS techniques in commercial rheometers, the spread of these techniques will be further facilitated. Recent uses of LAOS measurements, not included in this review, include fitting nonlinear parameters for constitutive models, e.g. the Giesekus model [188] and interrogating nonlinear response of dense colloidal suspensions under oscillatory shear using Mode-coupling theory and experiments [189]. Broader experimental application is also being found by modifying the LAOS ideas reviewed here. For example, recent reports have demonstrated the use of controlled *shear stress* input with analysis of the resulting nonlinear strain signal [190], and the use of large amplitude oscillatory *extension* tests [191]. Experimentally, one continuing difficulty is ensuring homogenous deformation. Recent work has shown the ability to simultaneously observe LAOS behavior while confirming homogeneous deformation [192]. LAOS responses in concert with non-homogenous deformation (shear-banding) have also been considered, e.g. for a nonlinear model for entangled wormlike micellar solutions [193].

The theoretical underpinnings of the nonlinear responses observed under LAOS flow for different complex fluids (e.g. polymer melts or solutions, dispersed systems, and blockcopolymer systems) are still poorly understood. The mechanisms that can lead to even harmonic generation in the shear stress also beg for improved theoretical understanding. Finally we also note that the use of complementary *in situ* microstructural probes, e.g. rheo-SAXS, rheo-dielectric configurations, etc., will help to more deeply connect the measured macroscopic response with the microstructural origin of nonlinear viscoelastic behavior.

List of symbols

A_l	coefficient of linear response function from characteristic function
A_r	coefficient of periodic rectangular function from characteristic function
A_t	coefficient of periodic triangular function from characteristic function
A_{st}	coefficient of periodic saw tooth function from characteristic function
a	creation rate constants in network model
a_{pq}	*in-phase* expansion coefficients at nonlinear oscillatory regime (p, q = 1, *odd*)
b	loss rate constants in network model
b_{pq}	*out-of-phase* expansion coefficients at nonlinear oscillatory regime (p, q = 1, *odd*)
C_{ij}	Taylor or polynomial expansion coefficient, i,j = 1, 2, 3, ⋯
D	the rate of deformation tensor
De	Deborah number (=ω/ω_c)
e_n	nth elastic Chebyshev coefficients (n = 1, *odd*)
$f(t)$	creation rate function in network model
$g(t)$	loss rate function in network model

G' elastic (storage) modulus in linear regime (SAOS) [Pa]
G'' viscous (loss) modulus in linear regime (SAOS) [Pa]
G'_n nonlinear elastic (storage) modulus from a Fourier series ($n = 1$, *odd*)
G''_n nonlinear viscous (loss) modulus from a Fourier series ($n = 1$, *odd*)
G'_{nm} nonlinear elastic modulus from a power series (n, $m = 1$, *odd*)
G''_{nm} nonlinear viscous modulus from a power series (n, $m = 1$, *odd*)
G'_N generalized elastic modulus
G'_{SR} sine-wave regression fit elastic modulus
G'_{LR} linear regression fit elastic modulus
G'_{PR} polynomial regression fit elastic modulus
G'_M the minimum-strain elastic modulus
G'_L the largest-strain secant elastic modulus
G'_K the largest-strain tangent elastic modulus
G^0_N plateau modulus
I_n nth harmonic intensities from FT-Rheology ($n = 1$, *odd*)
I_n/I_1 or $I_{n/1}$ relative intensities from FT-Rheology ($n = 3$, *odd*)
N_i first normal stress difference at $i = 1$ and second normal stress difference at $i = 2$
$N_{i,2k(k=0,1,2\ldots)}$ nonlinear normal stress differences $i = 1$ or 2
$Q(\gamma_0, \omega)$ nonlinear parameter from FT-Rheology
$Q_0(\omega)$ zero-strain nonlinear parameter or intrinsic nonlinear parameter from FT-Rheology
$Q1$ the first quarter cycle torque (stress) signal integration
$Q2$ the second quarter cycle torque (stress) signal integration
S/N the signal to noise ratio
t time [s]
T_n Chebyshev functions
v_n nth viscous Chebyshev coefficients

Greek letters

α the mobility factor in Giesekus model
δ phase angle at linear regime (SAOS) [rad or °]
δ_n nth phase angle from shear stress at nonlinear regime ($n = 1$, *odd*) [rad or °]
$\delta_{i,2k(k=0,1,2\ldots)}$ kth phase angle from normal stress difference $i = 1$ or 2 [rad or °]
η viscosity
η_0 zero shear viscosity
η_s solvent viscosity in Giesekus model
η_p polymer viscosity in Giesekus model
γ shear strain
γ_0 shear strain amplitude
$\dot{\gamma}$ shear rate [s^{-1}]
λ relaxation time [s]
σ or σ_{12} shear stress
$\boldsymbol{\sigma}$ stress tensor
$\overset{\nabla}{\boldsymbol{\sigma}}$ upper convected stress tensor
σ_{ij} stress tensor component, $i, j = 1, 2, 3$
$\sigma_{\max}$ maximum shear stress
σ_n nth harmonic shear stress at nonlinear regime ($n = 1$, *odd*)
σ' elastic shear stress (LAOS decomposition)
σ'' viscous shear stress (LAOS decomposition)
$\boldsymbol{\sigma_s}$ solvent stress tensor in Giesekus model
$\boldsymbol{\sigma_p}$ polymer stress tensor in Giesekus model
τ characteristic relaxation time
ω angular frequency [rad/s]
ω_c crossover angular frequency at $G' = G''$ in SAOS test [rad/s]

Acknowledgments

KH would like to thank Prof. Spiess for financial support and acknowledge support by Basic Science Research Program through the National Research Foundation of Korea (NRF) funded by the Ministry of Education, Science and Technology (no. 2010-0024466). RHE acknowledges support from the Institute for Mathematics and its Applications. MW would like to acknowledge the former and current members of his group, the cooperation partners and especially Prof. Spiess and Prof. Wegner from the Max-Planck Institute for Polymer Research in Mainz, Germany. KHA acknowledges the support by the National Research Foundation of Korea (NRF) grant (no. 0458-20090039) funded by the Korea government (MEST). GHM would like to acknowledge gifts from the Procter & Gamble Company and Schlumberger Doll Research.

Appendix A. Stress direction and deformation direction

In simple shear flow, the deformation gradient in the sample is given by $\mathbf{F} = \mathbf{I} + \gamma \mathbf{e}_1\mathbf{e}_2$ where $\mathbf{I}$ is the identity tensor, γ is the shear strain and $\mathbf{e}_i$ are the orthonormal base vectors inherent to the reference frame under consideration. Changes in the chosen coordinate system should not alter the physical phenomena that arise from the deformation. Consider a physical process that is described by two coordinate systems such that

$$\mathbf{e}'_1 = -\mathbf{e}_1, \quad \mathbf{e}'_2 = -\mathbf{e}_2, \quad \mathbf{e}'_3 = \mathbf{e}_3 \tag{A1}$$

Because of the symmetry of the simple shear flow, it follows that

$$\mathbf{F} = \mathbf{e}_i\mathbf{e}_i + \gamma\mathbf{e}_1\mathbf{e}_2 = \mathbf{e}'_i\mathbf{e}'_i + \gamma'\mathbf{e}'_1\mathbf{e}'_2, \quad \gamma = \gamma' \tag{A2}$$

In Eq. (A2), the summation convention was used. Since the stress ($\boldsymbol{\sigma}$) arising from the simple shear depends on the deformation history, the nature of the tensor and the symmetry of the simple shearing deformation lead to

$$\boldsymbol{\sigma} = \sigma_{ik}\mathbf{e}_i\mathbf{e}_k = \sigma'_{ik}\mathbf{e}'_i\mathbf{e}'_k = \sigma_{ik}\mathbf{e}'_i\mathbf{e}'_k$$

$$\sigma_{11} = \sigma'_{11}, \quad \sigma_{22} = \sigma'_{22}, \quad \sigma_{33} = \sigma'_{33}, \tag{A3}$$

$$\sigma_{12} = \sigma'_{12}, \quad \sigma_{23} = -\sigma'_{23}, \quad \sigma_{31} = -\sigma'_{31}$$

Thus, the only non-zero components of the stress tensor are the diagonal components and the off-diagonal

element σ_{12}. Hence, we have

$$\boldsymbol{\sigma} = \sigma_{11}\mathbf{e}_1\mathbf{e}_1 + \sigma_{22}\mathbf{e}_2\mathbf{e}_2 + \sigma_{33}\mathbf{e}_3\mathbf{e}_3 + \sigma_{12}(\mathbf{e}_1\mathbf{e}_2 + \mathbf{e}_2\mathbf{e}_1) \tag{A4}$$

Eq. (A4) is valid for shear flows such as those generated between rotating parallel disks, those between a rotating cone and a stationary plate and those generated in capillary rheometers. In case of oscillatory shear flow, the stress is analyzed in the steady periodic state, therefore stress can be expressed by an algebraic function of deformation rather than a functional of deformation. Hence we can write

$$\boldsymbol{\sigma} = \boldsymbol{\sigma}(\gamma, \gamma^{(1)}, \gamma^{(2)}, \ldots) \tag{A5}$$

where

$$\gamma^{(n)} = \frac{d^n\gamma}{dt^n} \tag{A6}$$

Because shear strain is given by $\gamma = \gamma_0 \sin\omega t$, we know that all time derivatives of shear strains are not independent. This allows us to write Eq. (A5) in simpler form:

$$\boldsymbol{\sigma} = \boldsymbol{\sigma}(x, y) \tag{A7}$$

where $x \equiv \gamma_0 \sin\omega t$ and $y = \gamma_0 \cos\omega t = \omega^{-1} d\gamma/dt$.

If the shear direction is changed, i.e., $x \to -x$ then we know that $y \to -y$. This change of the direction of shearing is equivalent to a change of the base vectors as follows

$$\mathbf{e}_1' = -\mathbf{e}_1, \quad \mathbf{e}_2' = \mathbf{e}_2, \quad \mathbf{e}_3' = \mathbf{e}_3 \tag{A8}$$

Eqs. (A8) and (A4) imply

$$\begin{aligned}\boldsymbol{\sigma}(-x, -y) &= \sum_{k=1}^{3}\sigma_{kk}(-x, -y)\mathbf{e}_k\mathbf{e}_k + \sigma_{12}(-x, -y)(\mathbf{e}_1\mathbf{e}_2 + \mathbf{e}_2\mathbf{e}_1)\\ &= \sum_{k=1}^{3}\sigma_{kk}(x, y)\mathbf{e}_k'\mathbf{e}_k' + \sigma_{12}(x, y)(-\mathbf{e}_1'\mathbf{e}_2' - \mathbf{e}_2'\mathbf{e}_1')\\ &= \sum_{k=1}^{3}\sigma_{kk}(x, y)\mathbf{e}_k\mathbf{e}_k - \sigma_{12}(x, y)(\mathbf{e}_1\mathbf{e}_2 + \mathbf{e}_2\mathbf{e}_1)\end{aligned} \tag{A9}$$

Finally, we note that the shear stress changes its sign according to that of the imposed deformation whereas the normal stress difference does not. Therefore, the symmetry of shear stress and normal stress difference are given as follows,

$$\sigma_{12}[-\gamma(t), -\dot{\gamma}(t)] = -\sigma_{12}[\gamma(t), \dot{\gamma}(t)] \tag{A10}$$

$$N_{1,2}[\gamma(t), \dot{\gamma}(t)] = N_{1,2}[-\gamma(t), -\dot{\gamma}(t)] \tag{A11}$$

where $N_{1,2}$ = first and second normal stress differences, respectively.

Appendix B. Odd harmonics of shear stress in oscillatory shear

$$\sigma(t) = \sum_{i=0}\sum_{j=0} C_{ij}\gamma^i(t)\dot{\gamma}^j(t) \tag{B1}$$

From Appendix A, the shear stress must be an odd function of the direction of shearing deformations.

$$\sigma[-\gamma(t), -\dot{\gamma}(t)] = -\sigma[\gamma(t), \dot{\gamma}(t)] \tag{B2}$$

$$\begin{aligned}\sigma(t) = \sum_{i=1}\sum_{j=1}&[C_{2i-1,2(j-1)}\gamma^{2i-1}(t)\dot{\gamma}^{2(j-1)}(t)\\ &+ C_{2(i-1),2j-1}\gamma^{2(i-1)}(t)\dot{\gamma}^{2j-1}(t)]\end{aligned} \tag{B3}$$

Applying an oscillatory shear flow, the strain and strain-rate can be described as follows

$$\gamma(t) = \gamma_0 \sin\omega t, \quad \dot{\gamma}(t) = \omega\gamma_0 \cos\omega t \tag{B4}$$

Inserting Eq. (B4) into Eq. (B3) results in the following expression for the shear stress:

$$\gamma^{2i-1}\dot{\gamma}^{2(j-1)} = \gamma_0^{2i+2j-3}\omega^{2(j-1)} \sin^{2i-1}\omega t \cos^{2(j-1)}\omega t$$

$$\gamma^{2(i-1)}\dot{\gamma}^{2j-1} = \gamma_0^{2i+2j-3}\omega^{2j-1} \sin^{2(i-1)}\omega t \cos^{2j-1}\omega t \tag{B5}$$

$$\begin{aligned}\sigma(t) = \sum_{i=1}\sum_{j=1}\gamma_0^{2i+2j-3}\omega^{2j-1}&\left[\frac{C_{2i-1,2(j-1)}}{\omega} \sin^{2i-1}\right.\\ &\left.\omega t \cos^{2(j-1)}\omega t + C_{2(i-1),2j-1} \sin^{2(i-1)}\omega t \cos^{2j-1}\omega t\right]\end{aligned} \tag{B6}$$

Sine and cosine functions are expressed as follows:

$$\cos^{2j-1}\omega t = \sum_{n=1}^{j} a_n \cos(2n-1)\omega t,$$

$$\sin^{2j-1}\omega t = \sum_{n=1}^{j} b_n \sin(2n-1)\omega t \tag{B7}$$

$$\sin^{2j}\omega t = \sum_{n=0}^{j} c_n \cos 2n\omega t, \quad \cos^{2j}\omega t = \sum_{n=0}^{j} d_n \cos 2n\omega t \tag{B8}$$

From the above equation,

$$\sin^{2i-1}\omega t \cos^{2(j-1)}\omega t = \left(\sum_{n=1}^{i} c_n \sin(2n-1)\omega t\right)$$

$$\left(\sum_{m=1}^{j} d_m \cos 2(m-1)\omega t\right) = \sum_{n=1}^{i}\sum_{m=1}^{j} c_n d_m \sin(2n-1)\omega t$$

$$\cos 2(m-1)\omega t = \sum_{n=1}^{i}\sum_{m=1}^{j}\frac{c_n d_m}{2}[\sin(2n+2m-3)\omega t$$

$$+ \sin(2n-2m+1)\omega t] = \sum_{m=1,odd}^{2i+2j-3} a_m \sin m\omega t \tag{B9}$$

$$\sin^{2i-2}\,\omega t\,\cos^{2j-1}\,\omega t = \left(\sum_{n=1}^{i} e_n \cos 2(n-1)\omega t\right)$$

$$\left(\sum_{m=1}^{j} f_m \cos(2m-1)\omega t\right) = \sum_{n=1}^{i}\sum_{m=1}^{j} e_n f_m \cos 2(n-1)\omega t$$

$$\cos(2m-1)\omega t = \sum_{n=1}^{i}\sum_{m=1}^{j}\frac{e_n f_m}{2}[\cos(2n+2m-3)\omega t + \cos(2n-2m-1)\omega t] = \sum_{n=1,odd}^{2i+2j-3} b_n \cos n\omega t \tag{B10}$$

Inserting Eq. (B9) and Eq. (B10) into the equation for stress given in Eq. (B6) results in the following expression for the stress:

$$\sigma(t) = \sum_{i=1}\sum_{j=1}\gamma_0^{2i+2j-3}\omega^{2j-1}\left[\frac{C_{2i-1,2(j-1)}}{\omega}\sum_{m=1,odd}^{2i+2j-3} a_m \sin m\omega t + C_{2(i-1),2j-1}\sum_{n=1,odd}^{2i+2j-3} b_n \cos n\omega t\right] \tag{B11}$$

Therefore, we simply summarized the shear stress with the *odd* higher-order terms in the nonlinear regime as follows:

$$\sigma(t) = \sum_{p,odd}\sum_{q,odd}^{p}\gamma_0^q[a_{pq}\sin q\omega t + b_{pq}\cos q\omega t] \tag{B12}$$

Appendix C. Giesekus and UCM model

Giesekus attempted to derive a theory for concentrated solutions or melts by starting from the simple dumbbell theory for dilute solutions [123]. The Giesekus model is given by

$$\overset{\nabla}{\boldsymbol{\sigma}} + \frac{1}{\lambda}\boldsymbol{\sigma} + \alpha\frac{1}{\lambda G}\boldsymbol{\sigma}\cdot\boldsymbol{\sigma} = 2G\mathbf{D} \quad \text{or} \quad \boldsymbol{\sigma} + \lambda\overset{\nabla}{\boldsymbol{\sigma}} + \alpha\frac{\lambda}{\eta}\boldsymbol{\sigma}\cdot\boldsymbol{\sigma} = 2\eta\mathbf{D} \tag{C1}$$

where λ is the relaxation time, G is the modulus, η is the viscosity ($\lambda = \eta/G$) and the superscript ∇ denotes the upper convective time derivative, which is defined as follows:

$$\overset{\nabla}{\boldsymbol{\sigma}} = \frac{\partial}{\partial t}\boldsymbol{\sigma} + v\cdot\nabla\boldsymbol{\sigma} - (\nabla v)^T\cdot\boldsymbol{\sigma} - \boldsymbol{\sigma}\cdot\nabla v \tag{C2}$$

where $\boldsymbol{\sigma}$ is the stress tensor, ∇v is the velocity gradient and $\mathbf{D}$ is the rate of deformation tensor. The parameter α is the "mobility factor" which can be associated with anisotropic Brownian motion and/or anisotropic hydrodynamic drag [2]. Maximum and minimum anisotropy correspond to $\alpha = 1$ and $\alpha = 0$, respectively. If α exceeds unity, the stress keeps on growing rather than relaxing when deformation ceases. When $\alpha = 0$ (isotropic drag), the upper-convected Maxwell (**UCM**) equation is recovered [123].

$$\overset{\nabla}{\boldsymbol{\sigma}} + \frac{1}{\lambda}\boldsymbol{\sigma} = 2G\mathbf{D} \quad \text{or} \quad \boldsymbol{\sigma} + \lambda\overset{\nabla}{\boldsymbol{\sigma}} = 2\eta\mathbf{D} \tag{C3}$$

Appendix D. Q_0 at low frequency

Pearson and Rochefort [20] calculated the nonlinear coefficients using the Doi-Edwards model for entangled polymer systems:

$$G'_{11}(\omega) = \frac{3}{5}\frac{\rho kT}{N_e}\sum_{p,odd}^{\infty}\frac{8}{\pi^2 p^2}\frac{\omega^2\tau_d^2}{p^4+\omega^2\tau_d^2} \tag{D1}$$

$$G''_{11}(\omega) = \frac{3}{5}\frac{\rho kT}{N_e}\sum_{p,odd}^{\infty}\frac{8}{\pi^2}\frac{\omega\tau_d}{p^4+\omega^2\tau_d^2} \tag{D2}$$

$$G'_{33}(\omega) = \frac{3}{28}\frac{\rho kT}{N_e}\sum_{p,odd}^{\infty}\frac{8}{\pi^2 p^2}\left(\frac{\omega^2\tau_d^2}{p^4+\omega^2\tau_d^2} - \frac{4\omega^2\tau_d^2}{p^4+4\omega^2\tau_d^2} + \frac{3\omega^2\tau_d^2}{p^4+9\omega^2\tau_d^2}\right) \tag{D3}$$

$$G''_{33}(\omega) = \frac{3}{28}\frac{\rho kT}{N_e}\sum_{p,odd}^{\infty}\frac{8}{\pi^2}\left(\frac{\omega\tau_d}{p^4+\omega^2\tau_d^2} - \frac{2\omega\tau_d}{p^4+4\omega^2\tau_d^2} + \frac{\omega\tau_d}{p^4+9\omega^2\tau_d^2}\right) \tag{D4}$$

The low-frequency limits of the dynamic moduli are

$$G'_{11}(\omega) \cong \frac{3}{5}\frac{\rho kT}{N_e}\sum_{p,odd}^{\infty}\frac{8}{\pi^2}\frac{\omega^2\tau_d^2}{p^6} \tag{D5}$$

$$G''_{11}(\omega) \cong \frac{3}{5}\frac{\rho kT}{N_e}\sum_{p,odd}^{\infty}\frac{8}{\pi^2}\frac{\omega\tau_d}{p^4} \tag{D6}$$

$$G'_{33}(\omega) \cong \frac{3}{28}\frac{\rho kT}{N_e}\sum_{p,odd}^{\infty}\frac{8}{\pi^2}\frac{-12\omega^4\tau_d^4}{p^{10}} \tag{D7}$$

$$G''_{33}(\omega) \cong \frac{3}{28}\frac{\rho kT}{N_e}\sum_{p,odd}^{\infty}\frac{8}{\pi^2}\frac{-2\omega^3\tau_d^3}{p^8} \tag{D8}$$

Using the definition of the nonlinear coefficient Q_0 from Eq. (31), the limiting response at low frequencies for the Doi-Edwards model is given as follows,

$$\lim_{\omega\to 0} Q_0(\omega) = \lim_{\omega\to 0}\frac{\sqrt{{G'_{33}}^2 + {G''_{33}}^2}}{\sqrt{{G'_{11}}^2 + {G''_{11}}^2}} \propto \lim_{\omega\to 0}\frac{\sqrt{\omega^8+\omega^6}}{\sqrt{\omega^4+\omega^2}} \propto \lim_{\omega\to 0}\frac{\omega^3}{\omega} \propto \omega^2 \tag{D9}$$

Therefore, a quadratic scaling ($Q_0 \propto \omega^2$) in the low-frequency limit can be assumed for the nonlinear coefficient $Q_0(\omega)$. For the specific case of the Doi-Edwards mode using standard formulae for summation of the individual terms in Eqs. (D5)–(D8), we find:

$$\lim_{\omega\to 0} Q_0(\omega) \to \frac{1}{3}(\tau_d\omega)^2 \tag{D10}$$

which is in good agreement with Fig. 12b of Hyun and Wilhelm [43].

References

[1] Ferry JD. Viscoelastic properties of polymers. New York: Wiley; 1980.
[2] Bird RB, Armstrong RC, Hassager O. Dynamics of polymeric liquids, vol. 1. New York: Wiley; 1987.
[3] Tschoegl NW. The phenomenological theory of linear viscoelastic behavior: an introduction. New York: Springer-Verlag; 1989.
[4] Dealy JM, Wissbrun KF. Melt rheology and its role in plastics processing: theory and applications. New York: VNR; 1990.
[5] Klein OC, Spiess HW, Calin A, Balan C, Wilhelm M. Separation of the nonlinear oscillatory response into a superposition of linear, strain hardening, strain softening, and wall slip response. Macromolecules 2007;40:4250–9.
[6] Hyun K, Nam JG, Wilhelm M, Ahn KH, Lee SJ. Large amplitude oscillatory shear behavior of PEO–PPO–PEO triblock copolymer solutions. Rheol Acta 2006;45:239–49.
[7] Yosick JA, Giacomin AJ, Moldenaers P. A kinetic network model for nonlinear flow behavior of molten plastics in both shear and extension. J Non-Newtonian Fluid Mech 1997;70:103–23.
[8] Giacomin AJ, Dealy JM. Large-amplitude oscillatory shear. In: Collyer AA, editor. Techniques in rheological measurements. London: Chapman & Hall; 1993. p. 99–121.
[9] Payne AR. The dynamic properties of carbon black-loaded natural rubber vulcanizates. Part I. J Appl Polym Sci 1962;6:57–63.
[10] Fletcher WP, Gent AN. Non-linearity in the dynamic properties of vulcanized rubber compounds. Trans Inst Rubber Ind 1953;29:266–80.
[11] Harris J. Response of time-dependent materials to oscillatory motion. Nature 1965;207:744.
[12] Philippoff W. Vibrational measurements with large amplitudes. Trans Soc Rheol 1966;10:317–34.
[13] MacDonald IF, Marsh BD, Ashare E. Rheological behavior for large amplitude oscillatory shear motion. Chem Eng Sci 1969;24:1615–25.
[14] Onogi S, Masuda T, Matsumoto T. Nonlinear behavior of viscoelastic materials. I. Disperse systems of polystyrene solution and carbon black. Trans Soc Rheol 1970;14:275–94.
[15] Dodge JS, Krieger IM. Oscillatory shear of nonlinear fluids. I. Preliminary investigation. Trans Soc Rheol 1971;15:589–601.
[16] Matsumoto T, Segawa Y, Warashina Y, Onogi S. Nonlinear behavior of viscoelastic materials. II. The method of analysis and temperature dependence of nonlinear viscoelastic functions. Trans Soc Rheol 1973;17:47–62.
[17] Komatsu H, Mitsui T, Onogi S. Nonlinear viscoelastic properties of semisolid emulsions. Trans Soc Rheol 1973;17:351–64.
[18] Tee TT, Dealy JM. Nonlinear viscoelasticity of polymer melts. J Rheol 1975;19:595–615.
[19] Walters K, Jones TER. Further studies on the usefulness of the Weissenberg rheogoniometer. In: Onogi S, editor. Proceedings of the 5th int cong rheol, vol. 4. Tokyo: University of Tokyo Press; 1970. p. 337–50.
[20] Pearson DS, Rochefort WE. Behavior of concentrated polystyrene solutions in large-amplitude oscillating shear fields. J Polym Sci Polym Phys Ed 1982;20:83–98.
[21] Helfand E, Pearson DS. Calculation of the nonlinear stress of polymers in oscillatory shear fields. J Polym Sci Polym Phys Ed 1982;20:1249–58.
[22] Hatzikiriakos SG, Dealy JM. Wall slip of molten high density polyethylene. I. Sliding plate rheometer studies. J Rheol 1991;35:497–523.
[23] Adrian DW, Giacomin AJ. The quasi-periodic nature of a polyurethane melt in oscillatory shear. J Rheol 1992;36:1227–43.
[24] Giacomin AJ, Jeyaseelan RS, Samurkas T, Dealy JM. Validity of separable BKZ model for large amplitude oscillatory shear. J Rheol 1993;37:811–26.
[25] Adrian DW, Giacomin AJ. The transition to quasi-periodicity for molten plastics in large amplitude oscillatory shear. J Eng Mater Technol 1994;116:446–50.
[26] Giacomin AJ, Oakley JG. Structural network models for molten plastics evaluated in large-amplitude oscillatory shear. J Rheol 1992;36:1529–46.
[27] Jeyaseelan RS, Giacomin AJ. Best fit for differential constitutive model parameters to nonlinear oscillation data. J Non-Newtonian Fluid Mech 1993;47:267–80.
[28] Dealy JM, Jeyaseelan RS. Frequency response of a shear stress transducer installed in a sliding plate rheometer. J Rheol 1998;42:833–41.
[29] Boukany PE, Wang SQ. A correlation between velocity profile and molecular weight distribution in sheared entangled polymer solutions. J Rheol 2007;51:217–33.
[30] Wilhelm M, Maring D, Spiess HW. Fourier-transform rheology. Rheol Acta 1998;37:399–405.
[31] Wilhelm M, Reinheimer P, Ortseifer M. High sensitivity Fourier-transform rheology. Rheol Acta 1999;38:349–56.
[32] Wilhelm M, Reinheimer P, Ortseifer M, Neidhöfer T, Spiess HW. The crossover between linear and nonlinear mechanical behaviour in polymer solutions as detected by Fourier-transform rheology. Rheol Acta 2000;39:241–7.
[33] Wilhelm M. Fourier-transform rheology. Macromol Mater Eng 2002;287:83–105.
[34] Dusschoten DV, Wilhelm M. Increased torque transducer sensitivity via oversampling. Rheol Acta 2001;40:395–9.
[35] Neidhöfer T, Wilhelm M, Spiess HW. Fourier-transform rheology on linear polystyrene melts. Appl Rheol 2001;11:126–33.
[36] Fleury G, Schlatter G, Muller R. Non linear rheology for long chain branching characterization, comparison of two methodologies: Fourier transform rheology and relaxation. Rheol Acta 2004;44:174–87.
[37] Schlatter G, Fleury G, Muller R. Fourier transform rheology of branched polyethylene: experiments and models for assessing the macromolecular architecture. Macromolecules 2005;38:6492–503.
[38] Sugimoto M, Suzuki Y, Hyun K, Ahn KH, Ushioda T, Nishioka A, Taniguchi T, Koyama K. Melt rheology of long-chain-branched polypropylenes. Rheol Acta 2006;46:33–44.
[39] Vittorias I, Parkinson M, Klimke K, Debbaut B, Wilhelm M. Detection and quantification of industrial polyethylene branching topologies via Fourier-transform rheology. NMR and simulation using the pom-pom model. Rheol Acta 2007;46:321–40.
[40] Vittorias I, Wilhelm M. Application of FT-Rheology towards industrial linear and branched polyethylene blends. Macromol Mater Eng 2007;292:935–48.
[41] Hyun K, Ahn KH, Lee SJ, Sugimoto M, Koyama K. Degree of branching of polypropylene measured from Fourier-transform rheology. Rheol Acta 2006;46:123–9.
[42] Hyun K, Baik ES, Ahn KH, Lee SJ, Sugimoto M, Koyama K. Fourier-transform rheology under medium amplitude oscillatory shear for linear and branched polymer melts. J Rheol 2007;51:1319–42.
[43] Hyun K, Wilhelm M. Establishing a new mechanical nonlinear coefficient Q from FT-Rheology: first investigation on entangled linear and comb polymer model systems. Macromolecules 2009;42:411–22.
[44] Neidhöfer T, Wilhelm M, Debbaut B. Fourier-transform rheology experiments and finite-element simulations on linear polystyrene solutions. J Rheol 2003;47:1351–71.
[45] Neidhöfer T, Sioula S, Hadjichristidis N, Wilhelm M. Distinguishing linear from star-branched polystyrene solutions with Fourier-transform rheology. Macromol Rapid Commun 2004;25:1921–6.
[46] Carotenuto C, Gross M, Maffetone PL. Fourier transform rheology of dilute immiscible polymer blends: a novel procedure to probe blend morphology. Macromolecules 2008;41:4492–500.
[47] Filipe S, Cidade MT, Wilhelm M, Maia JM. Evolution of morphological properties along the extruder length for blends of a commercial liquid crystalline polymer and polypropylene. Polymer 2004;45:2367–80.
[48] Filipe S, Cidade MT, Wilhelm M, Maia JM. Evolution of the morphological properties along the extruder length for compatibilized blends of a commercial liquid crystalline polymer and polypropylene. J Appl Polym Sci 2006;99:347–59.
[49] Daniel C, Hamley IW, Wilhelm M, Mingvanish W. Nonlinear rheology of a face-centered cubic phase in a diblock copolymer gel. Rheol Acta 2001;40:39–48.
[50] Oelschlaeger C, Gutmann JS, Wolkenauer M, Spiess HW, Knoll K, Wilhelm M. Kinetics of shear microphase orientation and reorientation in lamellar diblock and triblock copolymer melts as detected via FT-Rheology and 2D-SAXS. Macromol Chem Phys 2007;208:1719–29.
[51] Kallus S, Willenbacher N, Kirsch S, Distler D, Neidhöfer T, Wilhelm M, Spiess HW. Characterization of polymer dispersions by Fourier transform rheology. Rheol Acta 2001;40:552–9.
[52] Leblanc JL. Fourier transform rheometry on gum elastomers. J Appl Polym Sci 2003;89:1101–15.

[53] Leblanc JL, de la Chapelle C. Updating a torsional dynamic rheometer for Fourier transform rheometry on rubber materials. Rubber Chem Technol 2003;76:287–98.
[54] Leblanc JL, de la Chapelle C. Characterizing gum elastomers by Fourier transform rheometry. Rubber Chem Technol 2003;76:979–1000.
[55] Leblanc JL. Poly(vinyl chloride)-green coconut fiber composite and their nonlinear viscoelastic behavior as examined with Fourier transform rheometry. J Appl Polym Sci 2006;101:3638–51.
[56] Leblanc JL. Fourier transform rheometry on carbon black filled polybutadiene compounds. J Appl Polym Sci 2006;100:5102–18.
[57] Leblanc JL. Investigating the nonlinear viscoelastic behavior of rubber materials through Fourier transform rheometry. J Appl Polym Sci 2005;95:90–106.
[58] Leblanc JL. Investigating the non-linear viscoelastic behavior of filled rubber compounds through Fourier transform rheometry. Rubber Chem Technol 2005;78:54–75.
[59] Leblanc JL. Large amplitude oscillatory shear experiments to investigate the nonlinear viscoelastic properties of highly loaded carbon black rubber compounds without curatives. J Appl Polym Sci 2008;109:1271–93.
[60] Leblanc JL. Non-linear viscoelastic characterization of natural rubber gum through large amplitude harmonic experiments. J Rubber Res 2007;10:63–88.
[61] Leblanc JL. Non-linear viscoelastic characterization of molten thermoplastic vulcanizates (TPV) through large amplitude harmonic experiments. Rheol Acta 2007;46:1013–27.
[62] Debbaut B, Burhin H. Large amplitude oscillatory shear and Fourier-transform rheology for a high-density polyethylene: experiments and numerical simulation. J Rheol 2002;46:1155–76.
[63] Hyun K, Kim SH, Ahn KH, Lee SJ. Large amplitude oscillatory shear as a way to classify the complex fluids. J Non-Newtonian Fluid Mech 2002;107:51–65.
[64] Kim SH, Sim HG, Ahn KH, Lee SJ. Large amplitude oscillatory shear behavior of the network model for associating polymeric systems. Korea-Aust Rheol J 2002;14:49–55.
[65] Sim HG, Ahn KH, Lee SJ. Large amplitude oscillatory shear behavior of complex fluids investigated by a network model: a guideline for classification. J Non-Newtonian Fluid Mech 2003;112:237–50.
[66] Cho KS, Hyun K, Ahn KH, Lee SJ. A geometrical interpretation of large amplitude oscillatory shear response. J Rheol 2005;49:747–58.
[67] Klein OC, Venema P, Sagis L, van der Linden E. Rheological discrimination and characterization of carrageenans and starches by Fourier transform-rheology in the non-linear viscous regime. J Non-Newtonian Fluid Mech 2008;151:145–50.
[68] Ewoldt RH, Hosoi AE, McKinley GH. An ontology for large amplitude oscillatory shear flow. In: Co A, Leal LG, Colby RH, Giacomin AJ, editors. AIP conference proceedings, vol. 1027. Proceedings of the 15th int cong rheol. Monterey, CA: Am Inst Physics; 2008. p. 1135–7.
[69] Ewoldt RH, Hosoi AE, McKinley GH. New measures for characterizing nonlinear viscoelasticity in large amplitude oscillatory shear. J Rheol 2008;52:1427–58.
[70] Skoog DA, Leary JJ. Principles of instrumental analysis. Fort Worth, TX: Saunders College Publishing; 1992.
[71] Williams DJ. Organic polymeric and non–polymeric materials with large optical nonlinearities. Angew Chem Int Ed Engl 1984;23:690–703.
[72] Nam JG, Hyun K, Ahn KH, Lee SJ. Prediction of normal stresses under large amplitude oscillatory shear flow. J Non-Newtonian Fluid Mech 2008;150:1–10.
[73] Reimers MJ, Dealy JM. Sliding plate rheometer studies of concentrated polystyrene solutions: large amplitude oscillatory shear of a very high molecular weight polymer in diethyl phthalate. J Rheol 1996;40:167–86.
[74] Graham MD. Wall slip and the nonlinear dynamics of large amplitude oscillatory shear flows. J Rheol 1995;39:697–712.
[75] Larson RG. Instabilities in viscoelastic flows. Rheol Acta 1992;31:213–63.
[76] Groisman A, Steinberg V. Elastic turbulence in a polymer solution flow. Nature 2000;45:53–5.
[77] Atalık K, Keunings R. On the occurrence of even harmonics in the shear stress response of viscoelastic fluids in large amplitude oscillatory shear. J Non-Newtonian Fluid Mech 2004;122:107–16.
[78] Tapadia P, Ravindranath S, Wang SQ. Banding in entangled polymer fluids under oscillatory shearing. Phys Rev Lett 2006;96, 196001/1–4.
[79] Heymann L, Peukert S, Aksel N. Investigation of the solid–liquid transition of highly concentrated suspensions in oscillatory amplitude sweeps. J Rheol 2002;46:93–112.
[80] Wyss HM, Miyazaki K, Mattsson J, Hu Z, Reichmann DR, Weitz DA. Strain-rate frequency superposition: a rheological probe of structural relaxation in soft materials. Phys Rev Lett 2007;98, 238303/1–4.
[81] Ahn KH, Osaki K. A network model predicting the shear-thickening behavior of a poly(vinyl alcohol)/sodium borate aqueous solution. J Non-Newtonian Fluid Mech 1994;55:215–27.
[82] Harrison G, Franks GV, Tritaatmadja V, Boger DV. Suspensions and polymers – common links in rheology. Korea-Aust Rheol J 1999;11:197–218.
[83] Höfl S, Kremer F, Spiess HW, Wilhelm M, Kahle S. Effect of large amplitude oscillatory shear (LAOS) on the dielectric response of 1,4-cis-polyisoprene. Polymer 2006;47:7282–8.
[84] Inoue T, Osaki K. Rheological properties of poly(vinyl alcohol)/sodium borate aqueous solutions. Rheol Acta 1993;32:550–5.
[85] Storm C, Pastore JJ, MacKintosh FC, Lubensky TC, Janmey PA. Nonlinear elasticity in biological gels. Nature 2005;435:191–4.
[86] Mason TG, Bibette J, Weitz DA. Elasticity of compressed emulsions. Phys Rev Lett 1995;75:2051–4.
[87] Bower C, Gallegos C, Mackley MR, Madiedo JM. The rheological and microstructural characterization of the non-linear flow behavior of concentrated oil-in-water emulsions. Rheol Acta 1999;38:145–59.
[88] Mason TG, Weitz DA. Linear viscoelasticity of colloidal hard sphere suspensions near the glass transition. Phys Rev Lett 1995;75:2770–3.
[89] Bossard F, Moan M, Aubry T. Linear and nonlinear viscoelastic behavior of very concentrated plate-like kaolin suspensions. J Rheol 2007;51:1253–70.
[90] Cloitre M, Borrega R, Leibler L. Rheological aging and rejuvenation in microgel pastes. Phys Rev Lett 2000;85:4819–22.
[91] Sim HG, Ahn KH, Lee SJ. Three-dimensional dynamics simulation of electrorheological fluids under large amplitudes oscillatory shear flow. J Rheol 2003;47:879–95.
[92] Tirtaatmadja V, Tam KC, Jenkins RD. Superposition of oscillations on steady shear flow as a technique for investigating the structure of associative polymers. Macromolecules 1997;30:1426–33.
[93] Tirtaatmadja V, Tam KC, Jenkins RD. Rheological properties of model alkali-soluble associative (HASE) polymers: effect of varying hydrophobe chain length. Macromolecules 1997;30:3271–382.
[94] Tam KC, Guo L, Jenkins RD, Bassett DR. Viscoelastic properties of hydrophobically modified alkali-soluble emulsion in salt solutions. Polymer 1999;40:6369–79.
[95] Hyun K, Nam JG, Wilhelm M, Ahn KH, Lee SJ. Nonlinear response of complex fluids under LAOS (large amplitude oscillatory shear) flow. Korea-Aust Rheol J 2003;15:97–105.
[96] Raghavan SR, Khan SA. Shear induced microstructural changes in flocculated suspensions of fumed silica. J Rheol 1995;39:1311–25.
[97] Parthasarathy M, Klingenberg DJ. Large amplitude oscillatory shear of ER suspensions. J Non-Newtonian Fluid Mech 1999;81:83–104.
[98] Miller RR, Lee E. Rheology of solid propellant dispersions. J Rheol 1991;35:901–20.
[99] Ma L, Xu J, Coulombe PA, Wirtz D. Keratin filament suspensions show unique micromechanical properties. J Biol Chem 1999;274:19145–51.
[100] Citerne GP, Carreau PJ, Moan M. Rheological properties of peanut butter. Rheol Acta 2001;40:86–96.
[101] Carreau PJ, Lavoie PA, Yziquel F. Rheological properties of concentrated suspensions. In: Siginer DA, Kee DD, Chhabra RP, editors. Advances in the flow and rheology of non-Newtonian fluids, Rheology Series, vol. 8. Amsterdam: Elsevier; 1999. p. 1299–345.
[102] Rochefort WE, Middleman S. Rheology of Xanthan gum: salt, temperature, and strain effects in oscillatory and steady shear experiments. J Rheol 1987;31:337–69.
[103] Neidhöfer T, Wilhelm M, Debbaut B, Hadjichristidis N. FT-rheology and finite-element simulations on polystyrene solutions and melts of various topologies. In: Muenstedt H, Kaschta J, Merten A, editors. 6th European conference on rheology. Erlangen Germany: European Soc Rheol; 2002. p. 463–4.
[104] Chopra D, Vlassopoulos D, Hatzikiriakos SG. Nonlinear rheological response of phase separating polymer blends: poly(styrene-co-maleic anhydride)/poly(methyl methacrylate). J Rheol 2000;44:27–45.
[105] Lim T, Uhl JT, Prud'homme RK. Rheology of self-associating concentrated Xanthan solutions. J Rheol 1984;28:367–79.
[106] Hamley IW, Pole JA, Booth C, Derici L, Imperor-Clerc M, Davidson P. Shear-induced orientation of the body-centered-cubic phase in diblock copolymer gel. Phys Rev E 1998;58:7620–8.
[107] Okamoto S, Saijo K, Hashimoto T. Dynamics SAXS studies of sphere-forming block copolymers under large oscillatory shear deformation. Macromolecules 1994;27:3753–8.

[108] Gadala-Maria F, Acrivos A. Shear-induced structure in a concentrated suspension of solid spheres. J Rheol 1980;24:799–814.
[109] Powell JA. Application of a nonlinear phenomenological model to the oscillatory behavior of ER materials. J Rheol 1995;39:1075–94.
[110] Li H, Du H, Chen G, Yeo SH, Guo N. Nonlinear viscoelastic properties of MR fluids under large-amplitude-oscillatory shear. Rheol Acta 2003;42:280–6.
[111] Ewoldt RH, Clasen C, Hosoi AE, McKinley GH. Rheological fingerprinting of gastropod pedal mucus and synthetic complex fluids for biomimicking adhesive locomotion. Soft Matter 2007;3:634–43.
[112] Tariq S, Giacomin AJ, Gunasekaran S. Nonlinear viscoelasticity of cheese. Biorheology 1998;35:171–91.
[113] Lodge AS, Elastic Liquids:. An introductory vector treatment of finite-strain polymer rheology. New York: Academic Press; 1964.
[114] Coleman BD, Dill EH, Toupin RA. A phenomenological theory of streaming birefringence. Arch Rational Mech Anal 1970;39:358–99.
[115] Coleman BD, Markovitz H. Asymptotic relations between shear stresses and normal stresses in general incompressible fluids. J Polym Sci Polym Phys Ed 1974;12:2195–207.
[116] Vrentas JS, Venerus DC, Vrentas CM. Finite amplitude oscillations of viscoelastic fluids. J Non-Newtonian Fluid Mech 1991;40: 1–24.
[117] Oakley JG, Giacomin AJ. A sliding plate normal thrust rheometer for molten plastics. Polym Eng Sci 1994;34:580–4.
[118] Janmey PA, McCormick ME, Rammensee S, Leight JL, Georges PC, MacKintosh FC. Negative normal stress in semiflexible biopolymer gels. Nature Mater 2007;6:48–51.
[119] Labiausse V, Höhler R, Cohen-Addad S. Shear induced normal stress difference in aqueous foams. J Rheol 2007;51:479–92.
[120] Jeyaseelan RS, Giacomin AJ. Network theory for polymer solutions in large amplitude oscillatory shear. J Non-Newtonian Fluid Mech 2008;148:24–32.
[121] Férec J, Heuzey MC, Ausias G, Carreau PJ. Rheological behavior of fiber-filled polymers under large amplitude oscillatory shear flow. J Non-Newtonian Fluid Mech 2008;151:89–100.
[122] James DF. Boger fluids. Annu Rev Fluid Mech 2009;41:129–42.
[123] Larson RG. Constitutive equations for polymer melts and solutions. Boston: Butterworths; 1988.
[124] Nam JG, Ahn KH, Lee SJ. Analysis of the normal stress differences of viscoelastic fluids under large amplitude oscillatory shear flow. In: Co A, Leal LG, Colby RH, Giacomin AJ, editors. AIP conference proceedings, vol. 1027. Proceedings of the 15th int cong rheol. Monterey, CA: Am Inst Physics; 2008. p. 171–3.
[125] Nam JG, Ahn KH, Lee SJ, Hyun K. First normal stress difference of entangled polymer solutions in large amplitude oscillatory shear flow. J Rheol 2010;54:1243–66.
[126] Hilliou L, Dusschoten DV, Wilhelm M, Burhin H, Rodger ER. Increasing the torque sensitivity of an RPA 2000 by a factor 5-10 using advanced data acquisition. Rubber Chem Technol 2004;77:192–200.
[127] Liu J, Yu W, Zhou W, Zhou C. Control on the topological structure of polyolefin elastomer by reactive processing. Polymer 2009;50:547–52.
[128] Kossuth MB, Morse DC, Bates FS. Viscoelastic behavior of cubic phases in block copolymer melts. J Rheol 1999;43:167–96.
[129] Kim DH, Park JU, Ahn KH, Lee SJ. Electrically activated poly(propylene)/clay nanocomposites. Macromol Rapid Commun 2003;24:388–91.
[130] Yu W, Wang P, Zhou C. General stress decomposition in nonlinear oscillatory shear flow. J Rheol 2009;53:215–38.
[131] Larson RG. The structure and rheology of complex fluids. Oxford: Oxford University Press; 1999.
[132] Macosko CW. Rheology, principles, measurements and applications. NY: VCH; 1994.
[133] Hatzikiriakos SG, Dealy JM. Role of slip and fracture in the oscillating flow of HDPE in a capillary. J Rheol 1992;36:845–84.
[134] Yoshimura AS, Prud'homme RK. Wall slip effects on dynamic oscillatory measurements. J Rheol 1988;32:575–84.
[135] Yosick JA, Giacomin AJ, Stewart WE, Ding F. Fluid inertia in large amplitude oscillatory shear. Rheol Acta 1998;37:365–73.
[136] Mas R, Magnin A. Experimental validation of steady shear and dynamic viscosity relation for yield stress fluids. Rheol Acta 1997;36:49–55.
[137] Sagis LMC, Ramaekers M, van der Linden E. Constitutive equations for an elastic material with anisotropic rigid particles. Phys Rev E 2001;63, 051504/1–8.
[138] Ewoldt RH, Hosoi AE, McKinley GH. Rheological fingerprinting of complex fluids using large amplitude oscillatory shear (LAOS) flows. Ann Trans Nordic Soc Rheol 2007;15:3–8.
[139] Kim H, Hyun K, Kim DJ, Cho KS. Comparison of interpretation methods for large amplitude oscillatory shear response. Korea-Aust Rheol J 2006;18:91–8.
[140] Calin A, Balan C, Wilhelm M. A new approach to determine the nonlinear parameter of the Giesekus constitutive model. In: Co A, Leal LG, Colby RH, Giacomin AJ, editors. AIP conference proceedings, vol. 1027. Proceedings of the 15th int cong rheol. Monterey, CA: Am Inst Physics; 2008. p. 1372–4.
[141] Ewoldt RH, McKinley GH. On secondary loops in LAOS via self-intersection of Lissajous-Bowditch curves. Rheol Acta 2010;49:213–9.
[142] Rogers SA, Vlassopoulos D. Frieze group analysis of asymmetric response to large-amplitude oscillatory shear. J Rheol 2010;54:859–80.
[143] Renou F, Stellbrink J, Petekidis G. Yielding processes in a colloidal glass of soft star-like micelles under large amplitude oscillatory shear (LAOS). J Rheol 2010;54:1219–42.
[144] Ganeriwala SN, Rotz CA. Fourier-transform mechanical analysis for determining the nonlinear viscoelastic properties of polymers. Polym Eng Sci 1987;27:165–78.
[145] Franck AJP, Nowak M. Non-linear oscillation testing with a separate motor transducer rheometer. In: Co A, Leal LG, Colby RH, Giacomin AJ, editors. AIP conference proceedings, vol. 1027. Proceedings of the 15th int cong rheol. Monterey, CA: Am Inst Physics; 2008. p. 1138–40.
[146] Grosso M, Maffettone PL. A new methodology for the estimation of drop size distributions of dilute polymer blends based on LAOS flows. J Non-Newtonian Fluid Mech 2007;143:48–58.
[147] Yu W, Bousmina M, Zhou C. Note on morphology determination in emulsions via rheology. J Non-Newtonian Fluid Mech 2006;133:57–62.
[148] Leblanc JL, Nijman G. Engineering performance and material viscoelastic analyses along a compounding line for silica-based compounds. Part 2. Nonlinear viscoelastic analysis. J Appl Polym Sci 2009;112:1128–41.
[149] Langela M, Wilhelm M, Wiesner U, Spiess HW. Microphase reorientation in block copolymer melts as detected via FT-Rheology and 2D-SAXS. Macromolecules 2002;35:3198–204.
[150] Mortensen K, Pedersen JS. Structural study on the micelle formation of poly(ethylene oxide)–poly(propylene oxide)–poly(ethylene oxide) triblock copolymer in aqueous solution. Macromolecules 1993;26:805–12.
[151] Denny MW. The role of gastropod pedal mucus in locomotion. Nature 1980;285:160–1.
[152] Ewoldt RH, Hosoi AE, McKinley GH. Nonlinear viscoelastic biomaterials: meaningful characterization and engineering inspiration. Integr Comp Biol 2009;49:40–50.
[153] Davis WM, Macosko CW. Nonlinear dynamic mechanical moduli for polycarbonate and PMMA. J Rheol 1978;22:53–71.
[154] Papon A, Montes H, Lequeux F, Guy L. Nonlinear rheology of model filled elastomers. J Polym Sci Part B: Polym Phys 2010;48:2490–6.
[155] Ewoldt RH, Winegard TM, Fudge DS. Non-linear viscoelasticity of hagfish slime. Int J Non-linear Mech 2010, doi:10.1016/j.ijnonlinmec.2010.10.003.
[156] Ng TSK, McKinley GH, Ewoldt RH. Large amplitude oscillatory shear flow of gluten dough; a model power-law gel. J Rheol 2011;55:627–54.
[157] Doi M, Edward SF. The theory of polymer dynamics. Oxford: Clarendon Press; 1986.
[158] Bent J, Hutchings LR, Richards RW, Gough T, Spares R, Coates PD, Grillo I, Harlen OG, Read DJ, Graham RS, Likhtman AE, Groves DJ, Nicholson TM, McLeish TCB. Neutron-mapping polymer flow: scattering, flow visualization, and molecular theory. Science 2003;301:1691–5.
[159] Janeschitz-Krigel H. Polymer melt rheology and flow birefringence. Berlin: Springer; 1983.
[160] Fuller GG. Optical rheometry. Oxford: Oxford University Press; 1995.
[161] Safinya CR, Sirota EB, Plano RJ. Nematic to Smectic-A phase transition under shear flow: a nonequilibrium synchrotron X-ray study. Phys Rev Lett 1991;66:1986–9.
[162] Dootz R, Evans H, Köster S, Pfohl T. Rapid prototyping of X-ray microdiffraction compatible continuous microflow foils. Small 2007;3:96–100.
[163] Chen ZR, Kornfield JA, Smith SD, Grothaus JT, Satkowski MM. Pathways to macroscale order in nanostructured block copolymers. Science 1997;277:1248–53.
[164] Wiesner U. Lamellar diblock copolymers under large amplitude oscillatory shear flow: order and dynamics. Macromol Chem Phys 1997;198:3319–52.

[165] Hamley IW. Structure and flow behaviour of block copolymers. J Phys Condens Matter 2001;13:R643–71.
[166] Hamley IW, Castelletto V. Small-angle scattering of block copolymers in the melt, solution and crystal states. Prog Polym Sci 2004;29:909–48.
[167] Watanabe H, Matsumiya Y, Inoue T. Rheo-dielectrics in oligomeric and polymeric fluids: a review of recent findings. J Phys Condens Matter 2003;15:S909–21.
[168] Capaccioli S, Prevosto D, Best A, Hanewald A, Pakula T. Applications of the rheo-dielectric technique. J Non-Cryst Solids 2007;353:4267–72.
[169] Watanabe H, Sato T, Hirose M, Osaki K, Yao ML. Rheo-dielectric behavior of low molecular weight liquid crystals. 1. Behavior of nematic 5CB and 7CB. Rheol Acta 1998;37:519–27.
[170] Watanabe H, Sato T, Hirose M, Osaki K, Yao ML. Rheo-dielectric behavior of low molecular weight liquid crystals. 2. Behavior of 8CB in nematic and smectic states. Rheol Acta 1999;38: 100–7.
[171] Watanabe H. Dielectric relaxation of type-A polymers in melts and solutions. Macromol Rapid Commun 2001;22:127–75.
[172] Watanabe H, Matsumiya Y, Inoue T. Dielectric and viscoelastic study of entanglement dynamics: a review of recent findings. Macromol Symp 2005;228:51–70.
[173] Alig I, Skipa T, Lellinger D, Potschke P. Destruction and formation of a carbon nanotube network in polymer melts: rheology and conductivity spectroscopy. Polymer 2008;49:3524–32.
[174] Watanabe H, Matsumiya Y, Kakiuchi M, Aoki Y. Rheo-dielectric behavior of carbon black suspensions. Nihon Reoroji Gakkaishi 2001;29:77–80.
[175] Hyun K, Höfl S, Kahle S, Wilhelm M. The rheo-dielectric setup to measure dielectric spectra of 1,4-cis-polyisoprene under large amplitude oscillatory shear (LAOS). J Non-Newtonian Fluid Mech 2009;160:93–103.
[176] Watanabe H, Ishida S, Matsumiya Y. Rheodielectric behavior of entangled cis-polyisoprene under fast shear. Macromolecules 2002;35:8802–18.
[177] Stockmayer WH, Burke JJ. Dielectric dispersion in branched polypropylene oxide. Macromolecules 1969;2:647–50.
[178] Adachi K, Kotaka T. Dielectric normal mode relaxation. Prog Polym Sci 1993;18:585–622.
[179] Pople JA, Hamley IW, Fairclough JPA, Ryan AJ, Booth C. Orientational ordering of a poly(oxyethylene)–poly(oxybutylene) diblock copolymer gel under steady shear flow. Macromolecules 1998;31:2952–6.
[180] Panine P, Gradzielski M, Narayanan T. Combined rheometry and small-angle X-ray scattering. Rev Sci Instrum 2003;74: 2451–5.
[181] Rathgeber S, Lee H, Matyjaszewski K, Cola ED. Rheooscillations of a bottlebrush polymer solution due to shear-induced phase transitions between a shear molten state and a line hexatic phase. Macromolecules 2007;40:7680–8.
[182] Polushkin E, Ekenstein GA, Dolbnya I, Bras W, Ikkala O, Brinke G. In situ radial small angle synchrotron X-ray scattering study of shear-induced macroscopic orientation of hierarchically structured comb-shaped supramolecules. Macromolecules 2003;36:1421–3.
[183] Polushkin E, Ekenstein GA, Ikkala O, Brinke G. A modified rheometer for in-situ radial and tangential SAXS studies on shear-induced alignment. Rheol Acta 2004;43:364–72.
[184] Caputo FE, Burghardt WR, Krishnan K, Bates FS, Lodge TP. Time-resolved small-angle X-ray scattering measurements of a polymer bicontinuous microemulsion structure factor under shear. Phys Rev E 2002;66, 041401/1–18.
[185] Dingenouts N, Wilhelm M. New developments for the mechanical characterization of materials. Korea-Aust Rheol J 2010;22:317–30.
[186] Struth B, Hyun K, Kats E, Meins T, Walther M, Wilhelm M, Grübel G. Observation of New States of Liquid Crystal 8CB under Nonlinear Shear Conditions as Observed via a Novel and Unique Rheology/Small-Angle X-ray Scattering Combination. Langmuir 2011;27:2880–7.
[187] Garcia-Gutierrez MC, Hernandez JJ, Nogales A, Panine P, Rueda DR, Ezquerra TA. Influence of shear on the templated crystallization of poly(butylene terephthalate)/single wall carbon nanotube nanocomposites. Macromolecules 2008;41:844–51.
[188] Calin A, Wilhelm M, Balan C. Determination of the nonlinear parameter (mobility factor) of the Giesekus constitutive model using LAOS procedure. J Non-Newtonian Fluid Mech 2010;165:1564–77.
[189] Brader JM, Siebenbürger M, Ballauff M, Reinheimer K, Wilhelm M, Frey SJ, Weysser F, Fuchs M. Nonlinear response of dense colloidal suspensions under oscillatory shear: mode-coupling theory and Fourier transform rheology experiments. Phys Rev E 2010;82, 061401/1–20.
[190] Läuger J, Stettin H. Differences between stress and strain control in the non-linear behavior of complex fluids. Rheol Acta 2010;49:909–30.
[191] Bejenariu AG, Rasmussen HK, Skov AL, Hassager O, Frankaer SM. Large amplitude oscillatory extension of soft polymeric networks. Rheol Acta 2010:807–14.
[192] Li X, Wang SQ. Nonlinear rheological behavior of diphenylmethylvinyl silicone gum: an example of homogeneous shear. Rheol Acta 2010;49:89–94.
[193] Zhou L, Cook LP, McKinley GH. Probing shear-banding transitions of the VCM model for entangled wormlike micellar solutions using large amplitude oscillatory shear (LAOS) deformations. J Non-Newtonian Fluid Mech 2010;165:1462–72.